

**APPLICATION OF ION-MOLECULE REACTIONS TO STRUCTURE
CHARACTERIZATION AND THERMOCHEMICAL PROPERTY MEASUREMENTS**

by

Mingxiang Lin

BS, Nanjing University, P. R. China, 1997

Submitted to the Graduate Faculty of
Arts and Sciences in partial fulfillment
of the requirements for the degree of
Doctor of Philosophy

University of Pittsburgh

[2004]

UNIVERSITY OF PITTSBURGH
FACULTY OF ARTS AND SCIENCES

This dissertation was presented

by

Mingxiang Lin

It was defended on

November 22nd, 2004

and approved by

Adrian C. Michael

Sunil K. Saxena

Billy W. Day

Joseph J. Grabowski
Dissertation Director

APPLICATION OF ION-MOLECULE REACTIONS TO STRUCTURE CHARACTERIZATION AND THERMOCHEMICAL PROPERTY MEASUREMENTS

Mingxiang Lin, PhD

University of Pittsburgh, 2004

This thesis explores several novel applications of gas-phase ion-molecule reactions to solve analytical problems. In all cases, the application of an ion-molecule reaction to solve a specific challenge is based on a thorough understanding of the fundamental aspects of the reaction, including kinetics, production distributions and most notably, its reaction mechanism.

Ion-molecule reactions of the atomic oxygen radical anion, $O^{\bullet-}$, with selected ketones are investigated to explore a strategy to synthesize 1,3-distonic radical anions, which are precursors to 1,3-diyls. The $O^{\bullet-}$ /cyclopentanone reaction is examined in detail, under the well-defined thermal conditions uniquely available in the flowing afterglow, to ascertain if cyclopentan-2-one-1,3-diyl radical anion is formed. To further the understanding of this key reaction, a series of related ketones are also examined. Rate coefficients for each ketone reaction are measured, products are identified, and the branching ratios are determined. A strategy is developed to differentiate the 1,1- and 1,3- H_2^{**} isobaric abstraction products. A total yield of 48% $[M-2H]^{\bullet-}$ is obtained for the $O^{\bullet-}$ /cyclopentanone reaction, wherein ~15% is the absolute yield of the 1,1- and ~33% is the absolute yield of the 1,3- H_2^{**} abstraction product.

A chemical reagent that specifically cleaves the peptide backbone will greatly simplify peptide sequencing as compared to nonselective energetic collisions with inert gases. In the search for peptide cleavage reagents, translationally-driven, endothermic ion-molecule reactions between peptide ions and potential cleavage reagents are investigated in a custom-built,

electrospray ionization, triple quadrupole mass spectrometer. Strategies are adopted to minimize nonselective energetic fragmentation processes and to favor amide bond cleavage.

The kinetic method is used to derive the relative and absolute proton affinities of two neuropeptides, leucine-enkephalin and methionine-enkephalin. Based on analyses of the collision induced fragmentation of the proton-bound heterodimer of leucine-enkephalin and methionine-enkephalin, leucine-enkephalin is established to be 0.1 kcal/mol lower in proton affinity than methionine-enkephalin. Based on analyses of the collision induced fragmentation of the proton-bound heterodimer of leucine-enkephalin or methionine-enkephalin and triethylamine, tripropylamine or tributylamine, the absolute proton affinities of leucine-enkephalin and methionine-enkephalin are established to be 238.5 and 238.6 (± 5.0) kcal/mol.

TABLE OF CONTENTS

PREFACE.....	xiii
Chapter 1 Introduction.....	1
1.1. Overview.....	1
1.2. The flowing afterglow.....	5
1.3. Gas phase ion-molecule reaction coordinate diagrams.....	7
1.4. Ion-molecule reaction efficiencies.....	8
1.5. References.....	9
Chapter 2 Didehydro Radical Anions from Ketones via O ⁻ Chemical Ionization.....	12
2.1. Introduction.....	12
2.2. Experimental.....	14
2.3. Results.....	18
2.3.1. Acetone.....	24
2.3.2. 3-Pentanone.....	25
2.3.3. Cyclopentanone.....	30
2.3.4. 2-Butanone.....	33
2.3.5. Cyclohexanone.....	33
2.3.6. 2,4-Dimethyl-3-pentanone.....	36
2.3.7. 3,3-Dimethyl-2-butanone.....	41
2.4. Discussion.....	44
2.4.1. Reaction rates and proton transfer.....	44
2.4.2. HAT.....	45
2.4.3. Addition-elimination.....	45
2.4.4. 1,1-H ₂ ⁺ abstraction.....	46
2.4.5. 1,3-H ₂ ⁺ abstraction.....	50
2.4.6. Miscellaneous considerations.....	53
2.5. Conclusions.....	56
2.6. References.....	56
Chapter 3 Targeting Cleavage of the Peptide Amide Bond via Selective Gas-Phase Ion-Molecule Reactions.....	59
3.1. Introduction.....	59
3.2. Experimental.....	68
3.3. Results.....	71
3.3.1. Endothermic proton transfer.....	71
3.3.2. Leucine-enkephalin MS/MS experiments with hydrazine.....	73
3.3.3. GGFL-NH ₂ MS/MS experiments with hydrazine and ethylenediamine.....	76
3.3.4. GGFL-NH ₂ MS/MS experiments with formic acid and acetic anhydride.....	81
3.3.5. Ar CID on noncovalent complexes generated from solutions.....	81
3.3.6. MS/MS experiment on Ac ₂ O with hydrazine.....	84
3.4. Discussion.....	87
3.4.1. Cleavage mechanism.....	87
3.4.2. Potential complications.....	88
3.4.3. Alternative solutions.....	91
3.4.4. Negative ion cleavage.....	94

3.5. Conclusion	95
3.6. References.....	96
Chapter 4 Leucine-Enkephalin and Methionine-Enkephalin Proton Affinity Measurement via the Extended Kinetic Method	99
4.1. Introduction.....	99
4.2. Experimental	103
4.3. Results.....	105
4.3.1. Relative proton affinity measurement.....	105
4.3.2 Absolute proton affinity measurement using ESI-TQMS	108
4.4. Discussion.....	116
4.4.1 The absolute proton affinity.....	116
4.4.2 Entropy consideration.	117
4.4.3. Effective temperature.....	118
4.5. Conclusion	120
4.6. References.....	120
Appendix A Gas-Phase Thermochemical Properties.....	123

LIST OF TABLES

Table 2.1. Reaction rate coefficients for $O^{\bullet-}$ with selected ketones in the gas phase at room temperature	19
Table 2.2. Summary of the primary product distributions for the reaction of $O^{\bullet-}$ with selected ketones ^a	20
Table 2.3. Enthalpies used in this work.	21
Table 2.4. Yields of radical anion from the reaction of $O^{\bullet-}$ with ketones.....	52
Table 3.1. Results of the gas-phase ion-molecule reactions between $CH_3CON(^-)CH_3$ and selected X-Y reagents. Data has been presented on the 39 th ASMS Conference at Mass Spectrometry and Allied Topics [33].	64
Table 3.2. Summary of ion-molecule reactions between positive analogs with selected neutral examined in the flow afterglow. PT stands for proton transfer; NR stands for no reaction.	67
Table 3.3. Summary of product ions observed from MS/MS experiments examined in this study.	86
Table 4.1. Slopes and y-intercepts obtained from Figure 4.6(a). Effective temperatures are derived from the slopes ($-1/RT_{eff}$) and the apparent proton affinities are obtained from dividing y-intercepts by the corresponding slopes. Experiments are performed on the TQMS.	113
Table 4.2. Slopes and y-intercepts obtained from Figure 4.7(a). Effective temperatures are derived from the slopes ($-1/RT_{eff}$) and the apparent proton affinities are obtained from dividing y-intercepts by the corresponding slopes. Experiments are performed on the TQMS.	114
Table 4.3. Summary of the slopes and y-intercepts from the plots of $[PA(app)-PA(avg)]/RT_{eff}$ vs. $1/RT_{eff}$ derived from data obtained from TQMS experiments. The absolute proton affinity is the sum of the slope and $PA(avg)$ which is 236.7 kcal/mol for these experiments. The $\Delta(\Delta S)$ is obtained from the product of molar gas constant R and the y-intercept.	115
Table 4.4. Summary of experimental determination of the proton affinity of LeuEnk and MetEnk using TEA, TPA and TBA as references obtained from TQMS and Q-TOF at different experimental conditions. Proton affinities shown are the average of replicate experiments, the number of which is shown in parentheses.	115

LIST OF FIGURES

Figure 1.1. A schematic diagram of the flowing afterglow apparatus at the University of Pittsburgh.....	6
Figure 1.2. Reaction coordinate diagram for a nucleophilic substitution reaction in the gas-phase.	7
Figure 2.1. Representative semi-logarithm plots of ion intensity vs. reaction distance for the reactions of $O^{\bullet-}$ and several ketones. For these individual experiments, the number of half lives for which the reaction was followed in order to obtain the rate coefficient were: acetone, 2.8; cyclopentanone, 3.7; and 3-pentanone 2.6.	23
Figure 2.2. Representative branching ratio plot for the reaction of $O^{\bullet-}$ with acetone. The symbols represent experimentally observed data; the solid lines are a smooth fit to the observed data points.....	26
Figure 2.3. Representative branching plot for the reaction of $O^{\bullet-}$ with 3-pentanone. The symbols represent experimentally observed data; the solid lines are a smooth fit to the observed data points.....	28
Figure 2.4. Representative branching plot for the reaction of $O^{\bullet-}$ with cyclopentanone. The symbols represent experimentally observed data; the solid lines are a smooth fit to the observed data points.....	31
Figure 2.5. Representative branching plot for the reaction of $O^{\bullet-}$ with 2-butanone. The symbols represent experimentally observed data; the solid lines are a smooth fit to the observed data points. $C_4H_5O_2^-$ (m/z 85) is not shown in the figure to avoid congestions. The insert is an enlargement of the Y-scale and includes only the 4 minor products.....	34
Figure 2.6. Representative branching plot for the reaction of $O^{\bullet-}$ with cyclohexanone. The symbols represent experimentally observed data; the solid lines are a smooth fit to the observed data points.....	37
Figure 2.7. Representative branching plot for the reaction of $O^{\bullet-}$ with 2,4-dimethyl-3-pentanone. The symbols represent experimentally observed data; the solid lines are a smooth fit to the observed data points.....	39
Figure 2.8 Structures of (a) ring-opened form of 1,1- H_2^+ abstraction product from cyclopentanone and (b) oxidation product of ring-opened form of 1,1- D_2^+ abstraction from 2,2,5,5- d_4 -cyclopentanone.....	49
Figure 2.9. Structures of TMM, 1,3- distonic radical anion of acetone, 1,3-radical anion of cyclopentanone, and 1,1-radical anion of cyclopentanone	55
Figure 3.1. Definitions of peptide complementary a_n , b_n c_n and x_n , y_n z_n sequence ions.....	59
Figure 3.2. Electron capture dissociation scheme for the production of c_n and z_n type ions from a multiply protonated peptide.....	60
Figure 3.3. Ion-molecule reactions of methoxymethyl cation with peptide analogs. Figure adapted from [26].....	62
Figure 3.4. Proposed scheme for peptide bond cleavage via transacylation reaction. Figure adapted from [32].....	62
Figure 3.5. Strategy of a X-Y designer reagent cleaving the amide bond in a peptide analog.....	63
Figure 3.6. Proposed mechanism for CF_3COSEt cleaving deprotonated N-methylacetate ion....	65
Figure 3.7. Schematic diagram of the custom-built ESI-triple quadrupole mass spectrometer equipped with an electrospray source.....	70

Figure 3.8. Diagram of the ESI interface in the ESI-TQMS.	70
Figure 3.9. Endothermic proton transfer from a protonated glycine to methanol. (a) SIM spectrum of protonated glycine, generated from ESI of a glycine solution. (b) Product ion spectrum when methanol is used as collision gas at $\langle KE_{cm} \rangle = 1.5$ eV; protonated MeOH is observed. (c) Product ion spectrum when Ar is used as collision gas at $\langle KE_{cm} \rangle = 1.5$ eV. (Illustrations: filled cycle (●) – precursor ion; open cycle (○)– product ions; target gas – indicated on the right side of the arrow.)	72
Figure 3.10. Structure of Leucine-enkephaline (YGGFL, MW=555).	73
Figure 3.11. LeuEnk CID experiment using hydrazine as collision gas. (a) Electrospray spectrum of a 50 μ M LeuEnk solution with 5mM LiCl in 50:50 MeOH/H ₂ O. (b) SIM spectrum of protonated LeuEnk. (c) Product ion spectrum of protonated LeuEnk at $\langle KE_{cm} \rangle = 0.3$ eV. (d) Product ion spectrum of protonated LeuEnk at $\langle KE_{cm} \rangle = 0.8$ eV.	74
Figure 3.12. (a) Product ion spectrum of lithiated LeuEnk using Ar as collision gas at $\langle KE_{cm} \rangle = 1.3$ eV. (b) Product ion spectrum of lithiated LeuEnk using hydrazine as collision gas at $\langle KE_{cm} \rangle = 0.8$ eV. (c) Product ion spectrum of sodiated LeuEnk using Ar as collision gas at $\langle KE_{cm} \rangle = 1.3$ eV. (d) Product ion spectrum of sodiated LeuEnk using hydrazine as collision gas at $\langle KE_{cm} \rangle = 0.8$ eV.	75
Figure 3.13. Hypothetical mechanism for hydrazine cleaving an amide bond in a cationized peptide ion in the gas-phase.	76
Figure 3.14. Structure of [des-Tyr1]-Leucine enkephalinamide (GGFL-NH ₂ , MW=391)	76
Figure 3.15. (a) Electrospray spectrum of a 50 μ M GGFL-NH ₂ solution in 49.5:49.5:1 MeOH/H ₂ O/Acetic acid solution (M stands for the neutral molecule, GGFL-NH ₂). (b) SIM spectrum of protonated GGFL-NH ₂ , a small amount of (M+H-NH ₃) ⁺ is observed possible due to the CID resulting from the residue gas in the collision chamber. (c) Product ion spectrum of Ar CID on protonated GGFL-NH ₂	78
Figure 3.16. (a) Electrospray spectrum of a 50 μ M GGFL-NH ₂ solution with 5mM NaCl added. (M stands for the neutral molecule of GGFL-NH ₂). (b) SIM spectrum of sodiated GGFL-NH ₂ . (c) Product ion spectrum of Ar CID on sodiated GGFL-NH ₂	79
Figure 3.17. (a) Product ion spectrum of protonated GGFL-NH ₂ with hydrazine as collision gas at $\langle KE_{cm} \rangle = 0.4$ eV. (b) Product ion spectrum of protonated GGFL-NH ₂ with hydrazine as collision gas at $\langle KE_{cm} \rangle = 1.2$ eV (c) Product ion spectrum of protonated GGFL-NH ₂ with ethylenediamine as collision gas at $\langle KE_{cm} \rangle = 0.7$ eV. (b) Product ion spectrum of sodiated GGFL-NH ₂ with ethylenediamine as collision gas at $\langle KE_{cm} \rangle = 1.8$ eV.	80
Figure 3.18. (a) Product ion spectrum of sodiated GGFL-NH ₂ with formic acid as collision gas at $\langle KE_{cm} \rangle = 0.5$ eV. (b) Product ion spectrum of sodiated GGFL-NH ₂ with formic acid collision gas at $\langle KE_{cm} \rangle = 1.1$ eV. (c) Product ion spectrum of sodiated GGFL-NH ₂ with acetic anhydride as collision gas at $\langle KE_{cm} \rangle = 0$ eV. (d) Product ion spectrum of sodiated GGFL-NH ₂ with acetic anhydride as collision gas at $\langle KE_{cm} \rangle = 1.0$ eV.	82
Figure 3.19. (a) Electrospray spectrum of a mixture methanol solution of GGFL-NH ₂ with 25% hydrazine. Unlabeled ions are unidentified. (b) Product ion spectrum of Ar CID on the proton-bound heterodimer of GGFL-NH ₂ and hydrazine at $\langle KE_{cm} \rangle = 0.4$ eV. (c) Product ion spectrum of Ar CID on the proton-bound heterodimer of GGFL-NH ₂ and hydrazine at $\langle KE_{cm} \rangle = 1.3$ eV.	83
Figure 3.20. (a) Electrospray spectrum of pure Ac ₂ O liquid. (b) Product ion spectrum of MS/MS experiment on sodiated Ac ₂ O with NH ₂ NH ₂ as collision gas at $\langle KE_{cm} \rangle = 2.1$ eV. (c)	

Product ion spectrum of sodiated Ac ₂ O with NH ₂ NH ₂ as collision gas at $\langle KE_{cm} \rangle = 3.1$ eV.	85
Figure 3.21. Reaction scheme for the fragmentation of a sodiated peptide during the CID process.	88
Figure 3.22. Hypothetical mechanism for HCOOH cleaving an amide bond in a sodiated peptide ion.	90
Figure 3.23. Proposed mechanism of production of b ₁ and y _n fragments from [M+2H] ²⁺ ions of peptide PTC derivatives.	92
Figure 3.24. (a) Acetamidination reaction of a peptide. (b) Proposed cyclic intermediate leading to y _{n-1} in formation.	92
Figure 3.25. Proposed scheme for derivation of protonated peptide via gas-phase ion-molecule reaction of a protonated peptide and acetone.	93
Figure 3.26. Proposed scheme for cleavage of a negatively charged peptide ion by using HOOH as the cleavage reagent.	95
Figure 4.1. ESI of a mixture solution containing 500 μM LeuEnk and MetEnk each obtained from the TQMS; the spray conditions are 0.1 μl/min flow rate and 2.5 kV spray voltage.	106
Figure 4.2. A representative product ion spectrum of CID on the proton-bound dimer of LeuEnk and MetEnk obtained from the TQMS; $\langle KE_{CM} \rangle = 0.50$ eV.	106
Figure 4.3. The intensities of protonated MetEnk and protonated LeuEnk resulting from CID on the proton-bound heterodimer ion as a function of collision energy; the experiment was performed on the Q-TOF.	107
Figure 4.4. The intensity ratio of protonated MetEnk to protonated LeuEnk resulting from CID on the proton-bound heterodimer ion as a function of collision energy; the experiment was performed on the Q-TOF.	107
Figure 4.5. TQMS experiments of enkephalin proton affinity measurement versus pentaglycine: (a) Electrospray spectrum of a LeuEnk/pentaglycine mixture solution. (b) Electrospray spectrum of a MetEnk/pentaglycine mixture solution. (c) CID on the proton-bound heterodimer of LeuEnk and pentaglycine using Ar as collision gas. (d) CID on the proton-bound heterodimer of MetEnk and pentaglycine using Ar as collision gas.	111
Figure 4.6. A set of representative CID product ion spectra: (a) CID on the proton-bound heterodimer of TEA and LeuEnk. Product ions observed are protonated LeuEnk and protonated TEA. (b) CID on the proton-bound heterodimer of TPA and LeuEnk. Product ions observed are protonated LeuEnk and protonated TPA. (c) CID on the proton-bound heterodimer of TBA and LeuEnk. Product ions observed are protonated LeuEnk and protonated TBA.	112
Figure 4.7. (a) The natural logarithm of the intensity ratio of protonated LeuEnk to protonated trialkylamine $\ln(\text{LeuEnk}/\text{Amine})$ as a function of PA(amine)-PA(avg) obtained at various collision energies. (b) The plot of [PA(apparent)-PA(avg)]/RT _{eff} versus 1/RT _{eff} .	113
Figure 4.8. (a) The natural logarithm of the intensity ratio of protonated MetEnk to protonated trialkylamine $\ln(\text{MetEnk}/\text{Amine})$ as a function of PA(amine)-PA(avg) obtained at various collision energies. (b) The plot of [PA(apparent)-PA(avg)]/RT _{eff} versus 1/RT _{eff} .	114

LIST OF SCHEMES

Scheme 2.1. Proposed scheme for the reaction of $O^{\bullet-}$ with acetone.....	27
Scheme 2.2. Proposed scheme the reaction of $O^{\bullet-}$ with 3-pentanone.....	29
Scheme 2.3. Proposed scheme for the reaction of $O^{\bullet-}$ with cyclopentanone.....	32
Scheme 2.4 Proposed scheme for the reaction of $O^{\bullet-}$ with 2-butanone.	35
Scheme 2.5. Proposed scheme for the reaction of $O^{\bullet-}$ with cyclohexanone.....	38
Scheme 2.6. Proposed scheme for the reaction of $O^{\bullet-}$ with 2,4-dimethyl-3-pentanone.	40
Scheme 2.7. Proposed scheme for the reaction of $O^{\bullet-}$ with 3,3-dimethyl-2-butanone.	42
Scheme 2.8. Proposed scheme for the reaction of $O^{\bullet-}$ with a generic ketone, M.	43

DEDICATION

This thesis is dedicated to my family for their unconditional support through all these trying years.

PREFACE

I would like to express my gratitude for the multitude of people who have been of tremendous help during the course of my PhD program. First and foremost, I would like to express my sincerest appreciation and admiration for my advisor, Dr. Joseph Grabowski, who I am indebted forever. It was Dr. Grabowski who introduced me to the fascinating world of mass spectrometry and provided the necessary guidance and encouragement to overcome obstacles throughout my graduate study. More importantly, I learned from him the value of independent work and critical analysis, values that not only helped make me a better scientist but also a better person overall.

I would like to express my special thanks to Dr. Kasi Somayajula for the privilege to work for the departmental mass spectrometry facility for more than three years, where he provided invaluable insight and knowledge about mass spectrometry. I will sorely miss him not only as professional colleague but also a friend.

I would like to thank for the support and friendship from my groupmates: Abdil Ozdemir, Chris Taormina, Mark Morris, Kevin Davies, Daniel Owusu and Kyle Tilger and fellow graduate student Zeeshan Ahmed.

Finally I would also like to thank the personnel from electronic, machine and glass shop for helping me solving the problems with instruments.

Chapter 1 Introduction

1.1. Overview

The main goal of this thesis is to explore novel applications of gas-phase ion-molecule reactions in solving analytical problems. The scope of this thesis covers the application of ion-molecule as a chemical ionization means to generate novel organic intermediates, as a promising alternative to peptide sequence identification, and as a method to obtain thermochemical properties of peptides.

Gas-phase ion-molecule reactions long have been used in the study of intrinsic properties of organic compounds in a solvent free environment. Solvent effects play an essential role in determining a molecule's chemical reactivity and molecular conformation; unfortunately, they can also mask the properties of organic molecules and make the detailed study of chemical reactions difficult. Gas-phase ion-molecule reactions, free from the complication of solvent and counter-ion effects, can be used to elucidate the intrinsic reactivities of organic molecules, including reaction kinetics, product ion distributions, reaction mechanisms and thermodynamic properties. The valuable information obtained from experimental ion-molecule reaction investigations together with theoretical efforts has made a significant impact on the development of physical-organic chemistry.

Based on the knowledge obtained from ion-molecule fundamental studies, ion-molecule reactions have also been increasingly utilized as an analytical tool to solve various problems, such as preparing novel reagent ions for chemical ionization mass spectrometry, probing molecular structures and differentiating isomers [1]. Recently, ion-molecule reactions in conjunction with modern ionization techniques have also been successfully employed as probes

to unravel the gas-phase structures/conformations of peptides and proteins and to obtain thermochemical properties most relevant to their gas-phase behavior [2]. In this thesis, the focus on ion-molecule reaction study is placed on the pursuit of novel ion-molecule applications. In the meantime, several fundamental aspects of selected ion-molecule reactions, including reaction kinetics, product branching ratios and reaction mechanisms, are also investigated.

Chapter 2 presents a detailed study of the reactions between atomic oxygen radical anion ($O^{\bullet-}$) and selected ketones to explore an ion-molecule strategy to distonic radical anions of ketones. Distonic radical anions can be considered as precursors of diradicals, which are of great interest in organic chemistry but difficult to synthesize experimentally. The $O^{\bullet-}$ reactions provide a promising synthetic pathway to distonic radical anion due to the high reactivities of $O^{\bullet-}$ towards most organic molecules via proton transfer, hydrogen transfer and $H_2^{+\bullet}$ transfer [3]. Unique information about a diradical can be obtained from its corresponding radical anion via negative ion photonelectron spectroscopy. The $O^{\bullet-}$ /ketone reaction study presented in this chapter demonstrates that radical anions of interest can be successfully generated via $O^{\bullet-}$ chemical ionization. Furthermore, the detailed aspects of $O^{\bullet-}$ /ketone reactions, including reaction kinetics and product distribution, are revealed by a thorough study. The $O^{\bullet-}$ /ketone reactions are carried out in a flowing afterglow (See section 1.2 for the detailed description of the flowing afterglow used in this study), which is an ideal device for measuring ion-molecule reaction rate constants, investigating chemical reactivities, and deriving thermochemical properties among other things.

In Chapter 3, another type of ion-molecule reaction, the endothermic reaction, is investigated to explore a strategy targeting the cleavage of the peptide backbone amide bond to obtain primary sequence information of peptides. A chemical reaction that can cleave the peptide amide bond in the gas-phase is an attractive alternative to normal peptide gas-phase sequencing

approach, which utilizes nonselective energetic collision induced dissociation (CID) to produce fragments from precursor ions. Various studies have been undertaken to explore the possibilities of sequencing peptides via ion-molecule reactions [4, 5]. In this study, the ion-molecule reactions between positively charged peptide ions, generated from electrospray ionization, and potential cleaving reagents are examined in a custom-built electrospray triple quadrupole instrument. As opposed to the flowing afterglow, where reactions might suffer from interferences from metastable species and other ions generated in the ion source, a triple quadrupole instrument [6, 7] is capable of performing tandem experiments. In the most common approach in a triple quadrupole tandem experiment, a reactant ion is mass isolated by the first quadrupole and allowed to react with a neutral substrate in the second quadrupole (which might instead be an octopole) at controlled kinetic energies. The product ions and unreacted ions are mass analyzed by the third quadrupole. Structure characterization and isomeric ion differentiation have been demonstrated in this fashion on triple quadrupole instruments [8-11]. In current work, the study of ion-molecule reactions between peptide ions and cleavage reagents were performed by allowing the peptides ion, generated from the electrospray ionization source, to react with volatile neutral reagents in the octopole collision chamber under various kinetic energies.

Traditionally, ion-molecule reactions are used to investigate small molecules ionized by an electron ionization or chemical ionization source. Recently, ion-molecule reactions have been increasingly applied to peptides ionized from electrospray ionization sources. For example, in a series of related experiments, Lifshitz and co-workers [12-16] utilized an electrospray flow tube reactor, first introduced by Poutsman et al. [17], to measure the H/D exchange rates between protonated peptide ions and deuterium exchange reagents at thermal conditions. Proton transfer reaction involving singly and multiply charged peptides/proteins have also been extensively

studied to derive their proton affinity and gas-phase basicity, or to probe their gas-phase structures and conformations [2, 18]. The study carried out in Chapter 3 targets a more sophisticated ion-molecule reaction than the simple proton transfer reaction most commonly explored; the designed nucleophile-electrophile interactions between peptide ions and cleaving reagents are investigated targeting peptide amide bond cleavage. Strategies that minimize the competition from CID processes and proton transfers are explored and the reactions observed are discussed in terms of fundamental ion-molecule principle.

Chapter 4 measures the proton affinity, via the kinetic method, of leucine-enkephalin and methionine-enkephalin, which are two important brain neuropeptides. The proton affinity, one of the most fundamental thermochemical properties of a molecule and which plays a role in determining a molecule's ionization efficiency, is not known for either of these peptides. Equilibrium methods [19, 20] and bracketing methods [21] have been extensively used to obtain a molecule's proton affinity. The kinetic method, developed by Cooks et al. [22, 23], provides a simple but effective alternative to obtain proton affinities through the study of a unique type of ion-molecule reaction – unimolecular reaction. Moreover, non-volatile biological molecules can be studied by the kinetic method from where equilibrium methods are restricted. In this study, the proton affinities of leucine-enkephalin and methionine enkephalin are measured through the study of the dissociation of a proton bound heterodimer of a peptide with various reference compounds.

Finally, several thermochemical properties relevant to this thesis, including proton affinity, gas-phase basicity and electron affinity are listed separately as an appendix at the end of this thesis.

1.2. The flowing afterglow

A schematic diagram of the flowing afterglow (FA) instrument at the University of Pittsburgh as used in this work is shown in Figure 1.1. The flowing afterglow consists of three main regions: the ion generation region, the ion-molecule reaction region, and the ion detection region. In the ion generation region, there is a simple chemical ionization source; reagent ions are generated by electron ionization on precursor gases, introduced together with buffer gas via a stainless steel precursor gas manifold. The reaction region is essentially a stainless steel flow tube (150 cm length and 7.3 cm i.d.) with ten uniformly spaced neutral inlet ports. The detection region is separated from the flow tube by a nose cone with a 1.5 mm i.d. orifice. The detection region is composed of two chambers: the middle chamber, which is immediately after the orifice plate, is pumped by a 6" diffusion pump with a pumping speed of 700 l s^{-1} ; the rear chamber, where the quadrupole mass filter and ion detector are located, is pumped by a 4" diffusion pump with a pumping speed of 250 l s^{-1} . A conversion dynode and an electron multiplier are used to detect ions. During an experiment, a large flow of helium ($100\text{-}150 \text{ STP l s}^{-1}$) is pumped through the flow tube by a mechanical pump booster system with a pumping speed of 653 l s^{-1} . The operational pressure is maintained around 0.3 Torr and the velocity of helium in the flow tube is around 8000 cm s^{-1} . The helium serves two main purposes: (1) to transport ions and neutrals from their introduction points down to the flow tube to the analysis region; (2) to ensure the reacting species are thermally equilibrated to the buffer gas temperature. At the end of the flow tube, a fraction of the reaction mixture is sampled through the orifice into the detection region where the typical pressure is $(1\text{-}3)\times 10^{-5}$ Torr in the middle chamber. The gaseous mixture experiences a sudden expansion and the ion-molecule reactions are quenched by preventing further ion-molecule encounters. Thus, the reaction distance can be defined as the distance from

the neutral inlet to the sampling orifice and since the velocity of gases in the flow tube is well-defined and measured the reaction time can be derived. The voltages applied on the nose cone and the extracting plate are kept as small as possible to minimize any collision induced dissociations during the ion sampling from the higher pressure flow tube into the low pressure analysis region.

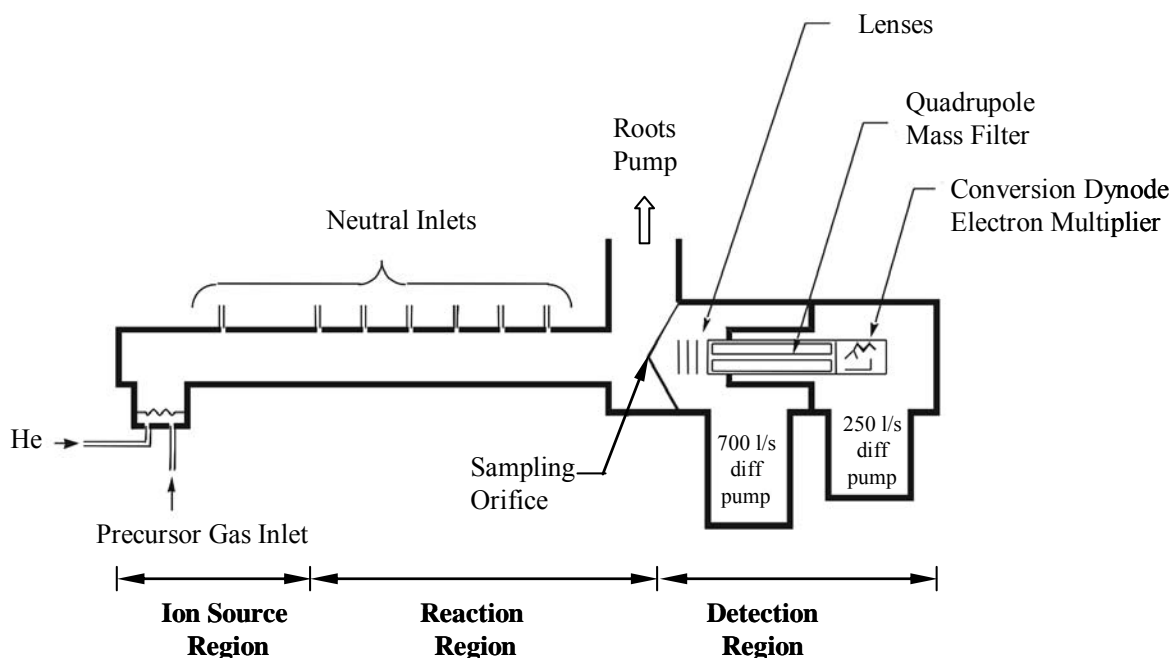


Figure 1.1. A schematic diagram of the flowing afterglow apparatus at the University of Pittsburgh.

Note that the flowing afterglow is a room temperature device: reactions in the flowing afterglow are carried out in a buffer gas with a pressure of 0.3-1.0 Torr, and ions generated by any mechanism are thermally equilibrated via numerous ion-helium collisions to room temperature. One consequence is that endothermic reactions are too slow to be observed in a flowing afterglow.

1.3. Gas phase ion-molecule reaction coordinate diagrams

The energetics of an ion-molecule reaction in the gas-phase differs from ion-molecule reactions in the condensed-phase. In solution, ions are surrounded by solvent molecules; in the gas-phase, ions and molecules can interact directly with each other directly through ion-induced dipole moment and/or ion-permanent dipole moment interactions.

The reaction coordinate diagram for an ion-molecule reaction can be illustrated by the double-well potential model as described by Brauman and co-workers [25-27], illustrated in Figure 1.2 for a nucleophilic substitution reaction $X^- + RY \rightarrow RX + Y^-$. In the first step, ion X^- and neutral RY are attracted to each other by ion-dipole and/or ion-induced dipole interactions to form a reactant collision complex $[X^- \cdots RY]$. Upon the ion-molecule encounter, the reactant complex gains solvation energy of 15-20 kcal mol⁻¹ [24]. Driven by this solvation energy, the reactant complex $[X^- \cdots RY]$ transforms, via a transition state $[X \cdots R \cdots Y]^\ddagger$, to product complex $[XR \cdots Y^-]$. Finally, the products RX and Y^- are separated by overcoming the solvation energy between RX and Y^- that has similar magnitude as gained during the formation of the reactant complex. The total energy of the system is illustrated by the uppermost dashed line in Figure 1.2.

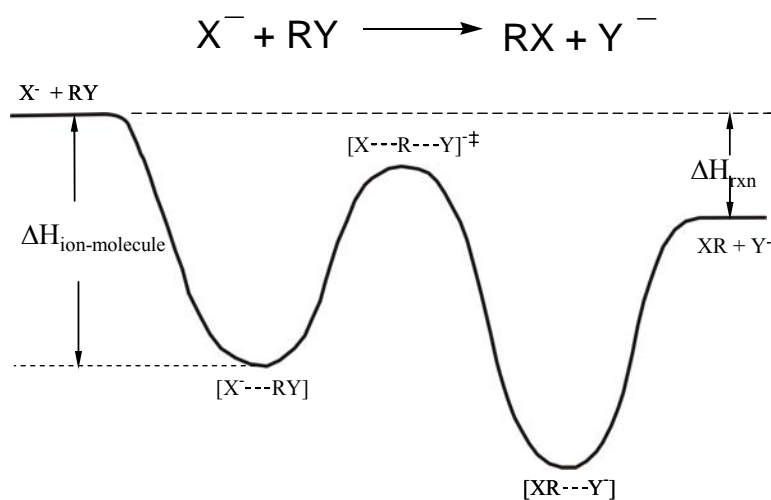


Figure 1.2. Reaction coordinate diagram for a nucleophilic substitution reaction in the gas-phase.

1.4. Ion-molecule reaction efficiencies

Since gas-phase ion-molecule reactions often proceed at or near collision rates, it is useful to discuss reaction efficiency which is the probability of a reaction occurring per unit collision. The reaction efficiency (EFF) of an ion-molecule reaction is defined as the ratio of observed reaction coefficient, k_{obs} and collision rate coefficient, k_{coll} (eq. 1.1).

$$EFF = k_{obs}/k_{coll} \quad (1.1)$$

Several theories have been developed to calculate the ion-molecule collision rate coefficient [28]. The *Langevin theory* assumes the attractive potential between an ion and a neutral molecule only comes from ion-induced dipole moment:

$$V_L(r) = \frac{1}{2}(\alpha q^2 / r^4) \quad (1.2)$$

where, q is the charge of the ion, α is the polarizability of the molecule, and r is the ion-molecule separation distance. Based on the attractive potential shown in eq. 1.2, the collision rate coefficient is expressed as:

$$k_L = 2\pi q(\alpha / \mu)^{1/2} \quad (1.3)$$

where μ is the reduced mass.

The *Locked dipole theory* further develops *Langevin theory* by including the contribution from the attraction potential caused by ion-permanent dipole moment interaction as shown in eq. 1.4:

$$k = (2\pi q / \mu^{1/2})[\alpha^{1/2} + \mu_D(2 / \pi kT)^{1/2}] \quad (1.4)$$

where μ_D , is the dipole moment of the molecule and k is Boltzmann's constant. This theory simplifies the additional ion-dipole moment interaction by assuming that the dipole of the molecule "locks in" towards the ion. The *Average Dipole Orientation (ADO) theory* considers that "locking in" does not necessarily occur. A parameter is introduced to reflect the effectiveness of the charge "locking in" of the dipole. Thus, the rate coefficient is expressed as:

$$k_{ADO} = (2\pi q / \mu^{1/2})[\alpha^{1/2} + c\mu_D(2/\pi kT)^{1/2}] \quad (1.5)$$

where, c is the dipole locking constant with a value between 0 (no locking) and 1 (complete locking). This constant is empirically determined. At constant temperature, c is only a function of $\mu_D/\alpha^{1/2}$.

A more widely used theory is the *trajectory calculation theory* developed by Su and Bowers [29]. This theory combines variational transition state theory and classical trajectory studies of ion-polar molecule capture collisions at thermal energy. In this theory, ions are treated as point charges, while polar molecules are treated as two-dimensional rigid rotors. A parameter K_{cap} is introduced to correct the collision rate calculated from *Langevin theory* (eq.1.6),

$$k_{Su} = K_{cap}(T_R, I^*) \times k_L \quad (1.6)$$

where $T_R = 2\alpha k_B T / \mu_D^2$, and $I^* = \mu_D I / \alpha q \mu$. (I is the moment of inertia of the neutral)

The empirical fit of the trajectory curve, based on large numbers of trajectories run for each combination of T_R and I^* , is shown in eq. 1.7:

$$K_{cap} = \begin{cases} 0.4767x + 0.6200; & x \geq 2, \\ \frac{(x + 0.5090)^2}{10.526} + 0.9754; & x \leq 2 \end{cases} \quad (1.7)$$

where $x = I/T_R^{1/2}$. This parameterized trajectory calculation theory is used to calculate collision rate coefficients in the current thesis work.

1.5. References

- [1] J.S. Brodbelt, Mass Spectrom. Rev. 16 (1997) 91-110.
- [2] M.K. Green and C.B. Lebrilla, Mass Spectrom. Rev. 16 (1997) 53-71.
- [3] J. Lee and J.J. Grabowski, Chem. Rev. 92 (1992) 1611-1647.
- [4] R.A. O'Hair, N.K. Androustopoulos, and G.E. Reid, Rapid Commun. Mass Spectrom. 14 (2000) 1707-1716.

- [5] R.A. O'Hair, *J. Mass Spectrom.* 35 (2000) 1377-1381.
- [6] R.A. Yost and C.G. Enke, *J. Am. Chem. Soc.* 177 (1978) 2274-2275.
- [7] J.V. Johnson, R.A. Yost, P.E. Kelley, and D.C. Bradford, *Anal. Chem.* 62 (1990) 2162-2172.
- [8] M.T. Kinter and M.M. Bursey, *J. Am. Chem. Soc.* 108 (1986) 1797-1801.
- [9] R.R. Pachuta, H.I. Kenttamaa, R.G. Cooks, T.M. Zennie, C. Ping, C.J. Chang, and J.M. Cassady, *Org. Mass Spectrom.* 23 (1988) 10-15.
- [10] W.J. Mehyerhoffer and M.M. Bursey, *Org. Mass Spectrom.* 24 (1989) 246-252.
- [11] W.J. Mehyerhoffer and M.M. Bursey, *Org. Mass Spectrom.* 24 (1989) 169-175.
- [12] G. Koster, M. Soskin, M. Peres, and C. Lifshitz, *Int. J. of Mass Spectrom.* 179/180 (1998) 165-171.
- [13] G. Koster and C. Lifshitz, *Int. J. of Mass Spectrom.* 182/183 (1999) 213-220.
- [14] A. Kogan, P. Ustyuzhanin, B.G. Reuben, and C. Lifshitz, *Int. J. of Mass Spectrom.* 213 (2002) 1-4.
- [15] G. Koster and C. Lifshitz, *Int. J. of Mass Spectrom.* 195/196 (2000) 11-19.
- [16] E. Levy-Seri, G. Koster, A. Kogan, K. Gutman, B.G. Reuben, and C. Lifshitz, *J. Phys. Chem. A* 105 (2001) 5552-5559.
- [17] J.C. Poutsman, R.A. Seburg, L.J. Chyall, L.S. Sunderlin, B.T. Hill, J. Hu, and R.R. Squires, *Rapid Commun. Mass Spectrom.* 11 (1997) 489-493.
- [18] E.R. William, *J. Mass Spectrom.* 31 (1996) 831-842.
- [19] R. Yamdagni and P. Kebarle, *J. Am. Chem. Soc.* 98 (1976) 1320-1324.
- [20] P. Kebarle, *Ann. Rev. Phys. Chem.* 28 (1977) 445-476.
- [21] J.L. Beauchamp, *Ann. Rev. Phys. Chem.* 22 (1971) 527-561.
- [22] R.G. Cooks, J.S. Patrick, T. Kotiaho, and S.A. McLuckey, *Mass. Spectrom. Rev.* 13 (1994) 287-339.
- [23] R.G. Cooks and P.S. Wong, *Acc. Chem. Res.* 31 (1998) 379-386.
- [24] J.E. Bartmess, *Ion-molecule Chemistry: the Roles of Intrinsic Structure, Solvation, and Counterions*, in: (Eds.), *Advances in Gas Phase Ion Chemistry*, 1996.
- [25] M.J. Pellerite and J.I. Brauman, *J. Am. Chem. Soc.* 102 (1980) 5993-5999.
- [26] W.E. Farneth and J.I. Brauman, *J. Am. Chem. Soc.* 98 (1976) 7891-7898.
- [27] W.N. Olmstead and J.I. Brauman, *J. Am. Chem. Soc.* 99 (1977) 4219-4228.

- [28] T. Su and M.T. Bowers, *J. Chem. Phys.* 58 (1973) 3027-3037.
- [29] T. Su and W.J. Chesnavich, *J. Chem. Phys.* 76 (1982) 5183-5185.

Chapter 2 Didehydro Radical Anions from Ketones via O⁻ Chemical Ionization

2.1. Introduction

Diradicals, an atom or molecule in which two electrons occupy two degenerate or nearly degenerate molecular orbitals [1], have been of great interest for a long time [2, 3]. One intriguing property of a diradical is the energy difference between its singlet and triplet states. Theoretical calculations and experiments show this energy spacing is typically small, around 2-5 kcal mol⁻¹ [4, 5]. For example, based on *ab initio* calculation, Power and Borden [6] predicted that cyclopentan-2-one-1,3-diyl is a ground state singlet, and that the singlet is both 4.3 kcal mol⁻¹ lower in energy than the ring closed form (bicycle[2,1,0]pentan-5-one) and 7.0 kcal mol⁻¹ below the triplet. However, direct synthesis of this diradical remains an unfulfilled challenge and thus its singlet-triplet energy spacing has not been measured experimentally yet. Distonic radical anions, with separated charge and radical sites [7, 8], can be considered as an one-electron reduction product of the corresponding diradical. Gas-phase chemistry and negative ion photoelectron spectroscopy (NIPES) have been combined to provide a new method to study diradicals [9-11]. One example of a diradical studied in this fashion is tetramethyleneethane (TME). Lee et al. reported that the 1,4-radical anion of TME was synthesized in the gas-phase via O⁻ chemistry [12]; NIPES experiments by Clifford et. al. revealed that TME is a ground state singlet [11]. We wish to explore this strategy of gas-phase synthesis of the 1,3-distonic radical anion of cyclopentanone so that the singlet-triplet energy splitting of cyclopentan-2-one-1,3-diyl can be measured by NIPES.

Existing approaches used to synthesize radical anions in the gas-phase include dissociative electron attachment, electron transfer, and ion-molecule reactions [13]. One

particularly promising synthetic pathway among these approaches to radical anions is through chemical ionization of an appropriate neutral molecule by means of the atomic oxygen radical anion $O^{\bullet-}$ [14]. Because of high proton and hydrogen atom affinities, $O^{\bullet-}$ possesses the abilities to abstract H_2^{*+} from a broad range of molecules to produce a didehydro radical anion $[M-2]^{\bullet-}$ of the corresponding neutral [15]. This unique reaction has been utilized to synthesize a variety of radical anions, including the *o*-benzene radical anion from benzene [16], the aromatic radical anions from pyridine, furan, thiophene, pyrrole and 1,3-cyclopentadiene [17], the radical anion of bicycle[1.1.0]but-1(3)-ene [18] and cubane [19], the distonic radical anion from thiomethoxyacetonitrile [20, 21], and the radical anion of 6,6-dimethylfulvene [22].

Several studies have noted some aspects of chemical ionization of ketones with $O^{\bullet-}$. For example, Harrison and Jennings reported the observation of $[M-H]^-$ and $[M-2H]^{\bullet-}$ products from $O^{\bullet-}$ with a number of cyclic and acyclic ketones using the ion cyclotron resonance (ICR) technique [23]. For the acetone reaction, they noticed that the ratio of $[M-H]^-/[M-2H]^{\bullet-}$ changed from 0.2 to 1.2 as the pressure of acetone increased from 1×10^{-5} to 3×10^{-4} Torr in their ICR. They attributed the ratio change to an increase in the $[M-H]^-$ due to a secondary reaction between HO^- and acetone. Dawson and co-workers investigated the reaction between $O^{\bullet-}$ and 1,1,1-*d*₃-acetone with an ICR and confirmed the production of both 1,1- and 1,3- H_2^{*+} abstraction products [24]. Marshall and co-workers allowed $O^{\bullet-}$ to react with C₄-C₇ carbonyl compounds, in a hybrid BEqQ instrument, and reported the deprotonated ketone ($[M-H]^-$) to be the base peak, along with lesser amounts of $[M-2H]^{\bullet-}$ and other ions, in their spectra [25]. These qualitative reports demonstrate that radical anions can be synthesized through $O^{\bullet-}$ chemistry. Unfortunately, none of the techniques used to date have examined the reactions at thermal energies (300K), and

no studies provide a detailed examination of the quantitative aspects of the $O^{\bullet-}$ chemical ionization process of ketones.

The flowing afterglow technique was introduced by Ferguson and co-workers in 1963, at the National Oceanic and Atmospheric Administration (NOAA) laboratory in Boulder, CO [26, 27]. Initially, this technique was developed for the measurement of ion-molecule reaction rate constants; it has been improved and widely used for studying all aspects of ion-molecule reactions in gas-phase. A detailed discussion of the technique, along with descriptions of various instrument configurations, has been provided by Graul and Squires [28]. A valuable feature of the flowing afterglow technique is that the ion-molecule reactions are carried out in a field-free region, in a buffer gas at a pressure of ~ 0.3 Torr. Excess internal or kinetic energy of ions generated by any mechanism in such an instrument is rapidly removed by collisions with the buffer gas. It has been the case that $O^{\bullet-}$ experiments in an ICR or a sector instrument involve translationally hot ions because of lack of collisional cooling [29]. We wish to present a complete mechanistic description of the reaction of $O^{\bullet-}$ with prototypical ketones, as studied with the flowing afterglow method.

2.2. Experimental

The flowing afterglow used for these studies has been described in detail previously (Chapter 1 and [30]); only those experimental details novel or key to this work will be included here. High purity helium (4.7 grade) was further purified prior to use by passing it through a molecular sieve-packed trap immersed in liquid nitrogen. Sufficient helium was used, in conjunction with the 7.3 cm diameter flow tube and 653 l s^{-1} mechanical booster system, to maintain the flow tube pressure at 0.3 Torr. Trace amounts of nitrous oxide (N_2O , 4.8 grade),

used as the precursor to form $\text{O}^{\bullet-}$ via dissociative electron attachment, was added along with the helium through the simple electron ionization source of the flowing afterglow. The amount of added N_2O was carefully titrated in each experiment to maximize $\text{O}^{\bullet-}$ production (eq. 2.1) and to minimize the fast reaction between $\text{O}^{\bullet-}$ and N_2O (eq. 2) [31]. For all experiments, 2 mTorr of Ar (4.8 grade) was added to the flow tube 15 cm downstream from the ion source and 22.2 cm upstream from the beginning of the reaction region, to quench any remaining metastable helium atoms prior to their entry into the reaction region (eq. 2.3) [32].



All organic neutrals, except for 2,2,5,5-*d*₄-cyclopentanone (supplied by Prof. W. T. Borden), were obtained from commercial suppliers. Each liquid sample was subjected to several freeze-pump-thaw cycles to remove dissolved gases and volatile impurities. The reaction of each organic compound was studied qualitatively to understand its reactivity. A sub-set of the compounds were then identified for in-depth studies, which entailed separate, replicate experiments to measure either the bimolecular rate coefficient or the product branching ratio.

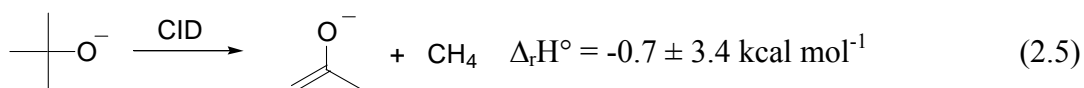
The rate coefficients were determined by monitoring the disappearance of $\text{O}^{\bullet-}$ as a function of the reaction distance, under pseudo-first-order reaction conditions. In the well-characterized flow tube, reaction distance is directly proportional to the reaction time [30]. All rate coefficients were derived from semi-logarithmic plots as described previously [17]. The rate coefficients reported here are the averages of at least five independent experiments conducted over several different days. The error bars reported are the standard deviations of the replicate

measurements. We have previously estimated the absolute accuracy of the kinetic measurement to be 20% [17]. To make better chemical sense of the observed rate coefficients for these very rapid reactions, we prefer reaction efficiency, which is the ratio of the observed rate coefficient to the estimated collision-limited rate coefficient. For this purpose, we employed the parameterized trajectory theory developed by Su and Chesnavich [33] to estimate the collision limited rate coefficient. The parameters (dipole moments and polarizabilities) were obtained from standard compilations when possible [34]. For several molecules, polarizabilities were estimated via the Lorentz-Lorenz equation and dipole moments were estimated from a homologous series of molecules with related structures and known dipole moments (See Table 2.1 for details).

Branching ratios were obtained by monitoring product ion intensity changes as a function of the extent of the reaction being examined [35]. In all cases, small corrections were made to the raw data to explicitly account for contributions from any HO^- impurity in the reactant ion spectrum, and for overlap of signals due to isotopic contributions from adjacent ions, as described next. A small amount of HO^- is always present whenever we generate $\text{O}^{\bullet-}$ in our flowing afterglow [30]. Hydroxide is also a product from many $\text{O}^{\bullet-}$ reactions, and is quite reactive (via proton abstraction) with the ketones examined here. We used our measured rate coefficient of a given $\text{O}^{\bullet-}$ /ketone reaction as the rate coefficient of the HO^- /ketone reaction to correct the observed HO^- signal to that representing only the HO^- formed as a product in the $\text{O}^{\bullet-}$ ketone reaction. We used the same data to discount the observed signal for deprotonated ketone by the amount of the contaminant hydroxide that had reacted (note, HO^- reacts with a ketone only via a proton transfer pathway). We next used a table of isotope neutral abundances [36] to correct adjacent m/z signals for coincidental overlaps of discrete chemical species due to isotopes. Such coincidental overlaps are most important when the yield of the $[\text{M}-2\text{H}]^{\bullet-}$ species

is high. Finally, for all product ions, data was only collected for the most abundant monoisotopic peak, necessitating a minor correction, again using the natural abundance table, to explicitly account for all naturally occurring isotopes. The corrected, normalized product ion intensities were plotted versus the change in reactant ion concentration, to give the branching ratio plot; the slopes of these curves extrapolated to zero reaction gives the primary product yield, while the shapes of curves at long reaction time provides information about any secondary reactions that are occurring. The product distribution reported here are the averages of at least two independent branching ratio experiments.

Qualitative collision induced dissociation (CID) experiments were carried out by dramatically increasing the nose cone potential as described by Baranov and Bohme [37]. The nose cone voltage was increased to accelerate the ions in the presence of helium, resulting in energetic collision that might lead to fragmentation. As the nose cone potential was systematically stepped, all subsequent focusing lens potentials were re-tuned to maximize the signal. The limit on the nose cone potential was defined by complete loss of ion signal. The collision-induced dissociation of *tert*-butoxide anion (formed via electron ionization of di-*tert*-butyl peroxide, eq. 2.4) according to eq. 2.5, was used to demonstrate the method.



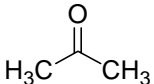
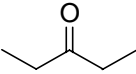
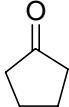
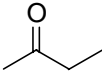
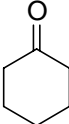
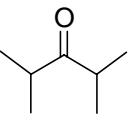
2.3. Results

The measured bimolecular rate coefficients for the reaction of $\text{O}^{\bullet-}$ with acetone, cyclopentanone, 3-pentanone, 2-butanone, cyclohexanone, and 2,4-dimethyl-3-pentanone are summarized in Table 2.1. Representative semi-logarithm kinetic plots used to derive individual rate coefficients are shown in Figure 2.1. All reactions examined are rapid, possessing reaction efficiencies of 40% or greater. The branching ratios for the six selected ketones are summarized in Table 2.2, wherein the product ions are categorized by reaction channels.

The enthalpy values used in this work are compiled in Table 2.3. For each ketone, the enthalpy of its conjugate base is derived from the gas phase acidity of the ketone. The enthalpy of the $[\text{M-H}]^{\bullet}$ radical of a ketone is derived from the bond dissociation energy (BDE) of the relevant α hydrogen-carbon bond. When the BDE is unavailable for a specific ketone, an approximate value based on an analog to that ketone is used. In all such cases, notes are indicated in the table. The enthalpy of a ketone 1,3-distonic radical anion is derived by assuming that the BDE of a C-H on the α carbon opposite of that from which the proton has been abstracted is the same as the BDE in the parent ketone. The enthalpies of a radical anion with charge and radical on the same carbon is estimated from a deprotonation reaction of a ketone $(\text{M-H})^{\bullet}$ radical. The enthalpy change of such reaction is approximated from the heterolytic dissociation reaction enthalpy of NCCH_2^{\bullet} (eq. 2.6), which is $378.4 \pm 4.0 \text{ kcal mol}^{-1}$ [38]. The error bars for these estimated values are the accumulated error from each step and are listed in Table 2.3.



Table 2.1. Reaction rate coefficients for O⁻ with selected ketones in the gas phase at room temperature

Reactant neutral	$\Delta H_{\text{acid}}^{\circ}$ ^a (kcal mol ⁻¹)	$k_{\text{obs}}^{\text{b}}$ (cm ³ mol ⁻¹ s ⁻¹)	# of experiments	Efficiency (μ_{D} ; α) ^c	Efficiency per α -H
	369.1 ± 2.1	2.93 (± 0.77) × 10 ⁻⁹	5	0.700 (2.88; 6.4)	0.12
	368.6 ± 2.2	1.76 (± 0.05) × 10 ⁻⁹	7	0.419 (2.78 ^d ; 9.93)	0.10
	368.0 ± 4.2	2.04 (± 0.40) × 10 ⁻⁹	7	0.433 (3.3; 9.13 ^e)	0.11
	367.2 ± 2.4	2.86 (± 0.57) × 10 ⁻⁹	6	0.690 (2.78; 8.13)	0.14
	365.8 ± 2.3	2.74 (± 0.18) × 10 ⁻⁹	5	0.607 (2.87; 11.0 ^e)	0.15
	364.8 ± 2.3	1.83 (± 0.26) × 10 ⁻⁹	5	0.435 (2.68 ^f ; 13.5 ^e)	0.22

a. [38]

b. Errors listed are one standard deviation of the replicate experiments.

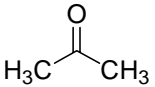
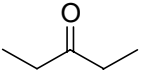
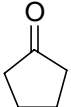
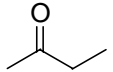
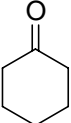
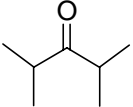
c. Efficiency is defined in the text. Units: μ_{D} , Debye; α , 10⁻²⁴ cm³. Values are taken from ref. [34] unless indicated.

d. Calculate via Cache (V. 6.01) at B88-LYP level of theory.

e. Calculated from Lorentz-Lorenz equation.

f. From Beilstein Crossfire Database (search performed on July 2003).

Table 2.2. Summary of the primary product distributions for the reaction of $O^{\bullet-}$ with selected ketones ^a

Reactant Neutral	Observed (M-2H) ⁻	Fragmentation	HAT (HO ⁻)	PT (M-H) ⁻	Add-Elim
	54%	16% (HCCO ⁻)	12%	15%	3% (CH ₃ COO ⁻)
	44%	0	10%	25%	21% (CH ₃ CH ₂ COO ⁻)
	48%	0	21%	31%	0
	42%	4% (HCCO ⁻) 2% (CH ₃ CCO ⁻)	17%	30%	2% (CH ₃ COO ⁻) 3% (CH ₃ CH ₂ COO ⁻)
	47%	0	18%	35%	0
	3%	0	17%	15%	65% ((CH ₃) ₂ CHCOO ⁻)

a. Branching ratio results are the average from at least two independent experiments carried out on two different experiment days.

Table 2.3. Enthalpies used in this work.

Species	$\Delta_f H^\circ_{298}$ (kcal mol ⁻¹)	Reference
H ⁺	367.5	a
H [•]	52.1	b
O ^{•-}	25.85 ± 0.2	b
HO ⁻	-32.8 ± 0.2	b
HO [•]	9.3	b
H ₂ O	-57.8	b
CH ₃ [•]	34.8	b
C ₂ H ₅ [•]	28.5 ± 0.5	b
(CH ₃) ₃ C [•]	1.1	b
CH ₃ COO ⁻	-126.6 ± 2.6	b
CH ₃ CH ₂ COO ⁻	-125.4 ± 2.3	b
HCCO ⁻	-13.7 ± 2.2	b
NCCH ⁻	69.3 ± 3.7	b
NCCH ₂ [•]	58.2 ± 2.7	b
Acetone & related species:		
C ₃ H ₆ O	-52.23 ± 0.14	b
C ₃ H ₅ O ⁻	-50.6 ± 2.0	b
C ₃ H ₅ O [•]	-5.9 ± 2.0	c
C ₃ H ₄ O ^{•-} (distonic)	-4.3 ± 8.0	e
3-Pentanone & related species		
C ₅ H ₁₀ O	-60.6 ± 0.2	a
C ₅ H ₉ O ⁻	-59.5 ± 2.0	b
C ₃ H ₉ O [•]	-22.7 ± 2.0	d
C ₅ H ₈ O ^{•-} (distonic)	-21.6 ± 8.0	e
C ₅ H ₈ O ⁻	-11.6 ± 8.0	f
Cyclopentanone & related species		
C ₅ H ₈ O	-47.2	b
C ₅ H ₈ O ⁻	-46.7 ± 4.0	b
C ₅ H ₈ O [•]	-9.2 ± 2.0	d
C ₅ H ₈ O ^{•-} (distonic)	-4.8 ± 8.0	e
C ₅ H ₈ O ⁻	1.3 ± 8.0	f
C ₅ H ₅ O ₂ ⁻	-95 ± 4.0	g
C ₅ H ₉ [•]	26.1 ± 1.0	b
2-Butanone & related species		
C ₄ H ₈ O	-57.02 ± 0.20	b
C ₄ H ₇ O ⁻	-57.5 ± 3.0	b
C ₄ H ₇ O [•]	-16.8 ± 2.0	c
C ₄ H ₆ O ^{•-} (distonic)	-17.3 ± 8.0	e

Cyclohexanone & relative species		
C ₆ H ₁₀ O	-55.23 ± 0.21	b
C ₆ H ₉ O ⁻	-50.7 ± 4.3	b
C ₆ H ₉ O [•]	-17.1 ± 2.0	d
C ₆ H ₈ O ^{+•} (distonic)	-12.8 ± 8.0	e
C ₆ H ₈ O ^{-•}	6.0 ± 8.0	f
2,4-Dimethyl-3-pentanone & relative species		
C ₇ H ₁₄ O	-74.4 ± 0.3	b
C ₇ H ₁₃ O ⁻	-77.1 ± 3.0	b
C ₇ H ₁₃ O [•]	-44.5 ± 5.0	d
C ₇ H ₁₂ O ^{+•} (distonic)	-47.2 ± 8.0	e
3,3-Dimethyl-2-butanone & relative species		
C ₆ H ₁₂ O	-69.7 ± 0.21	b
C ₆ H ₁₁ O ⁻	-70.3 ± 3.0	b
C ₆ H ₁₁ O [•]	-23.4 ± 2.0	d
C ₄ H ₉ COO ⁻	-139.3 ± 2.2	b

- a. Lias, S. G., Bartmess, J. E., Liebman, J. F., Holmes, J. L. Levin, R. D., and Mallard, W. G, J. Phys. Chem. Ref. Data, 17 (1988) (Suppl. 1)
- b. [38].
- c. [34].
- d. Estimated from BDE (H-CH₂COCH₃) and BDE (H-CH(CH₃)COCH₃).
- e. Derived by assuming that the BDE of an α C-H bond of the deprotonated ketone anion is approximately the same as that of a ketone neutral.
- f. Estimated from $\Delta_f H^\circ(\text{NCCH}_2^\bullet) = 58.2 \pm 2.7 \text{ kcal mol}^{-1}$ and $\Delta_f H^\circ(\text{NCCH}^{\bullet-}) = 69.3 \pm 3.7 \text{ kcal mol}^{-1}$.
- g. Estimated from 2,3-butanedione anion, $\Delta_f H^\circ(\text{CH}_3\text{COCOCH}_2^-) = -94.6 \text{ kcal mol}^{-1}$

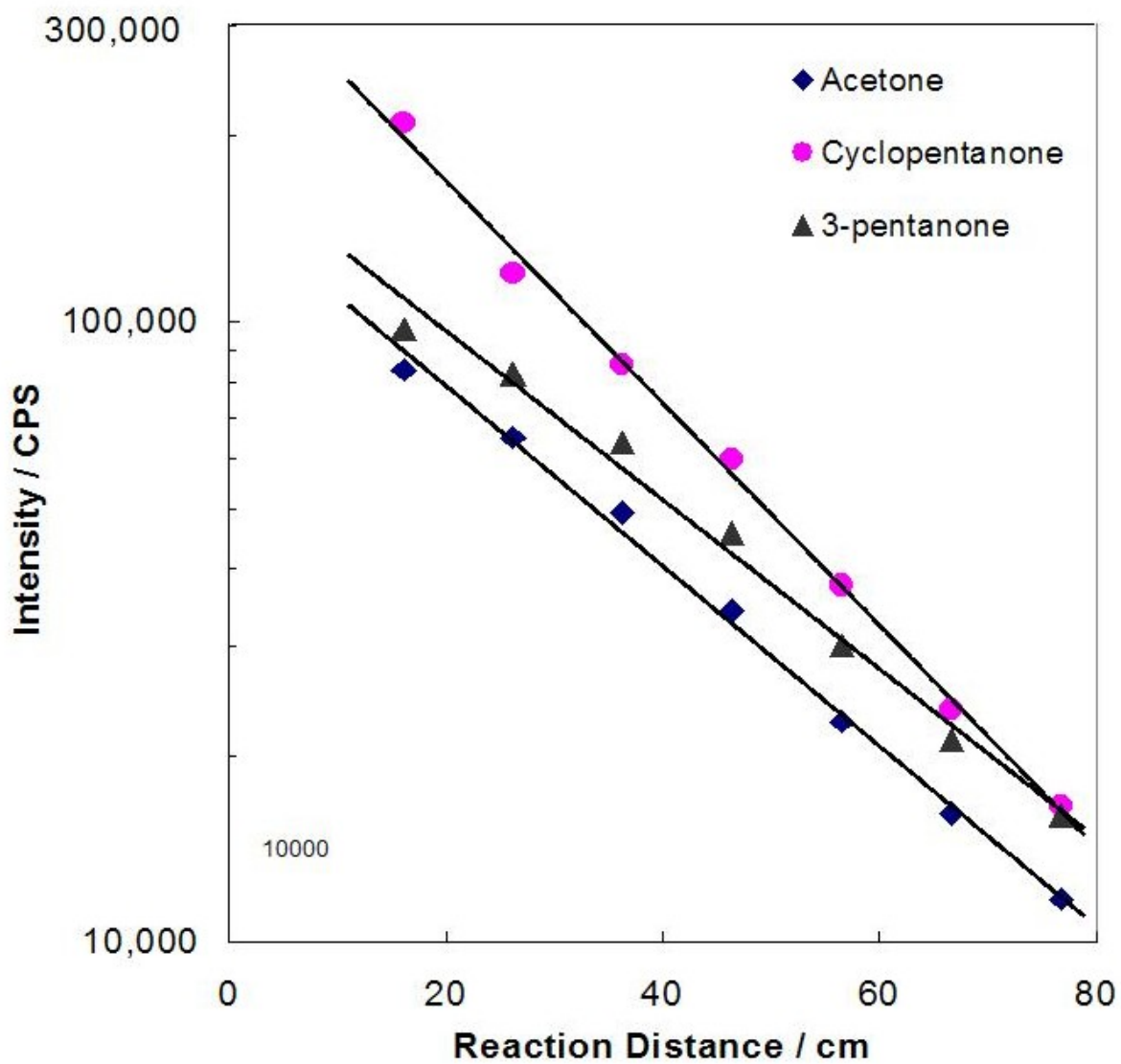


Figure 2.1. Representative semi-logarithm plots of ion intensity vs. reaction distance for the reactions of O^+ and several ketones. For these individual experiments, the number of half lives for which the reaction was followed in order to obtain the rate coefficient were: acetone, 2.8; cyclopentanone, 3.7; and 3-pentanone 2.6.

2.3.1. Acetone

The products observed from the reaction of atomic oxygen radical anion with acetone are m/z 17, 41, 56, 57, and 59. When acetone is replaced with d_6 -acetone, the products are observed at m/z 18, 42, 60, and 62. Based on these data, and the thermochemical considerations discussed below, the primary product ions from acetone are identified as HO^- , HCCO^- , $\text{C}_3\text{H}_4\text{O}^-$, $\text{CH}_3\text{C}(\text{O}^-)=\text{CH}_2$, and CH_3CO_2^- respectively. Note that for the d_6 -acetone reaction, two of the observed product ions from h_6 -acetone (m/z 57 and 59) are shifted to the same m/z value of 62 ($\text{CD}_3\text{C}(\text{O}^-)=\text{CD}_2$ and CD_3CO_2^-). The quantitative branching ratio experiments on acetone, an example of which is shown in Figure 2.2, leads to relative yields of 12% HO^- , 16% HCCO^- , 54% $\text{C}_3\text{H}_4\text{O}^-$, 15% $\text{CH}_3\text{C}(\text{O}^-)=\text{CH}_2$, and 3% CH_3CO_2^- . Figure 2.2 documents that facile secondary reactions are occurring as demonstrated via the curvature in yields of the m/z 17, 56, and 57 as a function of the extent of the primary reaction. The curves demonstrate that both HO^- and $\text{C}_3\text{H}_4\text{O}^-$ react with a second equivalent of acetone via proton transfer reactions, giving additional $\text{CH}_3\text{C}(\text{O}^-)=\text{CH}_2$, and that HO^- reacts faster by proton abstraction from acetone than $\text{C}_3\text{H}_4\text{O}^-$ does.

To gain additional insight into the identity of the $\text{C}_3\text{H}_4\text{O}^-$ ion and the source of the HCCO^- ion, we attempted to induce fragmentation of the $\text{C}_3\text{H}_4\text{O}^-$ ion during the sampling process. Over the energy range that can be successfully probed (up to 20V on the nose cone, as compared to a normal sampling potential of 0-1V), we were unable to change the m/z 56 to 41 ion intensity ratio. These results, coupled with the “matched” increase in m/z 57 with the decreases in m/z 56 and 17 (e.g. Figure 2.2), are interpreted to mean that all 1,1- H_2^+ -abstraction products immediately fragment to m/z 41 whereas the 1,3- H_2^+ -abstraction product is stable against fragmentation (in the energy region we examined) but is reactive with acetone (via a

proton transfer process). All these observations are combined, along with thermochemical considerations, to create the reaction diagram presented in Scheme 2.1, and which includes both primary and secondary reaction processes. The yields and scheme reported herein for the acetone reaction are consistent with the limited qualitative results previously reported in the literature, as noted in the introduction including the 1,1,1-*d*₃-acetone qualitative reaction [24].

2.3.2. 3-Pentanone

The products observed from the reaction of atomic oxygen radical anion with 3-pentanone are *m/z* 17, 73, 84, 85 and 99, which correspond to HO⁻, CH₃CH₂COO⁻, C₅H₈O^{•-}, C₅H₉O⁻ and C₅H₇O₂⁻. A representative branching ratio plot is shown in Figure 2.3; among other things, it demonstrates that CH₃CH₂COO⁻ (*m/z* 73) is only a primary product ion. A trace amount of C₅H₇O₂⁻ (*m/z* 99) is observed and is shown (in the branching ratio plot) to be only a secondary reaction product. The curvature of the HO⁻, C₅H₈O^{•-}, and C₅H₉O⁻ data in the branching ratio plot demonstrates that HO⁻ and C₅H₈O^{•-} react with a second equivalent of 3-pentanone, forming, in each case, additional C₅H₉O⁻. Analysis of the branching ratio plots leads to the yields of the primary products from the reaction of O^{•-} with 3-pentanone being assigned as: 10% HO⁻, 21% CH₃CH₂COO⁻, 44% C₅H₈O^{•-} and 25% C₅H₉O⁻. The qualitative and quantitative observations lead to the reaction processes, summarized in Scheme 2.2.

Interestingly, no *m/z* 55, CH₃CCO⁻, produced by the fragmentation of the 1,1 H₂^{•+}-abstraction product (analogous to the *m/z* 41 formed in acetone) was observed, despite careful searching for it. Nose cone CID experiments (up to 20V) failed to induce fragmentation of C₅H₈O^{•-}, as in the acetone case discussed above.

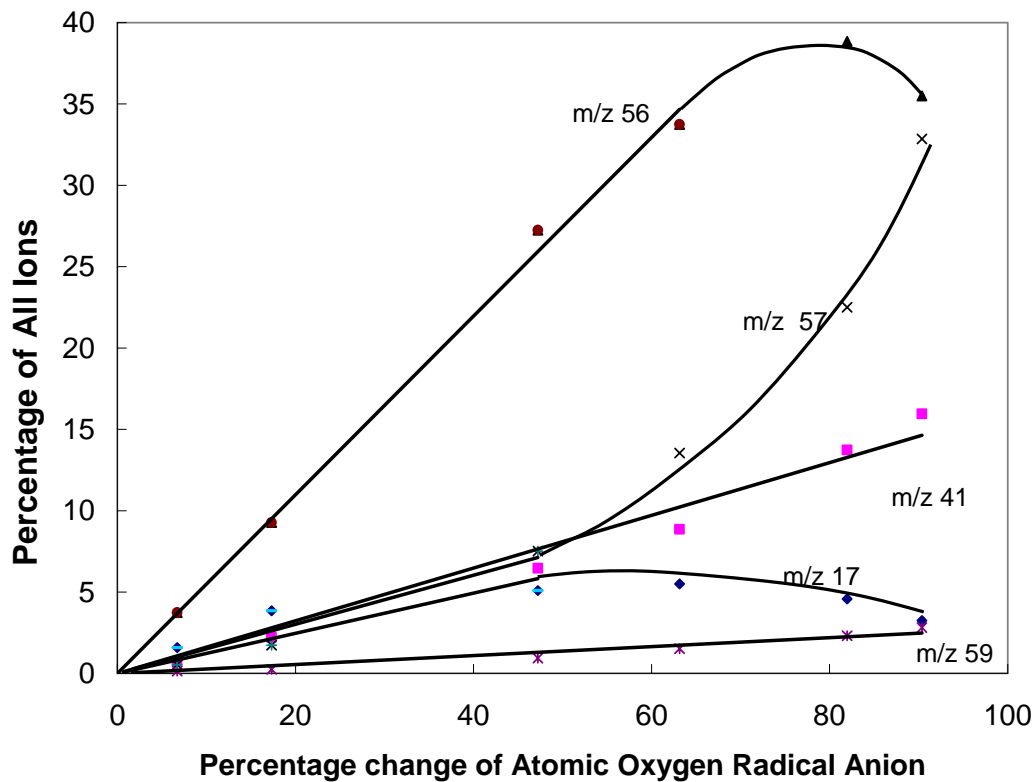
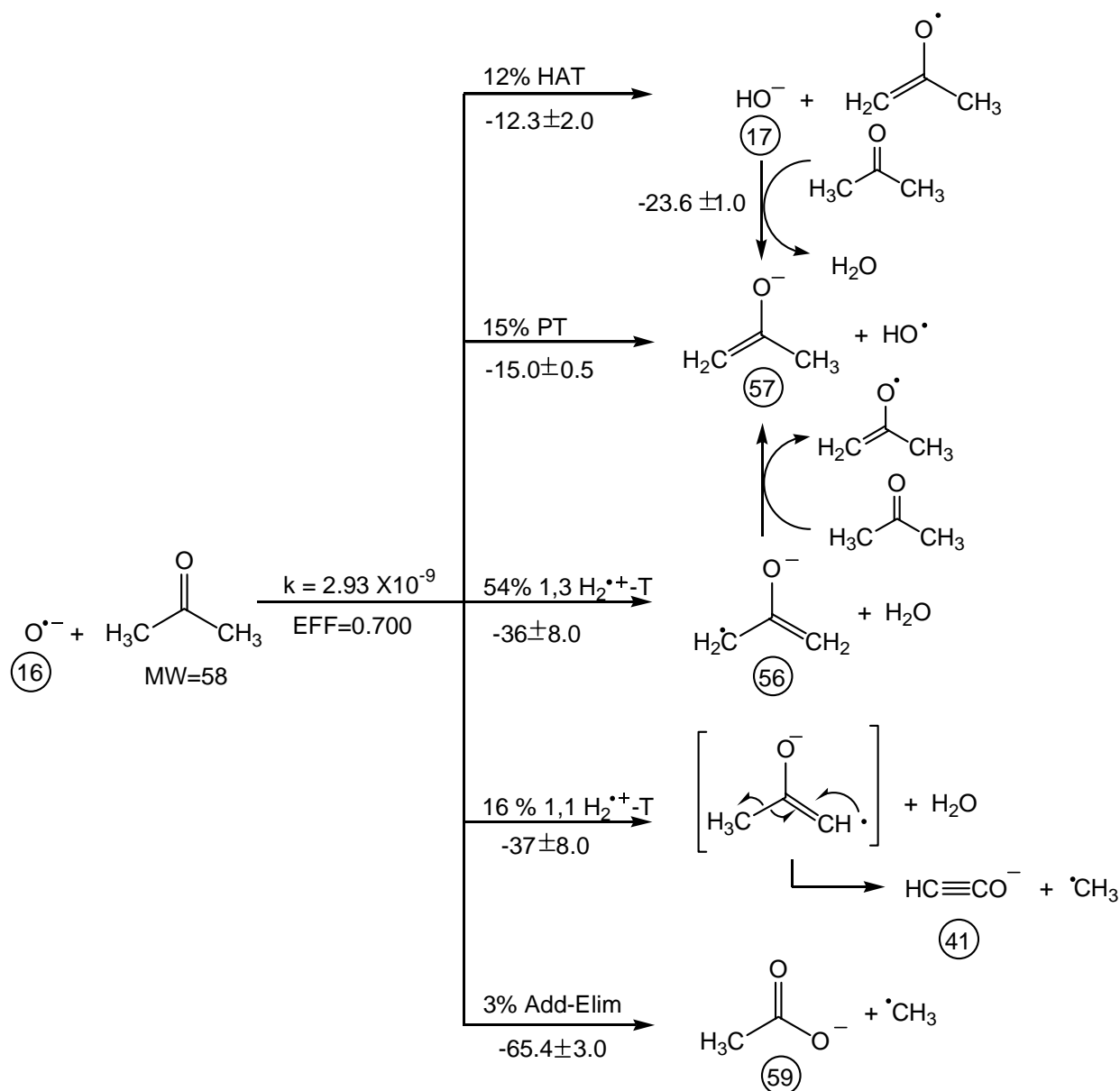


Figure 2.2. Representative branching ratio plot for the reaction of $O^{\bullet-}$ with acetone. The symbols represent experimentally observed data; the solid lines are a smooth fit to the observed data points.



Scheme 2.1. Proposed scheme for the reaction of $\text{O}^{\bullet-}$ with acetone. HAT stands for hydrogen atom transfer, PT for proton transfer, $\text{H}_2^{\bullet+}$ -T for $\text{H}_2^{\bullet+}$ -transfer, and Add-Elim for addition-elimination. The estimated reaction enthalpies (in kcal mol⁻¹) are listed below or to the left of reaction arrow for each pathway. Note: the reaction enthalpy of -37 ± 8.0 kcal mol⁻¹ listed for the 1,1-abstraction channel is the enthalpy change for the formation of the radical anion plus H_2O . The m/z value of each observed product ion is indicated by the number in a circle placed below each ion.

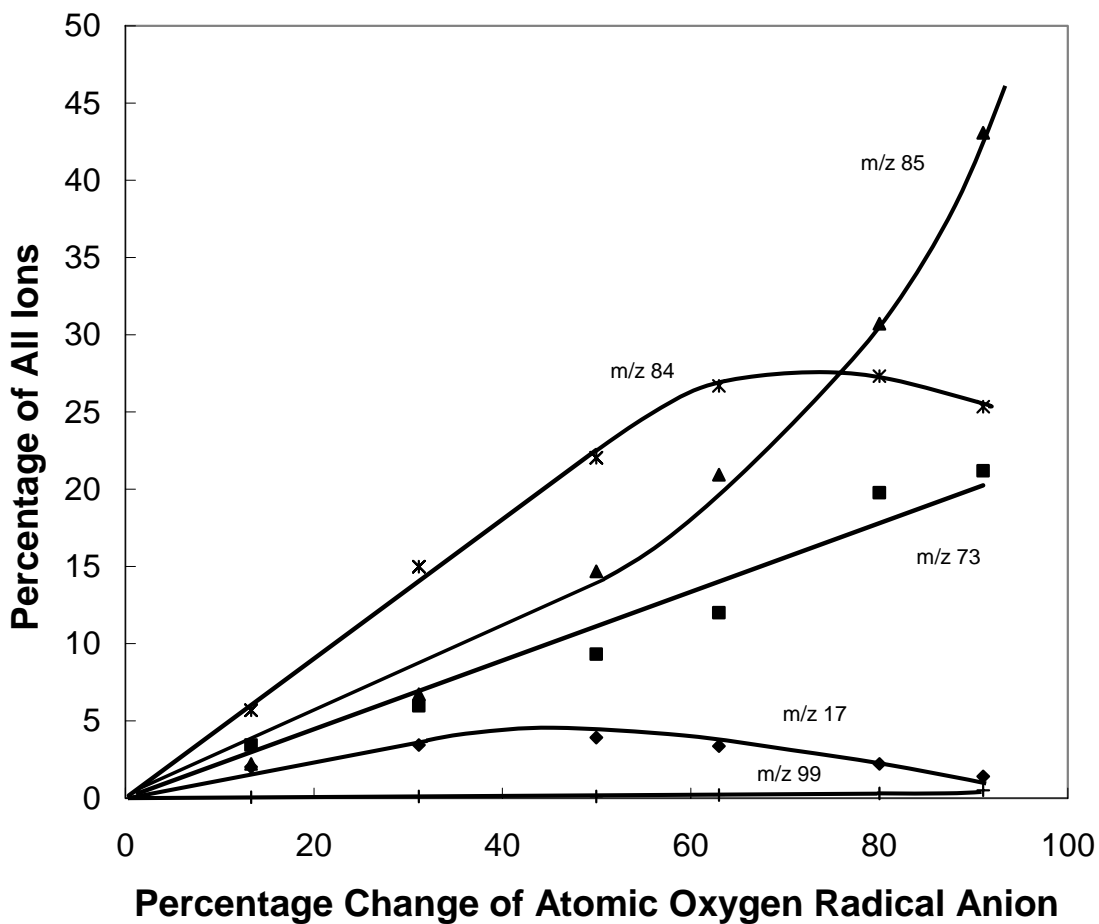
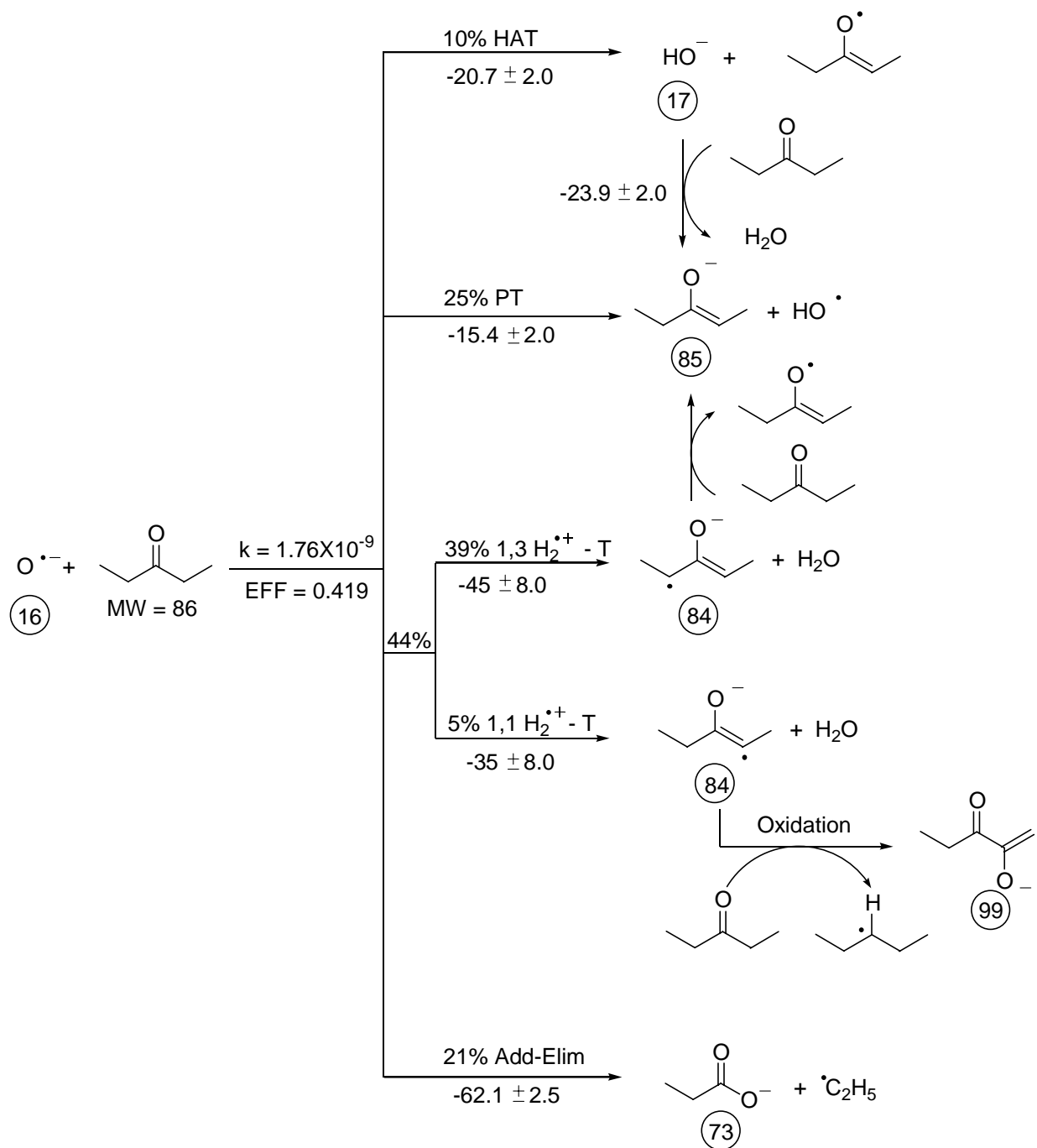


Figure 2.3. Representative branching plot for the reaction of $O^{\bullet-}$ with 3-pentanone. The symbols represent experimentally observed data; the solid lines are a smooth fit to the observed data points.



Scheme 2.2. Proposed scheme the reaction of $\text{O}^{\bullet-}$ with 3-pentanone. HAT stands for hydrogen atom transfer, PT for proton transfer, $\text{H}_2^{\bullet+}\text{-T}$ for $\text{H}_2^{\bullet+}$ -transfer, and Add-Elim for addition-elimination. The estimated reaction enthalpies (in kcal mol^{-1}) are listed below or to the left of reaction arrow for each pathway. The m/z value of each observed product ion is indicated by the number in a circle placed below each ion.

2.3.3. Cyclopentanone

The products observed in the reaction of the atomic oxygen radical anion with cyclopentanone are m/z 17, 82, 83, and 97. When 2,2,5,5- d_4 -cyclopentanone is allowed to react with $O^{\bullet-}$, the products are m/z 18, 84, 86, and 99. One of the replicate branching ratio experiments for cyclopentanone is summarized in Figure 2.4, which demonstrates that m/z 17, 82, and 83 are primary products while m/z 97 is only a secondary product (i.e., m/z 97 is best fit to a curve that has zero slope at zero reaction). Considering the secondary reaction of m/z 97, and the shift to m/z 99 in the d_4 -cyclopentanone experiment leads to the conclusion that it has a molecular formula of $C_5H_5O_2^-$ and which indicates that of the three hydrogens lost from the original cyclopentanone molecule, only two are from carbons immediately adjacent to the carbonyl carbon. We have therefore assigned m/z 97 to deprotonated cyclopenta-1,2-dione. The qualitative and quantitative observations (Figure 2.4) lead to the chemical reactions summarized in Scheme 2.3. Analysis of the branching ratio data according to the Scheme 2.3 leads to the conclusion that the primary product yields are 21% HO^- , 31% $C_5H_9O^-$ and 48% $C_5H_8O^{\bullet-}$. The curvature in the branching ratio plots at long reaction time demonstrates that HO^- reacts with a second equivalent of cyclopentanone via proton transfer yielding additional $C_5H_9O^-$. The $C_5H_8O^{\bullet-}$ also reacts with a second equivalent of cyclopentanone to give both $C_5H_9O^-$ and m/z 97.

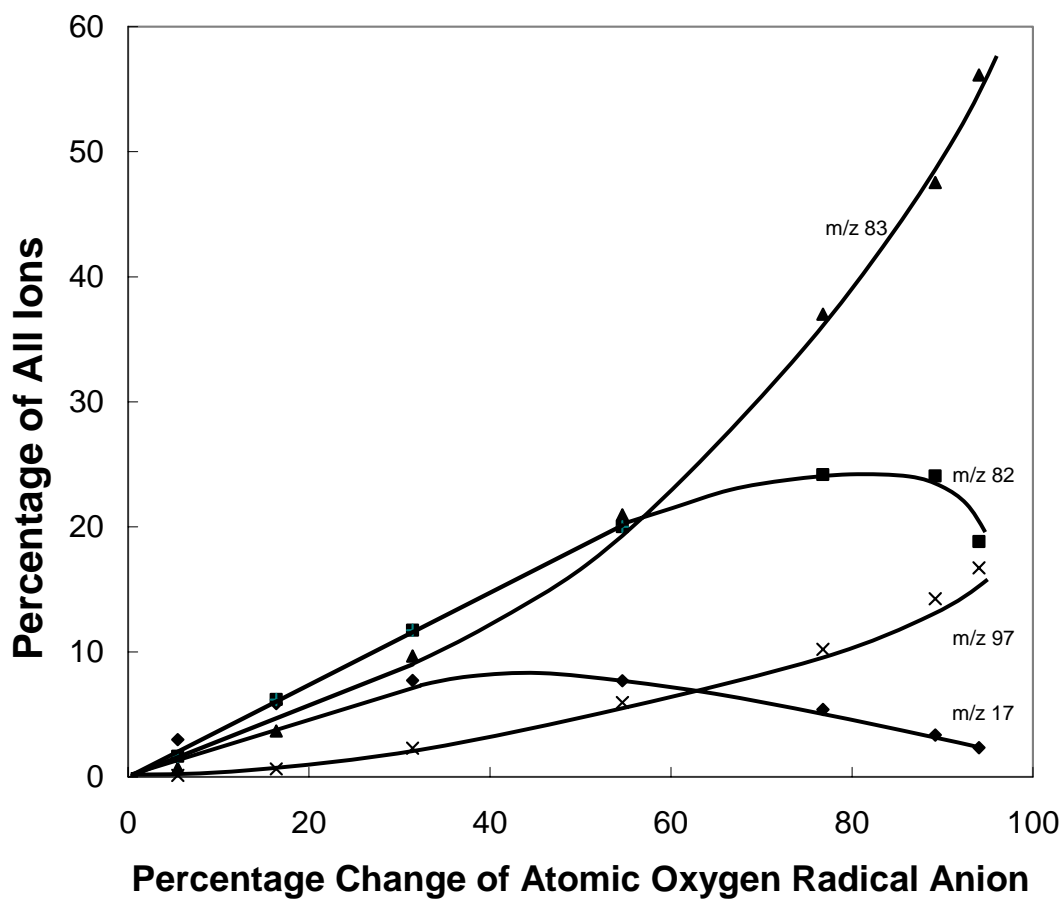
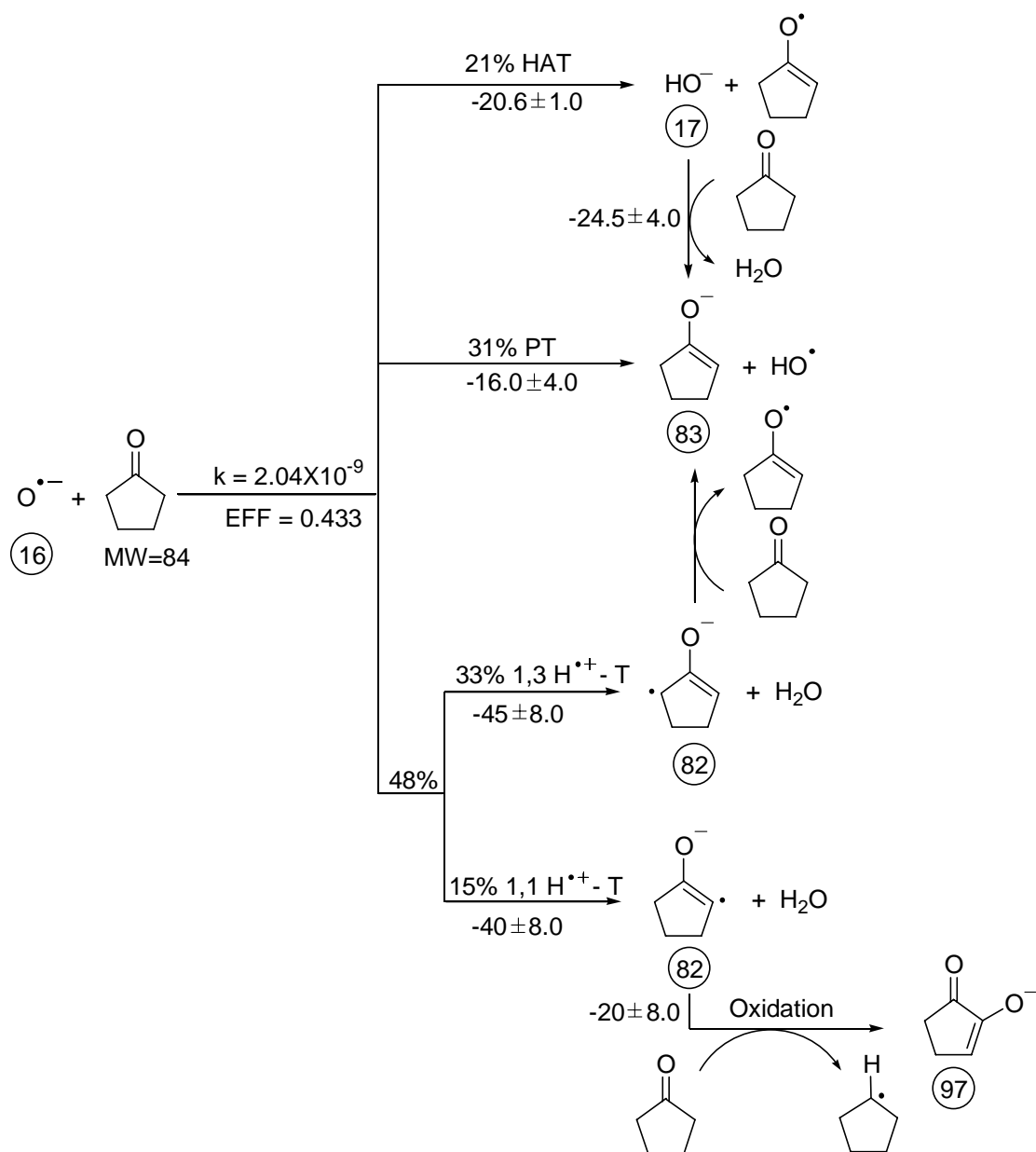


Figure 2.4. Representative branching plot for the reaction of $O^{\bullet-}$ with cyclopentanone. The symbols represent experimentally observed data; the solid lines are a smooth fit to the observed data points.



Scheme 2.3. Proposed scheme for the reaction of $\text{O}^{\bullet-}$ with cyclopentanone. HAT stands for hydrogen atom transfer, PT for proton transfer, and $\text{H}_2^{\bullet+}$ -T for $\text{H}_2^{\bullet+}$ -transfer. The estimated reaction enthalpies (in kcal mol^{-1}) are listed below or to left of the reaction arrow for each pathway. The m/z value of each observed product ion is indicated by the number in a circle placed below each ion.

2.3.4. 2-Butanone

The products observed from the reaction of atomic oxygen radical anion with 2-butanone are m/z 17, 41, 55, 59, 70, 71, 73 and 85 ions. In accord with the experiments described above, these m/z values are assigned to HO^- , HCCO^- , CH_3CCO^- , CH_3COO^- , $\text{C}_4\text{H}_6\text{O}^{\bullet-}$, $\text{C}_4\text{H}_7\text{O}^-$, $\text{CH}_3\text{CH}_2\text{COO}^-$ and $\text{C}_4\text{H}_5\text{O}_2^-$. A representative branching ratio plot is shown in Figure 2.5; among the product ions, it demonstrates that HCCO^- , CH_3CCO^- , CH_3COO^- and $\text{CH}_3\text{CH}_2\text{COO}^-$ are only primary products and do not participate any secondary reaction. A trace amount of $\text{C}_4\text{H}_5\text{O}_2^-$ (m/z 85) is observed and was demonstrated (data not shown) to be only a secondary reaction product ion. The curvature of HO^- , $\text{C}_4\text{H}_6\text{O}^{\bullet-}$ and $\text{C}_4\text{H}_7\text{O}^-$ data indicates that HO^- reacts with a secondary equivalent of 2-butanone via proton transfer yielding $\text{C}_5\text{H}_9\text{O}^-$. $\text{C}_4\text{H}_6\text{O}^{\bullet-}$ reacts with additional 2-butanone forming both an oxidation product $\text{C}_4\text{H}_5\text{O}_2^-$ and $\text{C}_5\text{H}_9\text{O}^-$. Combining all qualitative and quantitative results, the reaction scheme summarized in Scheme 2.4 is proposed. The branching ratio analysis according to this scheme leads to the primary product distribution: 17% HO^- , 4% HCCO^- , 2% CH_3CCO^- , 2% CH_3COO^- , 42% $\text{C}_4\text{H}_6\text{O}^{\bullet-}$, 30% $\text{C}_4\text{H}_7\text{O}^-$, and 3% $\text{CH}_3\text{CH}_2\text{COO}^-$.

2.3.5. Cyclohexanone

The product ions observed from the reaction of atomic oxygen radical anion with cyclohexanone are m/z 17, 96, 97 and 111. Based on comparison with cyclopentanone, the product ions from cyclohexanone reaction are identified to be HO^- , $\text{C}_6\text{H}_8\text{O}^{\bullet-}$, $\text{C}_6\text{H}_9\text{O}^-$, and $\text{C}_6\text{H}_7\text{O}_2^-$. A representative branching ratio plot is shown in Figure 2.6; it illustrates that $\text{C}_6\text{H}_7\text{O}_2^-$ is only a secondary reaction product. The curvature of HO^- , $\text{C}_6\text{H}_8\text{O}^{\bullet-}$ and $\text{C}_6\text{H}_9\text{O}^-$ data at longer reaction time in the branching ratio plot shows that HO^- and $\text{C}_6\text{H}_8\text{O}^{\bullet-}$ each react with a second

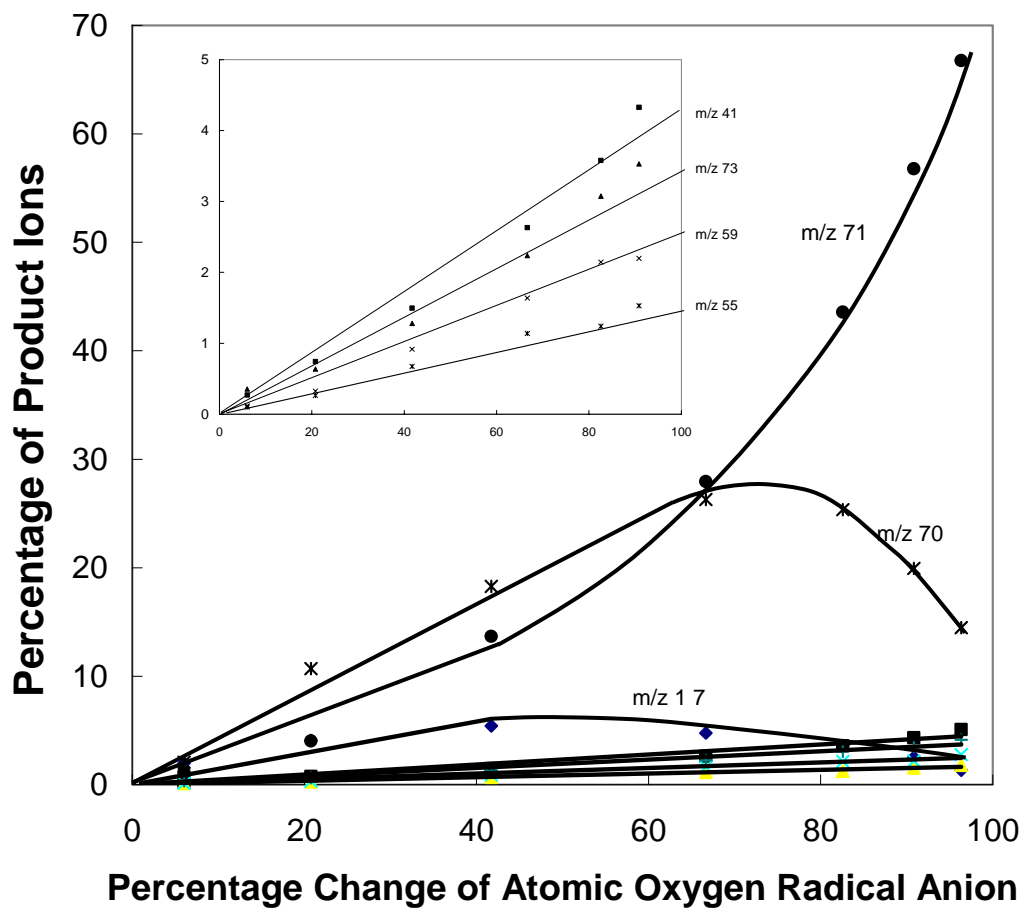
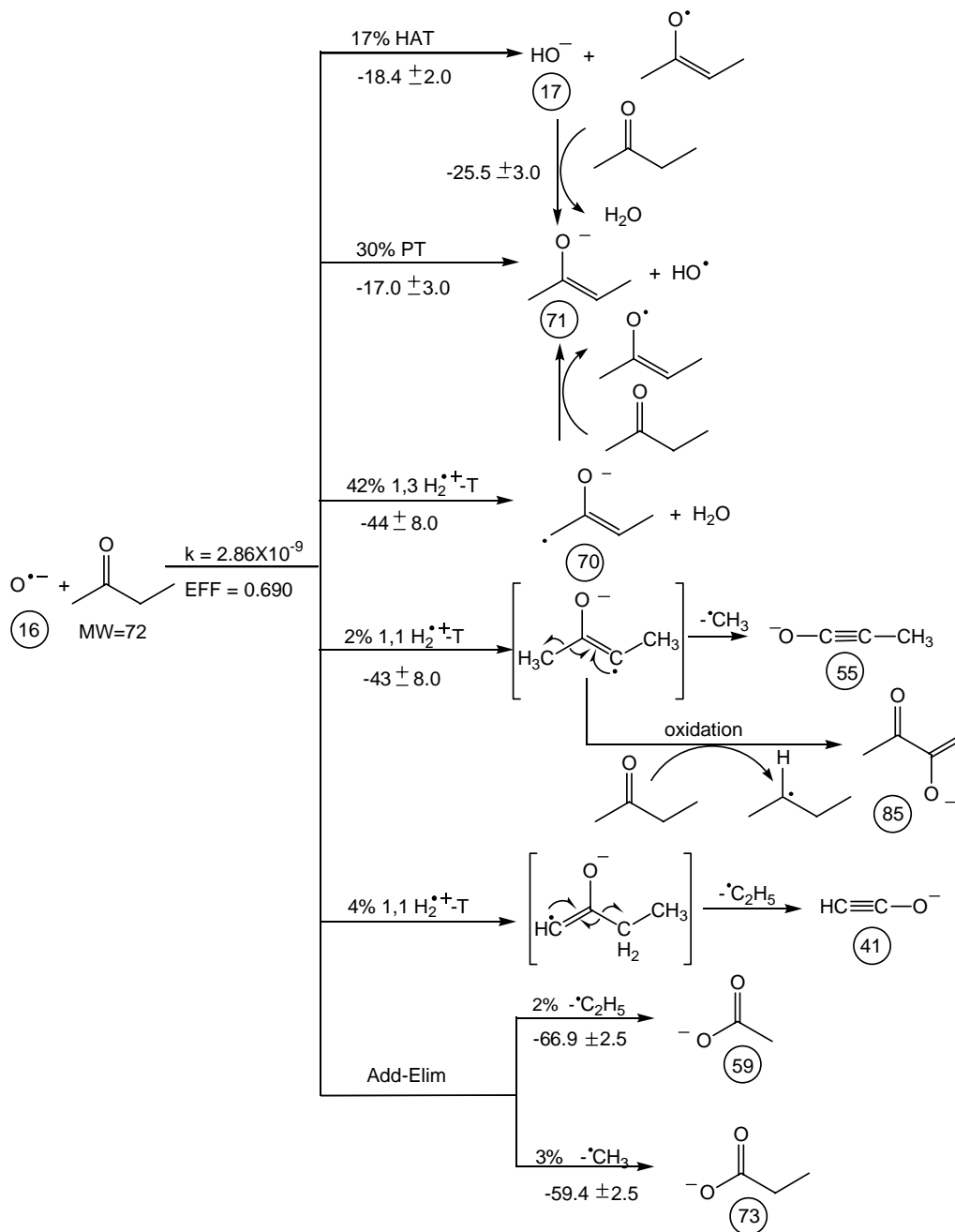


Figure 2.5. Representative branching plot for the reaction of $\text{O}^{\bullet-}$ with 2-butanone. The symbols represent experimentally observed data; the solid lines are a smooth fit to the observed data points. $\text{C}_4\text{H}_5\text{O}_2^-$ (m/z 85) is not shown in the figure to avoid congestions. The insert is an enlargement of the Y-scale and includes only the 4 minor products.



Scheme 2.4 Proposed scheme for the reaction of $\text{O}^{\bullet-}$ with 2-butanone. HAT stands for hydrogen atom transfer, PT for proton transfer, $\text{H}_2^{\bullet+}$ -T for $\text{H}_2^{\bullet+}$ -transfer, and Add-Elim for addition-elimination. The estimated reaction enthalpies (in kcal mol^{-1}) are listed below or to the left of reaction arrow for each pathway. Note: the reaction enthalpy of $-43 \pm 8.0 \text{ kcal mol}^{-1}$ listed for the 1,1-abstraction channel is the enthalpy change for the formation of the radical anion plus H_2O . The m/z value of each observed product ion is indicated by the number in a circle placed below each ion.

equivalent of cyclohexanone, individually, to form $C_6H_9O^-$ (m/z 97). The radical anion, $C_6H_8O^\bullet$, also reacts with an additional cyclohexanone producing $C_6H_9O^-$ via oxidation. By considering both the qualitative (data not shown) and the quantitative results, the reaction processes for $O^{\bullet-}$ with cyclohexanone summarized in Scheme 2.5 are proposed. The primary product distribution obtained through a branching ratio analysis according to this scheme is: 18% HO^- , 47% $C_6H_8O^\bullet$, and 35% $C_6H_9O^-$.

2.3.6. 2,4-Dimethyl-3-pentanone

The product ions observed from the reaction of atomic oxygen radical anion with 2,4-dimethyl-3-pentanone are m/z 17, 87, 112, and 113, which correspond to HO^- , $(CH_3)_2CH_2COO^-$, $C_7H_{12}O^{\bullet-}$, and $C_7H_{13}O^-$ in accord with the reactions discussed above. A representative branching ratio plot is shown in Figure 2.7; it demonstrates that $(CH_3)_2CH_2COO^-$ is only a primary reaction product (straight line in Figure 2.7). The curvature of HO^- , $C_7H_{12}O^{\bullet-}$, and $C_7H_{13}O^-$ shows that HO^- and $C_7H_{12}O^{\bullet-}$ react with, in each case, a second equivalent of 2,4-dimethyl-3-pentanone producing $C_7H_{13}O^-$. Combining these qualitative and quantitative results, the reaction scheme for $O^{\bullet-}$ and 2,4-dimethyl-3-pentanone reaction summarized in Scheme 2.6 is proposed. The branching ratio analysis according to this scheme leads to the primary product distributions: 17% HO^- , 65% $(CH_3)_2CH_2COO^-$, 3% $C_7H_{12}O^{\bullet-}$, and 15% $C_7H_{13}O^-$.

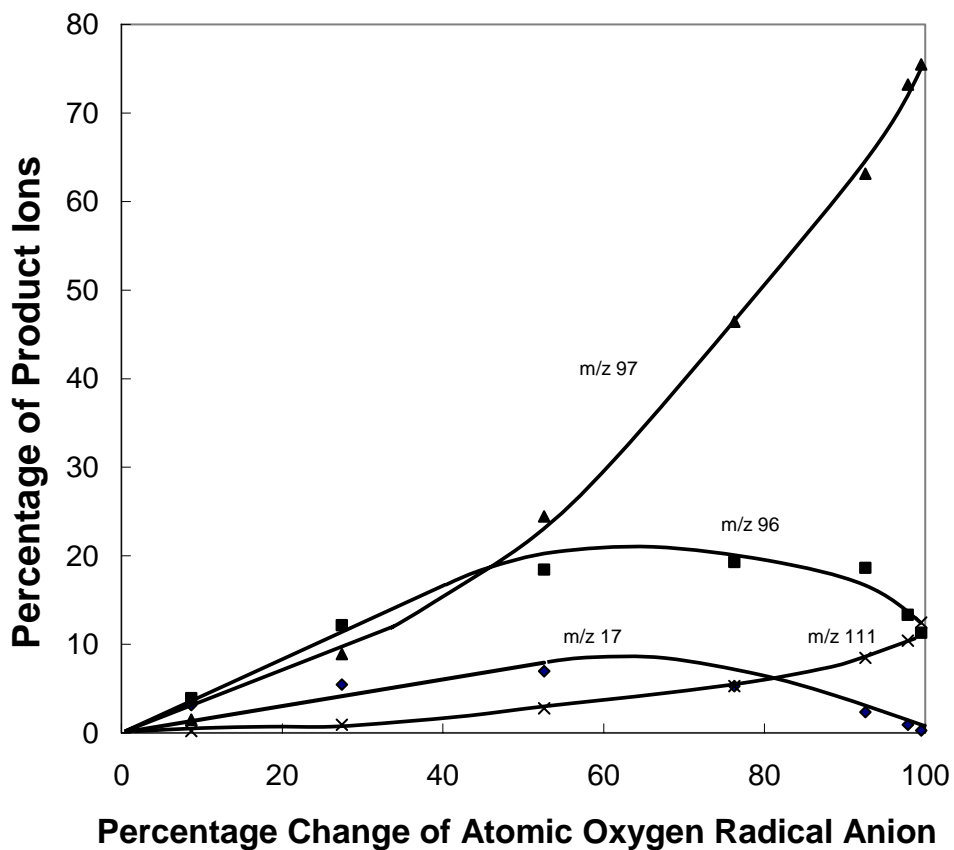
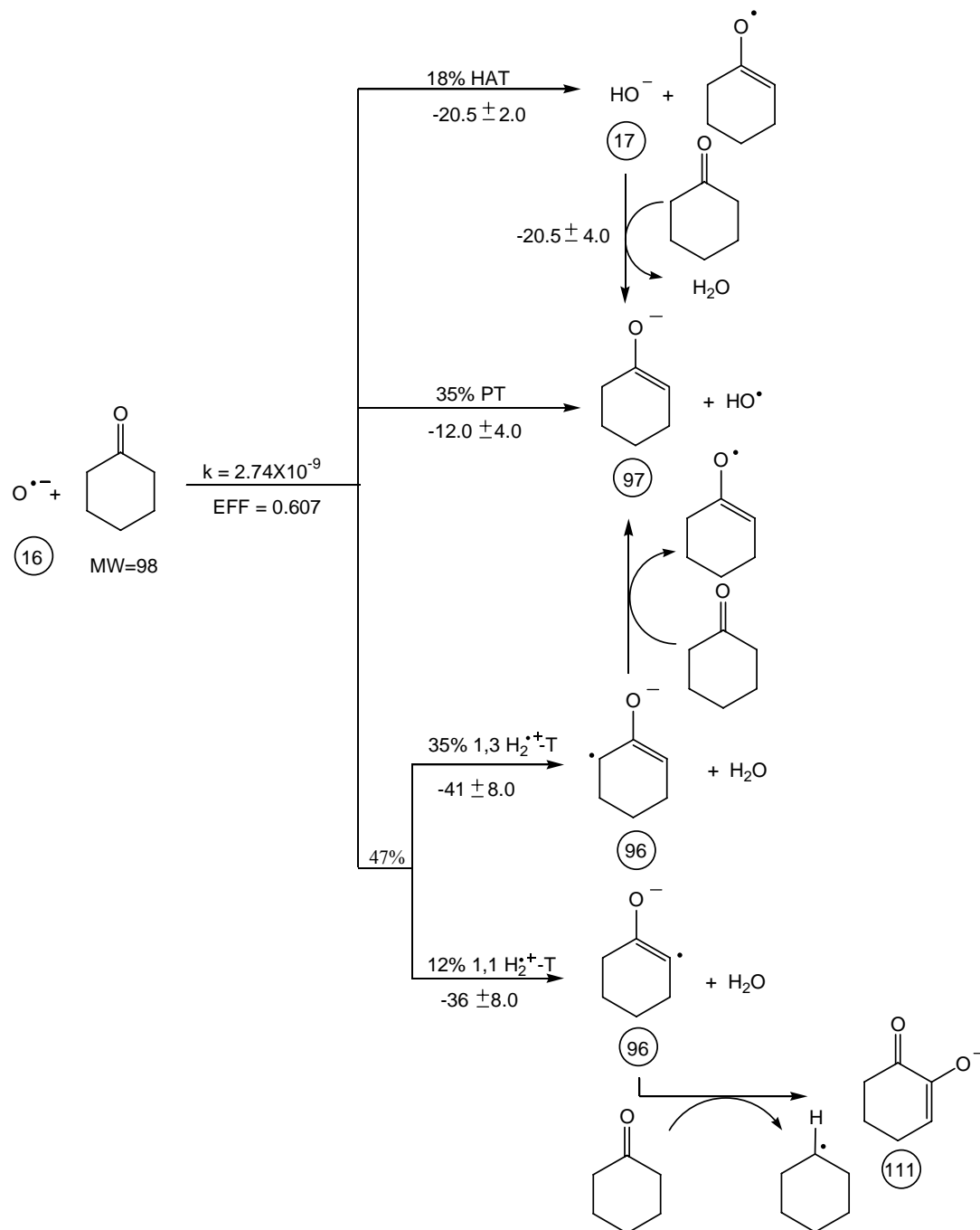


Figure 2.6. Representative branching plot for the reaction of $O^{\bullet-}$ with cyclohexanone. The symbols represent experimentally observed data; the solid lines are a smooth fit to the observed data points.



Scheme 2.5. Proposed scheme for the reaction of $\text{O}^{\bullet-}$ with cyclohexanone. HAT stands for hydrogen atom transfer, PT for proton transfer, and $\text{H}_2^{\bullet+}$ -T for $\text{H}_2^{\bullet+}$ -transfer. The estimated reaction enthalpies (in kcal mol⁻¹) are listed below or to the left of reaction arrow for each pathway. The *m/z* value of each observed product ion is indicated by the number in a circle placed below each ion.

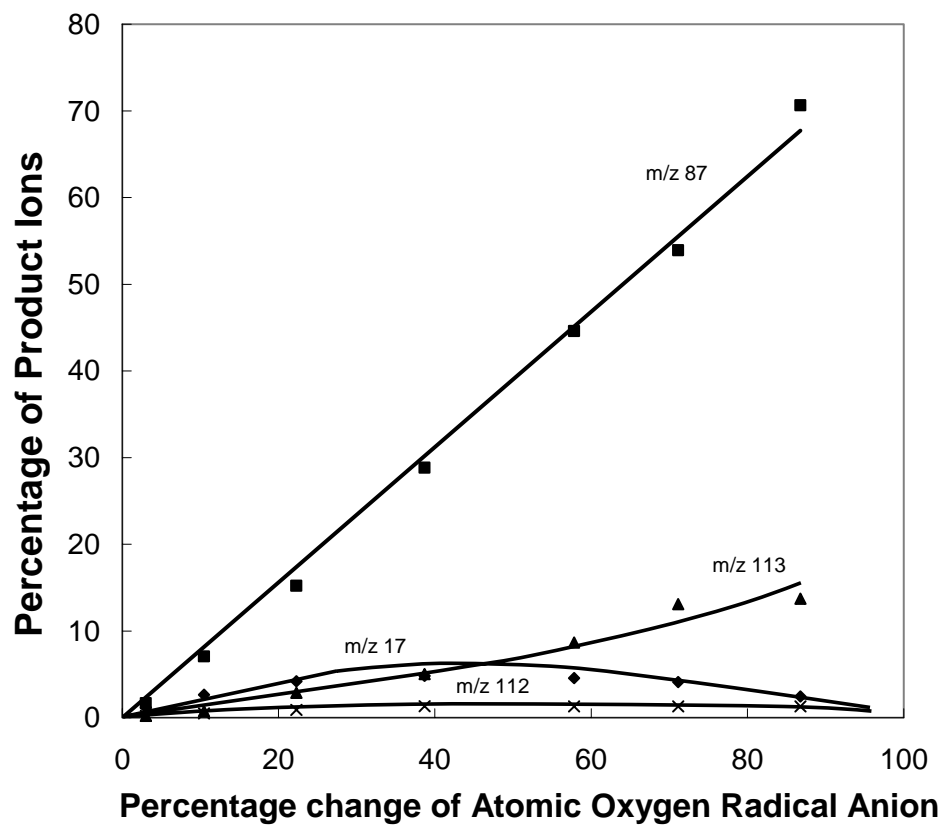
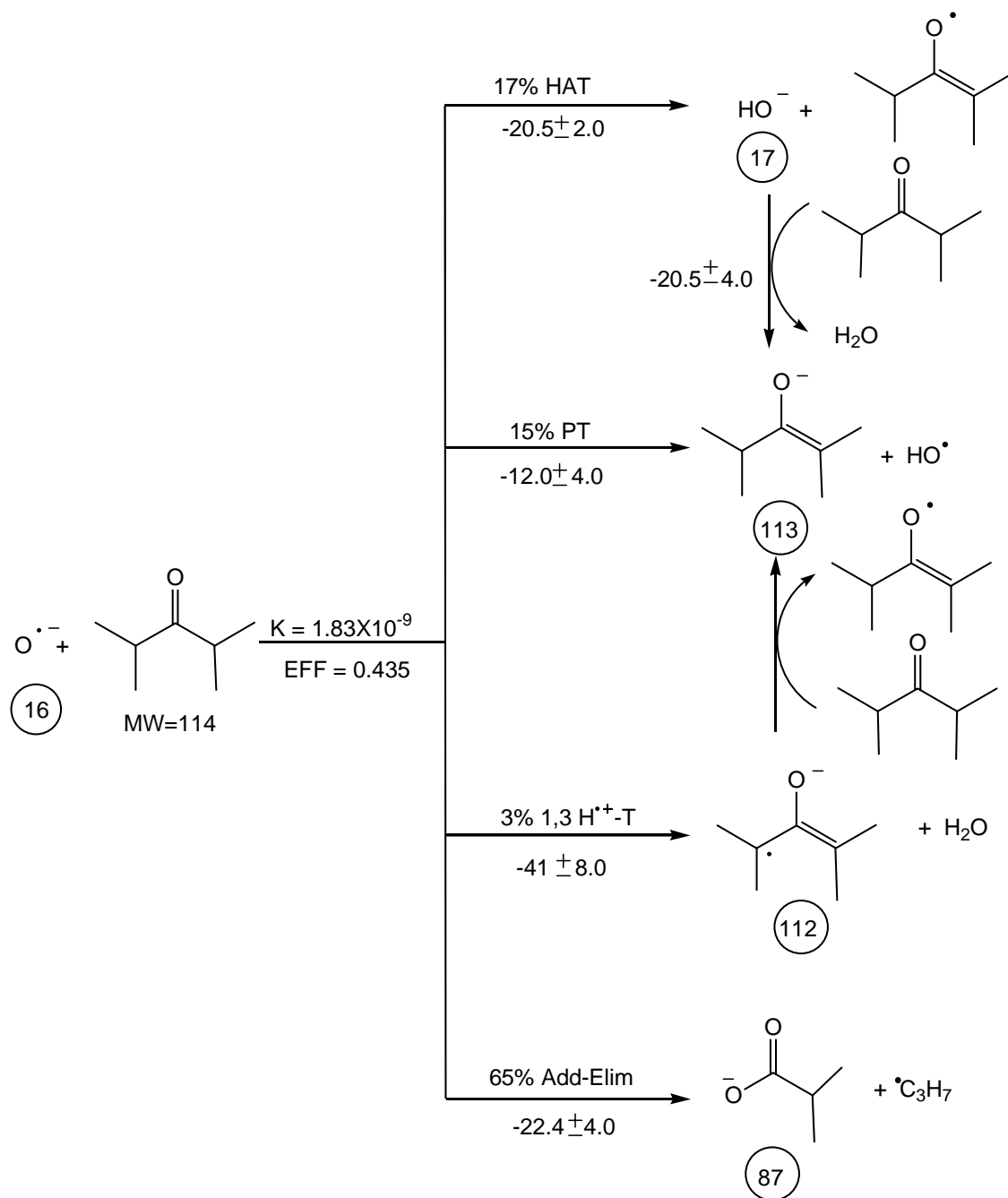


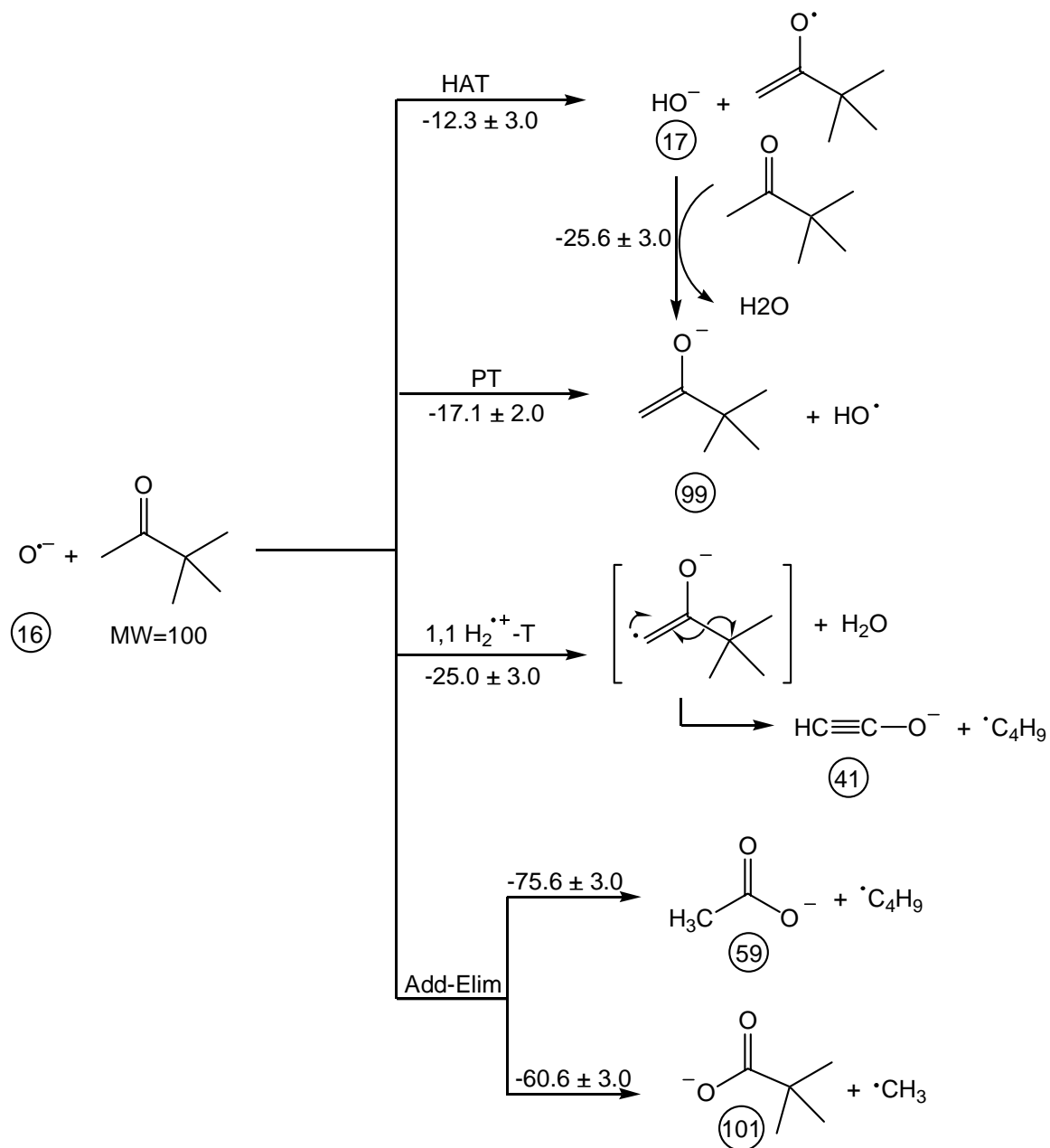
Figure 2.7. Representative branching plot for the reaction of $O^{\bullet-}$ with 2,4-dimethyl-3-pentanone. The symbols represent experimentally observed data; the solid lines are a smooth fit to the observed data points.



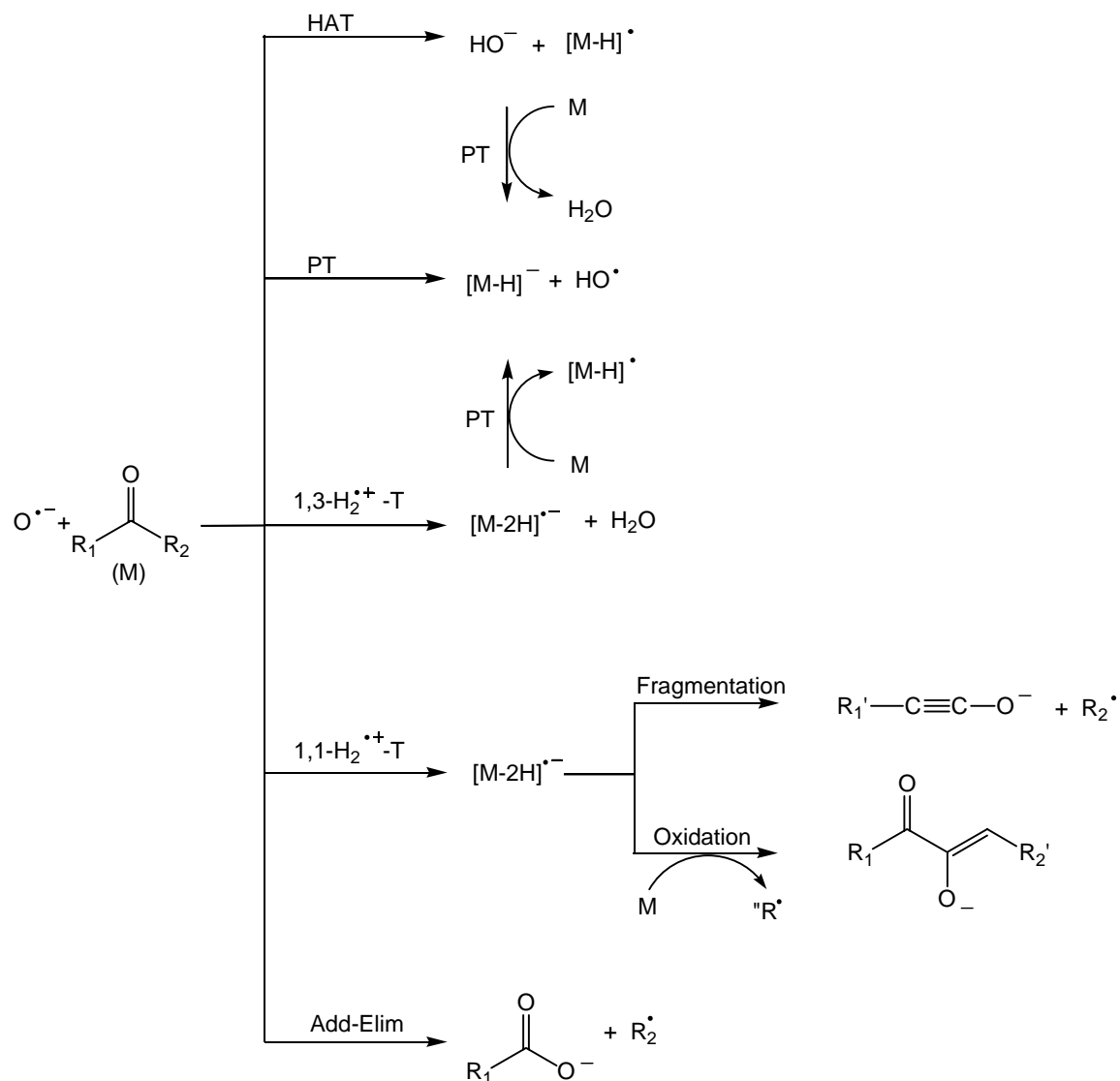
Scheme 2.6. Proposed scheme for the reaction of $\text{O}^{\bullet-}$ with 2,4-dimethyl-3-pentanone. HAT stands for hydrogen atom transfer, PT for proton transfer, $\text{H}_2^{\bullet+}$ -T for $\text{H}_2^{\bullet+}$ -transfer, and Add-Elim for addition-elimination. The estimated reaction enthalpies (in kcal mol⁻¹) are listed below or to the left of reaction arrow for each pathway. The *m/z* value of each observed product ion is indicated by the number in a circle placed below each ion.

2.3.7. 3,3-Dimethyl-2-butanone

The product ions observed from the reaction of atomic oxygen radical anion with 3,3-dimethyl-2-butanone are m/z 17, 41, 59, 99 and 101, and which have been assigned as HO^- , HCCO^- , $\text{CH}_3\text{CH}_2\text{COO}^-$, $(\text{CH}_3)_3\text{CC}(\text{O}^-)=\text{CH}_2$, and $(\text{CH}_3)_3\text{COO}^-$, the major product of which is from proton transfer. Based on these qualitative observations and the similar reactions discussed above (note, no branching ratio experiments were conducted on this compound), the reaction scheme summarized in Scheme 2.7 is proposed. Examination of the spectra recorded reveals that the major product is $(\text{CH}_3)_3\text{CC}(\text{O}^-)=\text{CH}_2$ (m/z 99). No m/z 98, which would correspond to $[\text{M}-2\text{H}]^{\bullet-}$, is detected. The m/z 41, with a yield of $\sim 15\%$, is assigned as a fragmentation product from an initially formed, but not stable, $[\text{M}-2\text{H}]^{\bullet-}$.



Scheme 2.7. Proposed scheme for the reaction of $\text{O}^{\bullet-}$ with 3,3-dimethyl-2-butanone. HAT stands for hydrogen atom transfer, PT for proton transfer, $\text{H}_2^{\bullet+}$ -T for $\text{H}_2^{\bullet+}$ -transfer, and Add-Elim for addition-elimination. The m/z value of each observed product ion is indicated by the number in a circle placed below each ion.



Scheme 2.8. Proposed scheme for the reaction of $\text{O}^{\bullet-}$ with a generic ketone, M. HAT stands for hydrogen atom transfer, PT for proton transfer, $\text{H}_2^{\bullet+}\text{-T}$ for $\text{H}_2^{\bullet+}$ -transfer, and Add-Elim for addition-elimination. For the ketones examined, the yield of HAT is $\sim 16\%$; the yield of PT is $\sim 7.3\%$ per $\alpha\text{-H}$ except for the least acidic acetone (2.5%); the yield of $[\text{M-2H}]^{\bullet-}$ is $\sim 47\%$ except for 2,4-dimethyl-3-pentanone; and the yield of Add-Elim increases as the size of R_1/R_2 increases but is not observed for cyclic ketones.

2.4. Discussion

The five main pathways for the reaction of the atomic oxygen radical anion with a ketone are: hydrogen atom transfer producing HO^- ; proton transfer producing the conjugate base of the ketone, $[\text{M}-1]^-$; H_2^{*+} -abstraction producing a didehydro radical anion, $[\text{M}-2]^{*-}$ from either 1,1 or 1,3 abstraction; and an addition-elimination reaction producing a carboxylate anion. All five typical reaction channels, when structurally possible, are observed in the ketone reactions examined in this work. These common reaction pathways are summarized in Scheme 2.8, which also includes the often observed secondary reactions; unique reaction channels are also observed in individual ketone reaction.

2.4.1. Reaction rates and proton transfer

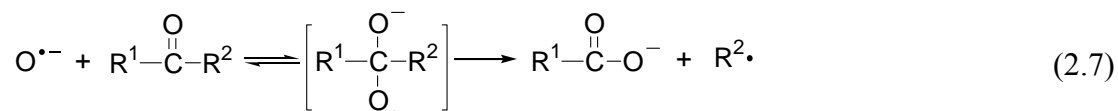
As is common for atomic oxygen radical anions with organics, all the rate coefficients reported herein are for highly efficient reactions, indicating that O^{*-} reacts with ketones on 4 out of 10 collisions or better. Inspection of either the rate coefficients or the reaction efficiencies indicates that on a per alpha C-H bond basis, the reaction proceeds more rapidly as acidity is increased. For example, the least acidic ketone has an efficiency of 10-12% per alpha C-H while the most acidic is double that at 22%. However, the yield of observed proton transfer product, per alpha C-H, is essentially invariant at 7.3% except for acetone the least acidic ketone examined for which it is only 2.5%. All ketones examined are more acidic (Table 2.1) than either HO^* ($\Delta H^\circ_{\text{acid}} = 382.7 \pm 0.10 \text{ kcal mol}^{-1}$) [38] or H_2O ($\Delta H^\circ_{\text{acid}} = 390.3 \text{ kcal mol}^{-1}$) [38] and yet, the observed products are more than just simple proton transfer, reflecting, the high proton affinities of HO^- and the fact that it is created adjacent to additional acidic protons on the newly formed organic radical.

2.4.2. HAT

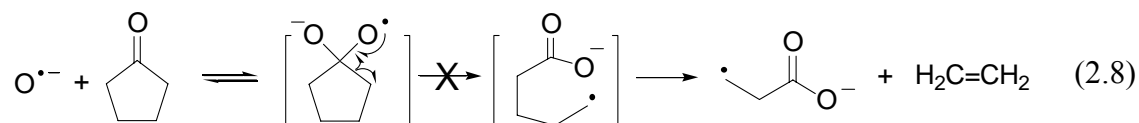
The hydrogen transfer (HAT) channel is always observed for the $O^{\bullet-}$ chemical ionization of ketones, but is never the major product. This is undoubtedly due to the high hydrogen atom affinities of hydroxyl radical (BDE [HO-H] = 119 ± 1 kcal mol⁻¹) [34], and the ready availability of additional, relatively labile C-H bonds. The hydroxide formed from a HAT process always reacts efficiently with a second equivalent of the ketone, by a proton abstraction process, in accord with literature. For example, HO^- with acetone produces only acetone enolate, with a reaction efficiency of 90% ($k_{\text{obs}} = 3.7 (\pm 0.9) \times 10^{-9}$ molecule⁻¹ cm³ s⁻¹ [39]).

2.4.3. Addition-elimination

The addition-elimination channel (eq. 2.7) is observed for each acyclic ketone, but



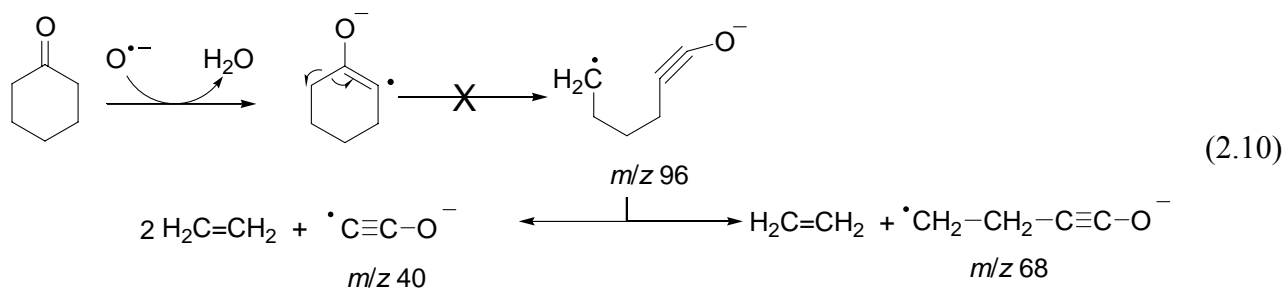
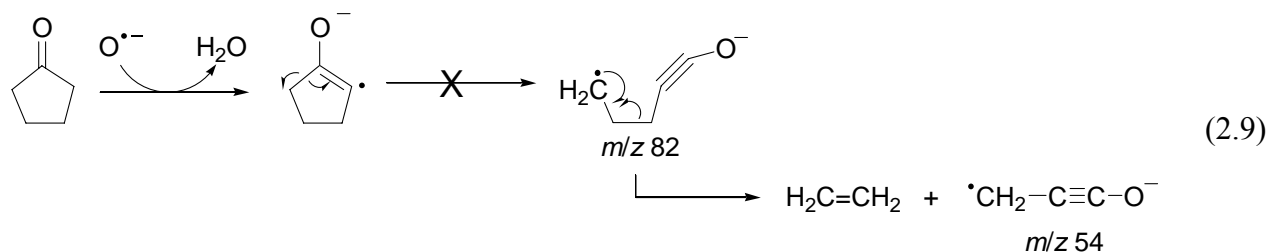
in widely varying absolute yields. However, if you consider the size of R^1 and R^2 , as the sum of these sizes increase, the yields of the addition-elimination channel increases. Thus acetone (two methyl groups) has the lowest yield of the addition-eliminations followed by methyl ethyl ketone, then diethyl ketone and lastly by 2,4-dimethyl-3-pentanone. Of course, the bulkier ketones also have “better” radical leaving groups from the tetrahedral intermediate on the addition-elimination pathway, suggesting that the first step in eq. 2.7 is reversible. Van der Wel et al. reported the observation of ¹⁸O-incorporated addition-elimination products from the reactions of ¹⁸O^{•-} with several carbonyl-containing compounds [40]. Interestingly enough, neither cyclic ketone examined here displayed products from an addition-elimination pathway (e.g., eq. 2.8).



2.4.4. 1,1-H₂^{•+} abstraction

Products corresponding to the fragmentation from a 1,1-H₂^{•+} abstraction process are observed in the acetone, 2-butanone and 3,3-dimethyl-2-butanone reactions, but are not observed in the 3-pentanone, cyclopentanone or cyclohexanone reactions. 1,1-H₂^{•+} abstraction is not structurally possible for 2,4-dimethyl-3-pentanone. For example, in the acetone reaction (Scheme 2.1), HCCO⁻ is assigned as the fragment from a 1,1-H₂^{•+} abstraction process. Dawson and co-workers reported the observation of both HCCO⁻ and DCCO⁻ in the reaction of O^{•-} with 1,1,1-*d*₃-acetone [24]. Our results from the CID experiments on the [M-2H]⁻ product from the acetone reaction suggests that any 1,1-H₂^{•+} abstraction product fragments immediately to HCCO⁻ (i.e., the observed ratio of C₃H₄O^{•+} to HCCO⁻ was invariant with extraction potential). In the 3,3-dimethyl-2-butanone reaction, HCCO⁻ is observed but [M-2H]⁻ is not present. This also suggests that product ions from 1,1-H₂^{•+} abstraction from a methyl group in methyl ketones do not survive long enough to be observed; they fragment by alkyl radical loss instead. Two fragments, CH₃CCO⁻ and HCCO⁻ are observed in the 2-butanone reaction (albeit, in low yields) owing to its asymmetric molecular structure (Scheme 2.4) with the loss of ethyl radical channel favored 2:1 over the methyl radical channel. Of the four acyclic ketones examined, only 3-pentanone does not show a 1,1-H₂^{•+}-fragmentation product. Attempts to induce fragmentation of the abundant [M-2H]⁻ formed in the 3-pentanone reaction, by increasing the nose cone potential, had no effect.

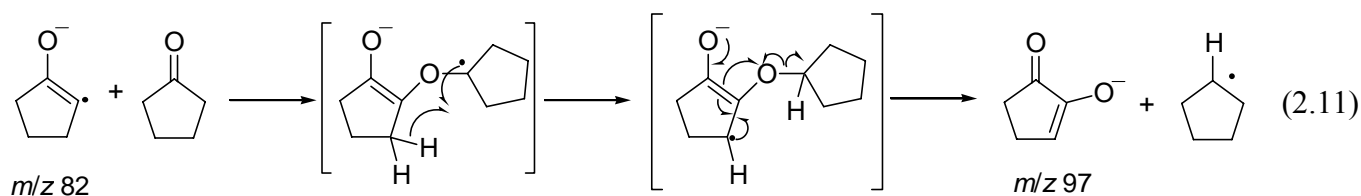
For cyclic ketones, if this 1,1-H₂^{•+} abstraction followed by a fragmentation process occurs, a linear distonic radical anion with a chemical formula [M-2H]^{•-} will be produced (eqs. 2.9 and 2.10) and/or possibly a fragmentation ion from ethylene loss. While [M-2H]^{•-} ions are observed from the cyclic ketones, the fragments are not. Harrison and Jennings reported a *m/z* 54 ion, H₂C=C=C=O^{•-}, was observed from the reaction of in O^{•-} with cyclopentanone in an ICR instrument [23]. However, despite careful checking, we were unable to observe such a product ion. One might argue that the EA of H₂C=C=C=O is too low to allow it to have a long-enough lifetime to be observed in the high pressure flow tube and the lack of observation of *m/z* 54 is due to collisionally-induced detachment. While we cannot conclusively rule out that pathway, a similar explanation for the cyclohexanone reaction is less satisfactory, yet the corresponding ion is not observed for that reaction either. The flowing afterglow we used examines ion-molecule reactions under conditions where the ions have thermal translational energies, while ICR experiments are carried out under high vacuum and prone to have translationally “hot” reactant ions for lack of collisional cooling as has been reported by Matimba et al [29]. There are numerous examples in the ion-molecule literature where excess kinetic energy allows different product ions and/or yields to be observed at different reactant energies. For example, ion-molecule reactions carried out in a SIFT-Drift instrument yield different products when varying reactant kinetic energy [41, 42]. As we will discuss below, we believe that 1,1-H₂^{•+} abstraction products are formed from the cyclic ketone, but that they are stable against the fragmentation process observed for the acyclic methyl ketones.



The formation of the low yield secondary product ion m/z 97 (<15%) in cyclopentanone reaction does not fit into any known $O^{\bullet-}$ reaction scheme. Experiments with d_4 -cyclopentanone prove its molecular formula to be $[M+O-3H]^-$, wherein two of the hydrogens lost originate from an α carbon and the third hydrogen comes from a β carbon. This conclusion is further supported by the observation of trace amounts of $[M+O-3H]^-$ ions in 3-pentanone, 2-butanone and cyclohexanone reactions, but not in acetone, 2,4-dimethyl-3-pentanone or 3,3-dimethyl-2-butanone.

The source molecules that might provide the new oxygen atom for the secondary product ion $[M+O-3H]^-$ in our experiments are limited to N_2O , adventitious O_2 or the parent ketone. If N_2O is the source of the oxygen atom for this secondary reaction, the apparent rate of this reaction will be different on different experimental days because the amount of N_2O present in the flow tube varies from experiment to experiment. In addition, if N_2O is the source, the branching ratio plot would not indicate it is a secondary product. The branching ratio plots

unequivocally demonstrated that all $[M+O-3H]^-$ ions are secondary and are formed in a reproducible manner. Likewise, adventitious O_2 in the helium is ruled out by the curved branching ratio plots. Adventitious O_2 in the ketone sample introduction is ruled out by two observations; the first (section 2.4.6) is that the $1,1-H_2^{++}$ abstraction product from cyclopentanone readily charge transfers to O_2 , thereby serving as a “marker” for adventitious O_2 . The second is that our best efforts to eliminate any adventitious O_2 in the cyclopentanone sample results in spectra lacking an O_2^- signal, but having a m/z 97 signal. Based on these analyses, we propose an “oxidation” pathway for the conversion of initially formed $[M-2H]^-$ to $[M+O-3H]^-$, illustrated in eq. 2.11 using the cyclopentanone reaction as an example.



Incidentally, if the $1,1-H_2^{++}$ abstraction product from cyclopentanone (m/z 82) was a ring-opened form (e.g. Figure 2.8a), we would expect the analogous ion formed from the d_4 -cyclopentanone to be oxidized to the m/z 98 ion shown in Figure 8b, rather than the m/z 99 observed. This data therefore supports our earlier conclusion that the $1,1-H_2^{++}$ ions formed from the cyclic ketone are not ring-opened.

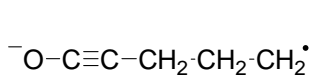


Figure 2.8a

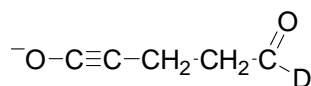


Figure 2.8b

Figure 2.8 Structures of (a) ring-opened form of $1,1-H_2^{++}$ abstraction product from cyclopentanone and (b) oxidation product of ring-opened form of $1,1-D_2^{++}$ abstraction from 2,2,5,5- d_4 -cyclopentanone.

2.4.5. 1,3-H₂^{•+} abstraction

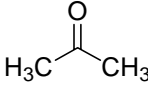
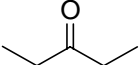
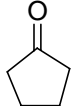
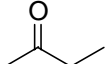
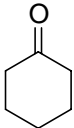
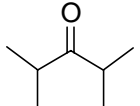
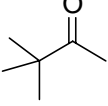
Of the six ketones examined in detail, the H₂^{•+} abstraction channel is the major process (47 ± 5%) in all but 2,4-dimethyl-3-pentanone. In all ketones, at least a portion of the [M-2H]^{•-} signal reacts with a second equivalent of the ketone by a proton transfer reaction. We have assumed that these are reactions of the 1,3-H₂^{•+} abstraction product, but cannot unequivocally rule out participation of the 1,1-H₂^{•+} abstraction products. These facile proton transfer reactions indicate that the alpha-dehydro ketone radicals are less acidic on the other alpha carbon, than the ketone. In other terms, replacing a C-H bond alpha to a carbonyl group with a single electron decreases the acidity of the proton on the opposite alpha carbon.

We have suggested that radical anions formed by 1,1-H₂^{•+} abstraction from methyl ketones, (including acetone, 2-butanone, and 2,2-dimethyl-3-butanone), fragment completely by a β-scission process. It follows therefore that the observed [M-2]^{•-} radical anions from these reactions are only distonic radical anions from 1,3-H₂^{•+} abstraction. For the cyclopentanone reaction, we suggest that the 1,1-H₂^{•+} abstraction product ions does not undergo a fragmentation process (to form a ring-opened distonic radical anion) and that the ring-closed radical anion formed by a 1,1-H₂^{•+} abstraction process reacts rapidly with a second equivalent of cyclopentanone via the oxidation channel. However, adding additional cyclopentanone is insufficient to quench the [M-2H]^{•-} signal. We therefore conclude that for cyclopentanone, of the 48% [M-2H]^{•-} yield, 15% (estimated from the ultimate yield of the oxidation product) is from 1,1- and 33% is from 1,3-H₂^{•+} abstraction. Formally, these are lower and upper limits respectively, but the kinetic behavior demonstrated in the branching ratio plot strongly suggests the absolute yields are not much different from these limits. Cyclohexanone, not unexpectedly, is similar to cyclopentanone: ≥ 12% yield of the 1,1- and ≤ 35% yield of the 1,3-H₂^{•+} abstraction

products. For 2-butanone, small yields of both possible fragment ions from 1,1-H₂^{•+} abstraction products are observed, along with a trace amount of the oxidation product. We conclude that the [M-2H]⁻ from 2-butanone is $\geq 7\%$ from 1,1- and $\leq 41\%$ from 1,3-H₂^{•+} abstraction. For 3-pentanone, we suggest that the [M-2H]⁻ product formed is $\geq 5\%$ from 1,1- and $\leq 39\%$ from 1,3-H₂^{•+} abstraction. Our best estimates of initial yields of the isomeric radical anions from the different ketone are summarized in Table 2.4.

The mechanism of H₂^{•+} abstraction, be it stepwise or concerted is an intriguing question. The fact that all the ketone reactions quantitatively examined in this study show formation of distinct products from just proton transfer, or just hydrogen atom transfer, or both proton and hydrogen atom transfer, suggests that a stepwise mechanism, proceeding by either step first, is highly likely.

Table 2.4. Yields of radical anion from the reaction of $O^{\bullet-}$ with ketones

Reactant Neutral	Total yield of $[M-2H]^{\bullet-}$ ^b	1,1- $H_2^{\bullet+}$ -abstraction ^a	1,3- $H_2^{\bullet+}$ -abstraction ^a
	70%	16%	54%
	44%	5%	39%
	48%	15%	33%
	48%	7%	41%
	47%	12%	35%
	3%	0%	3%
	15%	15%	0%

- a. While these yields are formally limits (lower for 1,1- $H_2^{\bullet+}$ abstraction products and upper for 1,3- $H_2^{\bullet+}$ abstraction products), as discussed in the text, they are likely to be close to the absolute yields.
- b. Includes both observed $[M-2H]^{\bullet-}$ ion and any fragmentation ions produced from 1,1- $H_2^{\bullet+}$ abstraction.

2.4.6. Miscellaneous considerations

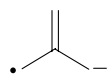
For the addition-elimination reaction, the product yields are controlled by thermodynamics. Acetone (3%) and 3-butanone (6%) give less addition-elimination products than 3-pentanone (21%) and 2,4-dimethyl-3-pentanone (65%); the observed general trend is consistent with both stability of the alkyl radical leaving group and the steric bulk of the reactant ketone. For 2-butanone, two addition-elimination products are observed with the ethyl group elimination favored 2:1 over the methyl group elimination. The lack of addition-elimination products for the cyclic ketones likely reflects both the unfavorability of a primary alkyl radical departing, and the unfavorable entropy change, as compared to acyclic ketones.

For several experiments with cyclopentanone (but never for any other ketone we examined), a small O_2^- signal is observed at long reaction times, the yield of which was highly variable. We propose that it comes from a charge transfer reaction from a cyclopentanone-derived radical anion to trace amounts of oxygen present in the system on those days. Confirmation of this hypothesis was obtained by adding a small amount of oxygen through port 1 (port nearest to the sampling orifice) during an otherwise normal O^+ plus cyclopentanone experiment. Under these conditions, the $[M-2]^+$ signal goes down and the O_2^- signal goes up with increased O_2 flow and are restored to their original intensities when the O_2 flow is stopped. This result shows that a secondary reaction takes place between a cyclopentanone radical anion and oxygen. Wenthold and co-workers [43] reported the electron affinity of the TMM diradical to be 0.43 eV, which is similar to the electron affinity of O_2 (0.45eV) [38]. Because of the higher electronegativity of oxygen as compared to carbon, one could expect that the EA of the 1,3-diradical derived from acetone to be much higher than TMM. The 1,3-diradical from cyclopentanone should have a similar electron affinity as the analogous species from acetone

(Figure 2.9). Therefore, we suggest that the 1,1- H_2^{*+} abstraction from cyclopentanone is able to transfer an electron to oxygen to produce O_2^- (i.e., that the EA of the α -carbon of cyclopentanone is less than or equal to the EA of O_2). The yields of O_2^- we observed are consistent with this explanation as well.

Reactive detachment (i.e., an anion-molecule reaction that is exothermic enough to permit the extra electron on the anionic product to detach) is always a consideration for these types of radical anion reactions, and is challenging to probe for the cases discussed herein due to the large number of ion products and the “stable” nature of the major ions. Our data, both without and with the presence of O_2 (which yields O_2^- that does not rapidly detach at 300K) are most consistent with the conclusion that reactive detachment is not an important process in these systems.

We can compare the results obtained in this work to that of O^{*-} reacting with acetaldehyde as examined by using the flowing afterglow technique and reported previously [30]: 32% of didehydro radical anion, 9% of HO^- , 34% of proton transfer product $[\text{M}-1]^-$, and 25% of product from addition-elimination, wherein 15% exhibits hydrogen elimination and 10% exhibits methyl elimination. Considering the unavailability of a 1,3- H_2^{*+} abstraction process, the enhanced acidity, and greater electrophilicity for the aldehyde, the ketone results reported here are consistent with acetaldehyde’s reaction.



Trimethylmethylene
(TMM) radical anion

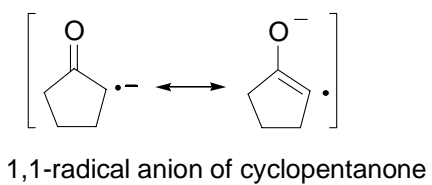
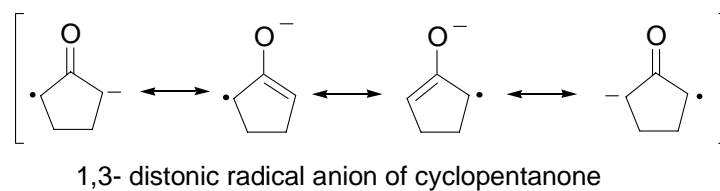
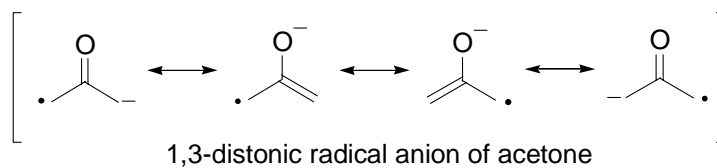


Figure 2.9. Structures of TMM, 1,3- distonic radical anion of acetone, 1,3-radical anion of cyclopentanone, and 1,1-radical anion of cyclopentanone

2.5. Conclusions

By using the flowing afterglow technique, $[M-2H]^{\bullet-}$ radical anions of cyclopentanone are successfully generated from the reaction of $O^{\bullet-}$ with cyclopentanone at 300K with a yield of 48%, wherein $\sim 15\%$ are from 1,1- and $\sim 33\%$ are from 1,3- $H_2^{\bullet+}$ abstraction. These yields are likely to be high enough, though challenging, for a NIPES study. The electron affinity of 1,1-diradical of cyclopentanone will be near or below O_2 . However, a complication is that $[M-2H]^{\bullet-}$ radical anions from the ketones examined are reactive with their parents: the 1,3- $H_2^{\bullet+}$ abstraction product reacts with a second equivalent of ketone via a proton transfer pathway and the 1,1- $H_2^{\bullet+}$ abstraction product when possible reacts with a second equivalent of ketone via an oxidation pathway. Preferably, the 1,1- $H_2^{\bullet+}$ abstraction product from methyl ketones undergo spontaneous fragmentation. Ketones that are not methyl ketones do not display this pathway, reflecting, perhaps, the greater stability of the alkyl substituted 1,1-radical anions and/or higher activation barrier for such fragmentations.

2.6. References

- [1] L. Salem and C. Rowland, *Angew. Chem. Int. Ed. Engl.* 11 (1972) 92-111.
- [2] P. Dowd, *J. Am. Chem. Soc.* 88 (1966) 2587-2589.
- [3] P. Dowd, *J. Am. Chem. Soc.* 92 (1970) 1066-1068.
- [4] J.A. Berson, *Structural Determinants of the Chemical and Magnetic Properties of Non-Kekule Molecules*, in: P.M. Lahti (Eds.), *Magnetic Properties of Organic Materials*, Marcel Dekker, Inc. New York, 1999, pp. 7-26.
- [5] J.A. Berson, *Acc. Chem. Res.* 30 (1997) 238-244.
- [6] H.K. Power and W.T. Borden, *J. Org. Chem.* 60 (1995) 2654-2655.
- [7] B.F. Yates, W.J. Bouma, and L.J. Radom, *J. Am. Chem. Soc.* 106 (1984) 5805-5808.
- [8] B.F. Yates, W.J. Bouma, and L.J. Radom, *Tetrahedron* 42 (1986) 6225-6234.

- [9] P.F. Zittel, G.B. Ellison, S.V. O'Neil, E. Herst, W.C. Lineberger, and W.P. Reinhardt, *J. Am. Chem. Soc.* 98 (1976) 3731-3732.
- [10] D.G. Leopold, A.E.S. Miller, and W.C. Lineberger, *J. Am. Chem. Soc.* 108 (1986) 1379-1384.
- [11] E.P. Clifford, P.G. Wenthold, W.C. Lineberger, G.B. Ellison, C.X. Wang, J.J. Grabowski, F. Vila, and K.D. Jordan, *J. Chem. Soc. Perkin Trans. 2* 5 (1998) 1015-1020.
- [12] J. Lee, P.K. Chou, P. Dowd, and J.J. Grabowski, *J. Am. Chem. Soc.* 115 (1993) 7902-7903.
- [13] M. Born, S. Ingemann, and N.M.M. Nibbering, *Mass Spectrom. Rev.* 16 (1997) 181-200.
- [14] A.G. Harrison, *Chemical Ionization Mass Spectrometry*. 2nd ed. 1992: CRC Press, Inc.
- [15] J. Lee and J.J. Grabowski, *Chem. Rev.* 92 (1992) 1611-1647.
- [16] Y. Guo and J.J. Grabowski, *J. Am. Chem. Soc.* 113 (1991) 5923-5931.
- [17] Y. Guo and J.J. Grabowski, *Int. J. of Mass Spectrom. Ion. Processes* 117 (1992) 299-326.
- [18] P.K. Chou and S.R. Kass, *J. Am. Chem. Soc.* 113 (1991) 697-698.
- [19] P.O. Staneke, S. Ingemann, P.N. Eaton, N.M.M. Nibbering, and S.R. Kass, *J. Am. Chem. Soc.* 116 (1994) 6445-6446.
- [20] M. Born, S. Ingemann, and N.M.M. Nibbering, *J. Am. Chem. Soc. Mass Spectrom.* 6 (1995) 71-75.
- [21] J. Kauw, M. Born, S. Ingemann, and N.M.M. Nibbering, *Rapid Commun. in Mass Spectrom.* 10 (1996) 1400-1404.
- [22] J. Zhao, P. Dowd, and J.J. Grabowski, *J. Am. Chem. Soc.* 118 (1996) 8871-8874.
- [23] A.G. Harrison and K.R. Jennings, *J. Chem. Soc. Faraday Trans. 1* 72 (1976) 1601-1608.
- [24] J.H.J. Dawson, A.J. Noest, and N.M.M. Nibbering, *Int. J. of Mass Spectrom. Ion. Phys.* 30 (1979) 189-191.
- [25] A. Marshall, T. Martin, and A.G. Harrison, *J. Am. Soc. Mass Spectrom.* 2 (1991) 292-298.
- [26] F.C. Fehsenfeld, A.L. Schmeltekopf, H.I. Schiff, and E.E. Ferguson, 15 (1967) 373-379.
- [27] E.E. Ferguson, *Flow Tube Studies of Ion-Molecule Reactions*, in: (Eds.), *Advances in Atomic Molecular Physics*, Academic Press, Inc, 1988.
- [28] S.T. Graul and R.R. Squires, *Mass Spectrom. Rev.* 7 (1988) 263-358.

- [29] H.E. Matimba, S. Ingemann, and N.M.M. Nibbering, *J. Am. Soc. Mass Spectrom.* 4 (1993) 73-81.
- [30] J.J. Grabowski and S.J. Melly, *Int. J. of Mass Spectrom. Ion. Processes* 81 (1987) 147-164.
- [31] R. Marx, G. Mauclaire, F.C. Fehsenfeld, D.B. Dunkin, and E.E. Ferguson, *J. Chem. Phys.* 58 (1973) 3267-3273.
- [32] K. Mitsuke, K. Kusafuka, and K. Ohno, *J. Phys. Chem.* 93 (1989) 3062-3068.
- [33] T. Su and W.J. Chesnavich, *J. Chem. Phys.* 76 (1982) 5183-5185.
- [34] D.R. Lide, ed. *CRC Handbook of Chemistry and Physics*. 84th ed. 2003-2004, CRC Press.
- [35] D.R. Anderson, V.M. Bierbaum, C.H. Depuy, and J.J. Grabowski, *Int. J. of Mass Spectrom. Ion. Phys.* 52 (1983) 65-94.
- [36] Isotopic distribution is calculated using IsoPro 3.0, a free MS/MS software package available from <http://members.aol.com/msmssoft>.
- [37] V. Baranov and D.K. Bohme, *Int. J. of Mass Spectrom. Ion. Phys.* 154 (1996) 71-88.
- [38] NIST Standard Reference Database Number 69 - March 2003 Release.
- [39] S.D. Tanner, G.I. Mackay, and D.K. Bohme, *Can. J. Chem.* 59 (1981) 1615-1621.
- [40] H. Van Der Wel and N.M.M. Nibbering, *Recl. Trav. Chim. Pays-Bas* 107 (1988) 479-490.
- [41] C.H. Depuy, *Mathematical and Physical Sciences* 118 (1984) 227-241.
- [42] V.M. Bierbaum, J.J. Grabowski, and C.H. Depuy, *J. Phys. Chem.* 88 (1984) 1389-1393.
- [43] P.G. Wenthold, J. Hu, R.R. Squires, and W.C. Lineberger, *J. Am. Chem. Soc.* 118 (1996) 475-476.

Chapter 3 Targeting Cleavage of the Peptide Amide Bond via Selective Gas-Phase Ion-Molecule Reactions

3.1. Introduction

The tandem mass spectrometry technique (MS/MS) has been widely used in protein identification and characterization [1-3]. In the most common approach for protein MS/MS sequencing, a protein is proteolytically digested into smaller peptides, then the digestion mixture is separated by chromatographic techniques. Individual peptides resulting from the digestion are ionized by appropriate ionization methods (including by ESI, MALDI or FAB) and then subjected to a collision induced dissociation (CID) process in the gas-phase. The amino acid sequence of a peptide is reconstructed based on interpreting the complementary a_n , b_n , c_n and x_n , y_n , z_n sequence ions [4] obtained from the CID process. The definitions of sequence ions from a protonated peptide are illustrated in Figure 3.1.

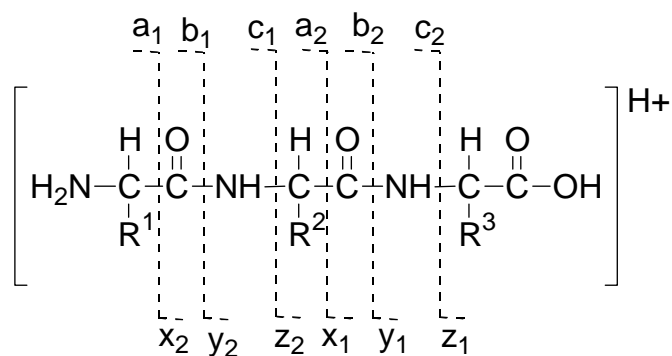


Figure 3.1. Definitions of peptide complementary a_n , b_n , c_n and x_n , y_n , z_n sequence ions.

MS/MS database searching is used to aid CID data interpretation and for protein identification [5]. However, the nonselective CID process using inert collision gas can produce a complicated spectrum that contains fragments resulting from peptide backbone bonds breaking

and side chain cleavages. Even a powerful program such SEQUEST typically identifies less than 40% of the peptides in a digestion of known protein [6]. Moreover, for a novel or a posttranslationally modified protein, the elucidation of its complete sequence remains a formidable challenge. Systematic approaches have been developed to deduce the sequence of parent peptides from the observed ions in their CID product ion spectra, but they are often time-consuming and laborious [7]. In addition, conventional CID methods suffer from decreasing efficiency of fragmentation with increasing molecular weight of the precursor ion due to the fact that the internal energy converted from the translational energy during the collision dissipates into more degrees of freedom in the larger molecule. Furthermore, conventional CID on a protonated peptide tends to favor fragments at arginine [8] or lysine [9] residues. A method that can produce a contiguous series of sequence ions from a parent peptide ion via selective backbone cleavage would be advantageous; such a method will simplify fragmentation product ion spectrum interpretation and facilitate the identification of peptide sequence through MS/MS product spectrum analysis. Several alternative peptide/protein gas-phase fragment methods have been examined. The most promising technique may be electron capture dissociation (ECD) [10-13], which allows protein/peptide cations to interact with near-thermal electrons to induce backbone cleavages, mainly producing c_n and z_n type ions. The fragmentation scheme for producing c_n and z_n type ions from a reaction between an electron and multiply protonated peptide during an ECD process is shown in Figure 3.2.

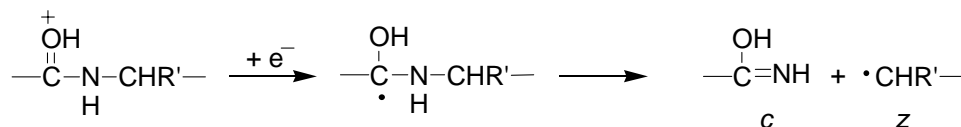


Figure 3.2. Electron capture dissociation scheme for the production of c_n and z_n type ions from a multiply protonated peptide.

ECD has been used as a top-down *de novo* sequencing technique due to its capability to sequence an intact protein without prior enzymatic proteolysis [14]. ECD can only be used to a Fourier transform ion cyclotron resonance (FT-ICR) mass spectrometry and the fragmentation efficiency in an ECD process is only ~30%. Electron transfer dissociation (ETD) [15, 16], which utilizes ion/ion reactions between multiply protonated peptides and anions, is capable of generating c_n - and z_n - fragments via a mechanism similar to ECD in a less expensive ion trap instrument. However, ETD suffers from the competition of proton transfer and low fragmentation efficiencies (~30%). Other techniques that have been used in peptide sequencing include photon dissociation [17, 18], infrared multiphoton dissociation (IRMPD) [19, 20], surface induced dissociation (SID) [21-24]. These techniques have been used as a supplement to CID method for peptide sequencing.

Using gas-phase ion-molecule reactions to sequence a peptide ion is an attractive alternative. Unlike the conventional CID process in which peptide backbone breaking is induced via depositing excess kinetic energy in peptide ions during an energetic collision, chemical cleavages break peptide bonds via specific chemical reactions between designer reagent neutrals and peptide ions in the gas-phase. The few literature reports of attempts to cleave peptide backbones via gas-phase ion-molecule reactions involve nucleophile-electrophile interactions [25]. For instance, Freitas et al. [26, 27] demonstrated that the methoxymethyl cation, as an electrophile, can cleave the amide bond in a neutral peptide, although other reaction pathways leading to non-cleavage products are also observed (Figure 3.3).

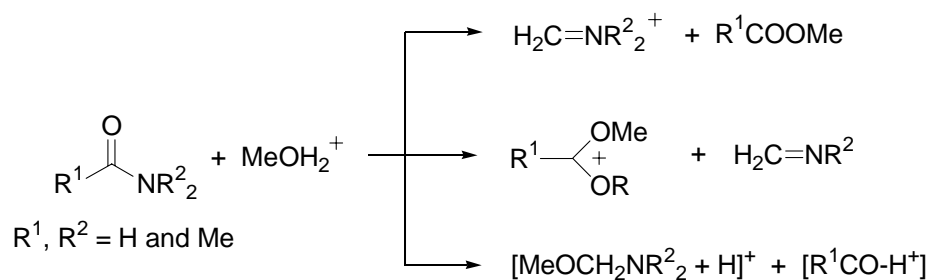


Figure 3.3. Ion-molecule reactions of methoxymethyl cation with peptide analogs. Figure adapted from [26].

Fenselau and co-workers [28-31] illustrated that collision induced dissociation using NH_3 or amines decrease the threshold of producing fragments, though the detailed mechanism is not clear. O'Hair et al. [32] explored the possibility of cleaving peptide bonds via transacylation reaction using NH_3 or amine as nucleophiles, (Figure 3.4). Despite these efforts, no chemical reagent that can specifically and efficiently cleave a peptide in the gas-phase has been found.

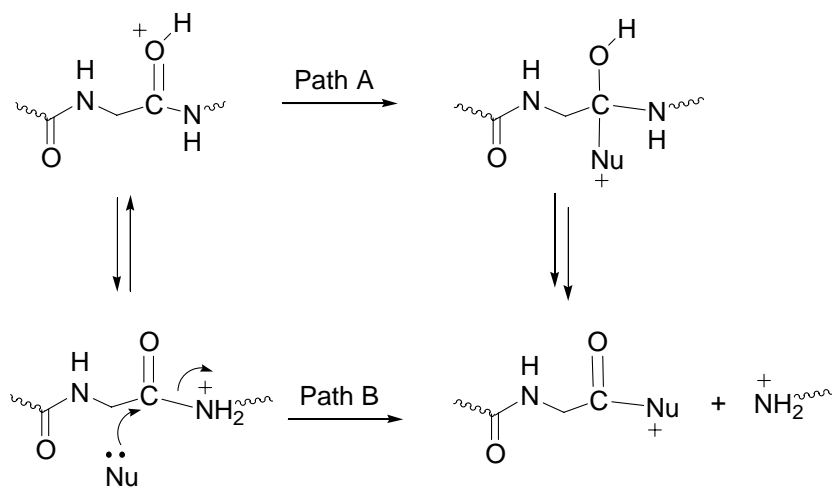


Figure 3.4. Proposed scheme for peptide bond cleavage via transacylation reaction. Figure adapted from [32].

Amide bond cleavage using a deprotonated amide has been demonstrated by Cheng et al. [33] in the reactions of small peptide analogs with selected designer reagents using a flowing afterglow. Considering the inert chemical properties of amide bonds [34-36], an X-Y reagent, with the Y portion of the molecule intended to activate the amide bond and the X portion of the molecule to cleave the amide bond, is envisioned as a gas-phase cleaving reagent, shown in Figure 3.5.

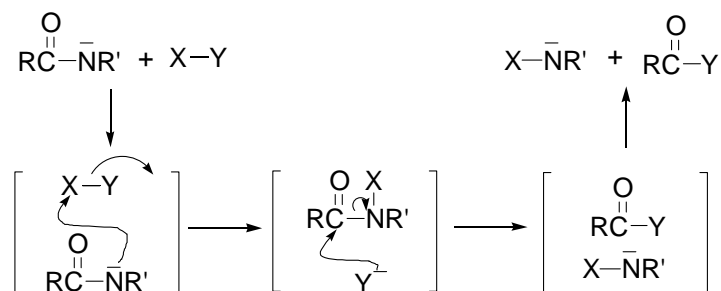
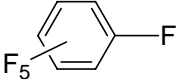
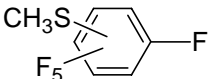
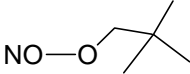


Figure 3.5. Strategy of a X-Y designer reagent cleaving the amide bond in a peptide analog.

Among several X-Y reagents studied, S-ethyl trifluorothioacetate (CF_3COSEt) was the most promising: the reaction is fast and 90% of product ions originate from amide bond cleavage, as shown in Table 3.1.

Table 3.1. Results of the gas-phase ion-molecule reactions between $\text{CH}_3\text{CON}(\ominus)\text{CH}_3$ and selected X-Y reagents. Data has been presented on the 39th ASMS Conference at Mass Spectrometry and Allied Topics [33].

Cleavage observed			Cleavage not observed	
X-Y	X-NCH_3		X-Y	Product observed
$\text{CF}_3\text{C}(=\text{O})\text{SEt}$	90%	fast	$\text{CF}_3\text{S}(=\text{O})_2\text{OCH}_3$	$\text{CF}_3\text{SO}_3^-/\text{CF}_3\text{SO}_2^-$ (fast)
$\text{CF}_3\text{C}(=\text{O})\text{OPh}$	25%	fast	$\text{CF}_3\text{C}(=\text{O})\text{OEt}$	CF_3CO_2^- (slow)
	70%	medium	$\text{CH}_3\text{S}(=\text{O})_2\text{SCH}_3$	$\text{CH}_3\text{SO}_2^-/\text{CH}_3\text{SO}_2\text{SCH}_3^-/\text{CH}_3\text{SO}_2\text{S}^-$ (medium)
	25%	medium	$\text{PhC}(=\text{O})\text{OOtBu}$	Unidentified products (slow)
	30%	slow	tBuO-OtBu	No reaction

The proposed mechanism for CF_3COSEt cleaving a negatively charged peptide analog ion, $\text{CH}_3\text{CON}^-\text{CH}_3$, is shown in Figure 3.6. The cleavage starts with nucleophilic addition by the negatively charged nitrogen atom at the carbonyl group in CF_3COSEt , followed by ^-SEt ion expulsion from the tetrahedral intermediate. The new ion-molecule complex reacts via nucleophilic attack by ^-SEt at the carbonyl group in the newly activated amide. Although X-Y reagents, such as CF_3COSEt , have shown high efficiency at cleaving the amide bonds in small peptide analogs, the direct application of such X-Y reagents to cleave typical peptides is limited: it is difficult to generate the negatively charged peptide as required by the cleavage mechanism proposed in Figure 3.6.

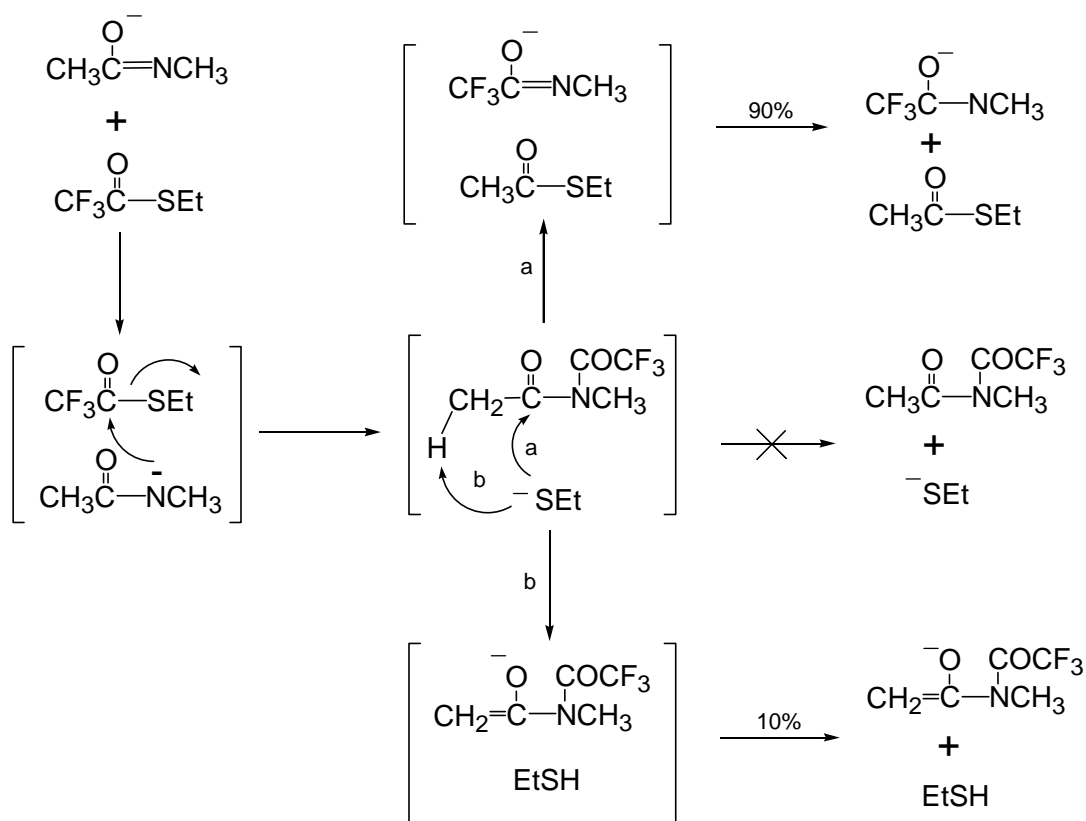
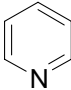
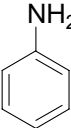
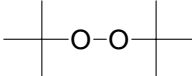


Figure 3.6. Proposed mechanism for CF_3COSEt cleaving deprotonated N-methylacetate ion.

Ion-molecule reactions between positively charged peptide analog ions and selective chemical reagents have also been examined in the flowing afterglow [37], as summarized in Table 3.2. Unfortunately, the general observations for these reactions are either a cation transfer from the positive charged peptide ion to the neutral reagent when the reaction is exothermic, or the formation of clusters when the cation transfer reaction is endothermic. Since the reactions in a flowing afterglow are carried out under thermal energy (i.e., room temperature), endothermic reactions are too slow to be observed. A device that can derive endothermic reactions is necessary to increase the probability of success for a peptide amide bond gas-phase cleavage reagent. Therefore, an electrospray triple quadrupole instrument, which is capable of performing endothermic reactions through collisional activation, is adopted in the search for peptide cleaving reagents, in this study.

The search for peptide chemical cleavage reagents starts with good nucleophiles. An α -nucleophile, which has anomalously high nucleophilic reactivity due to the one or more lone pairs of lone electrons at an atom adjoining to its nucleophilic center [38, 39], appears to be an ideal candidate for peptide cleavage. Hydrazine, one of the most extensively studied α -nucleophiles, was chosen to be examined for its reactivity toward peptide amide bonds in the gas-phase. Other reagents, including ethylenediamine, formic acid and acetic anhydride, were tested on various peptides based on proposed cleavage mechanisms.

Table 3.2. Summary of ion-molecule reactions between positive analogs with selected neutral examined in the flow afterglow. PT stands for proton transfer; NR stands for no reaction.

Precursor ion	Neutral	Reactions observed
	NH_2NH_2	cluster
$\text{H}_3\text{C}-\overset{\text{+}}{\text{C}}(\text{OH})-\text{N}(\text{CH}_3)_2$		PT, cluster
	$\text{CH}_3\text{CONHCH}_3$	cluster
	PhPH_2	PT, cluster
$\text{H}_3\text{C}-\overset{\text{+}}{\text{C}}(\text{OCH}_3)-\text{N}(\text{CH}_3)_2$		NR
	$\text{NH}_2\text{CH}_2\text{CH}_2\text{NH}_2$	cluster
	CF_3COSEt	cluster
$\text{H}_3\text{C}-\overset{\text{+}}{\text{C}}(\text{OH})-\text{NHCH}_3$ / $\text{H}_3\text{C}-\overset{\text{+}}{\text{C}}(\text{OCH}_3)-\text{NHCH}_3$ / $\text{H}_3\text{C}-\overset{\text{+}}{\text{C}}(\text{OC}_2\text{H}_5)-\text{NHCH}_3$ mixture	HOOH	cluster
		cluster
	$\text{CH}_3\text{COOCH}_3$	cluster
$\text{H}_3\text{C}-\overset{\text{+}}{\text{C}}(\text{OH})-\text{NHCH}_3$ / $\text{H}_3\text{C}-\overset{\text{+}}{\text{C}}(\text{OC}_2\text{H}_5)-\text{NHCH}_3$ / $\text{H}_3\text{C}-\overset{\text{+}}{\text{C}}(\text{OC}_3\text{H}_7)-\text{NHCH}_3$ mixture	$\text{CH}_3\text{COSCH}_3$	cluster
	CS_2	NR
	Ac_2O	cluster
	CF_3COOPh	cluster

3.2. Experimental

The custom-built electrospray ionization triple quadrupole mass spectrometer (ESI-TQMS) used in this study, shown in Figure 3.7, has been described elsewhere [40]. Briefly, two quadrupole mass filters with mass ranges up to 2000 amu (Extrel Inc, Pittsburgh, PA) are used as the first-stage (Q_1) and third-stage (Q_3) mass analyzers; an RF-only octopole (Q_2) is used as a collision cell located in a gas-tight housing between Q_1 and Q_3 . These three multipoles are housed in a stainless steel chamber pumped by a 700 l/s Edwards Diffstak diffusion pump and a 360 l/s Leybold-Heraeus turbo pump. An conversion dynode and an electron multiplier are used to detect ions. The electrospray interface, shown in Figure 3.8, consists of a 6.5 cm long, 1.5 mm i.d. stainless steel inlet capillary and two skimmers (the one immediately after the inlet desolvation capillary has an i.d of 1.0 mm; the other one has an i.d. of 0.75mm). The inlet capillary can be heated to 200 °C by two cartridge heaters that are in contact with the capillary assembly. A set of three Enizel lenses is used to guide and focus ions coming out of the ESI interface into Q_1 . Two-stage differential pumping in the ESI interface is maintained by two 4.4 l/s Pfeifer Balzers mechanical pumps. The typical operational conditions applied on the ESI interface are: 150 °C on heated capillary, +70 V on heated capillary, +50 V on skimmer 1 and +35 V on skimmer 2. Merlin Automation software (Version 1.0.15, Extrel, Inc) is used both for instrument control and data analysis.

Various gases and chemicals are allowed into the collision chamber via a stainless steel gas manifold, which is connected to the chamber via a flow-regulating metering valve mounted on the back flange. Liquid chemicals are placed in glass flask reservoirs fitted with Teflon stoppers connected to the gas manifold through Cajun vacuum fittings (Swagelok Company). Gas inlet lines are connected to the manifold through gas-tight Swagelok fittings from gas tanks

equipped with pressure regulators. Different gases or chemicals can be introduced into the chamber by opening appropriate valves on the manifold. A mechanical pump connected to the manifold is used to pump away any residual gases when switching gases.

The typical procedure for a MS/MS experiment performed on the TQMS in the present study is as following: a peptide ion generated by electrospray is mass isolated by Q_1 and allowed to react with a neutral reagent in the octopole collision chamber at various collision energies; the product ions are then recorded by scanning Q_3 . For a positively charged peptide ion generated from the electrospray source under typical operational conditions, a positive pole bias offset of 15-25V can completely retard ion transmission through the octopole. Thus a pole bias offset less than 15V results in an attractive potential and accelerates ions when they travel from Q_1 into Q_2 . Therefore, by varying Q_2 pole bias offset, various collision energies can be achieved. Pressure in the collision chamber is monitored by an ion gauge located in the turbo pump inlet (with a typical reading of $1.0\text{-}3.0 \times 10^{-5}$ Torr during MS/MS) and an ion gauge connected to the collision chamber with an 1/8-inch stainless steel tubing (with a typical reading $1.0\text{-}3.0 \times 10^{-4}$ Torr during MS/MS). The ion gauges are calibrated with nitrogen and air by the manufacturer and are used as received.

The nanospray emitters used for electrospray are fabricated from 75 μm i.d. fused silica capillaries using a capillary puller (P-2000 CO₂ laser puller, Sutter Instruments, Novato, CA). The nanospray emitter is connected through a metal union where a 1.8-2.5 kV voltage is applied to a 75 μm i.d. capillary. The analyte solution is delivered by a syringe pump (Harvard Apparatus) with a flow rate of 0.1-0.2 $\mu\text{l}/\text{ml}$. Protonated peptide ions were generated from peptide solutions in 49.5:49.5:1 methanol:H₂O:acetic acid; sodiated or lithiated peptide ions are obtained from peptide solutions in 50:50 methanol:H₂O with 5mM NaCl or 5mM LiCl added.

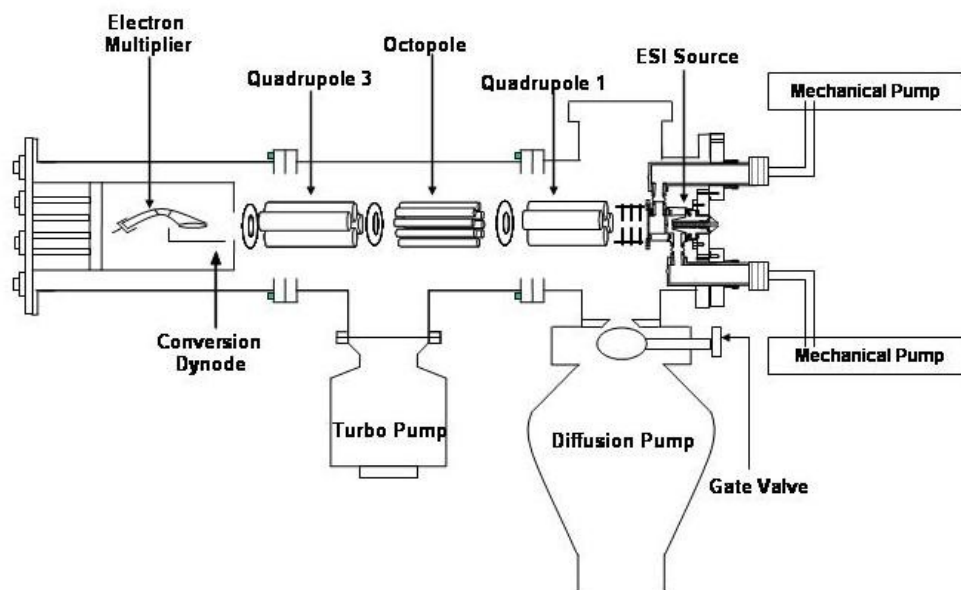


Figure 3.7. Schematic diagram of the custom-built ESI-triple quadrupole mass spectrometer equipped with an electrospray source.

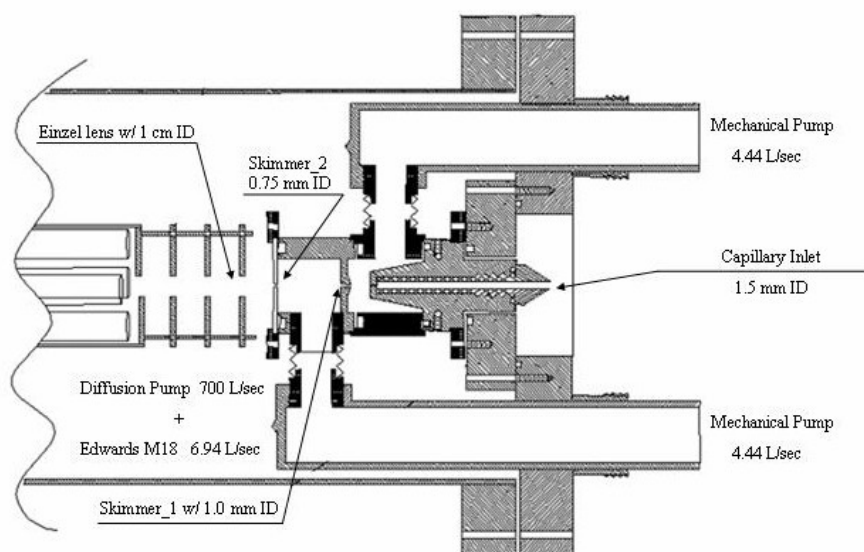
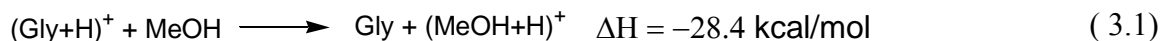


Figure 3.8. Diagram of the ESI interface in the ESI-TQMS.

3.3. Results

3.3.1. Endothermic proton transfer

The proton affinity of methanol is 183.5 kcal/mol [41] and the proton affinity of glycine is 211.9 kcal/mol [41]. Thus, the proton transfer from a protonated glycine ion to a neutral methanol molecule is endothermic by 28.4 kcal/mol (1.2 eV).



Shown in Figure 3.9(a-c), by supplying a 5 eV collision energy in the lab frame, which is 1.5 eV in the center-of-mass frame, the endothermic proton transfer from the protonated glycine to methanol is observed. MS/MS experiments performed on this study are represented by a symbolic system proposed by Cooks and co-workers [42]. A filled cycle (●) represents the precursor ion; an open cycle (○) represents product ions. An arrow pointing from the filled cycle to the open cycle illustrates that product ions observed are produced from a MS/MS experiment on the precursor ion. The target gas used is indicated on the right side of the arrow. Note that the conversion of collision energy between the center-of-mass frame, $\langle KE_{CM} \rangle$, and the lab frame, $E(\text{lab})$, is

$$\langle KE_{CM} \rangle = E(\text{lab}) \times \frac{M(\text{MeOH})}{M(\text{GlyH}) + M(\text{MeOH})} \quad (3.2)$$

where $M(\text{MeOH})$ is the molecular weight of methanol and $M(\text{GlyH})$ is the molecular weight of protonated glycine. A control experiment with Ar as collision gas at the same center-of-mass collision energy fails to afford any proton transfer from the protonated glycine to Ar due to the low proton affinity of Ar ($\text{PA} = 88.24 \text{ kcal/mol}$ [41]), which would indicate a 123.7 kcal/mol endothermic reaction.

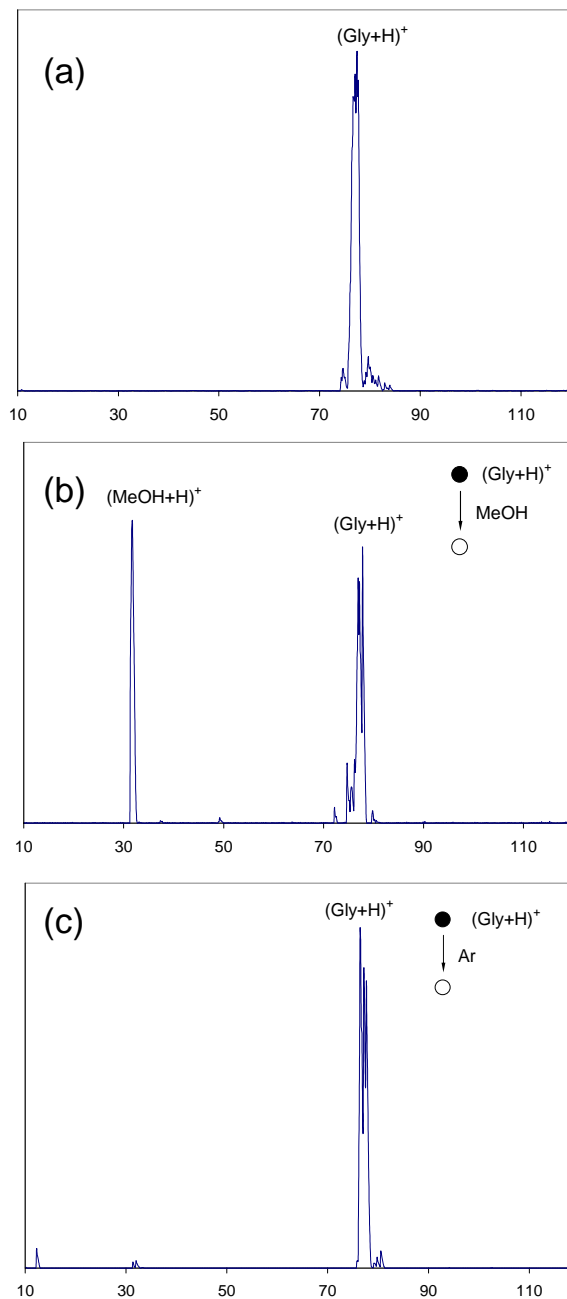


Figure 3.9. Endothermic proton transfer from a protonated glycine to methanol. (a) SIM spectrum of protonated glycine, generated from ESI of a glycine solution. (b) Product ion spectrum when methanol is used as collision gas at $\langle \text{KE}_{\text{cm}} \rangle = 1.5$ eV; protonated MeOH is observed. (c) Product ion spectrum when Ar is used as collision gas at $\langle \text{KE}_{\text{cm}} \rangle = 1.5$ eV. (Illustrations: filled cycle (\bullet) – precursor ion; open cycle (\circ) – product ions; target gas – indicated on the right side of the arrow.)

3.3.2. Leucine-enkephalin MS/MS experiments with hydrazine

Hydrazine (NH_2NH_2), an α -nucleophile, is used as collision gas in the MS/MS experiment of leucine-enkephalin (LeuEnk, YGGFL, Figure 3.10).

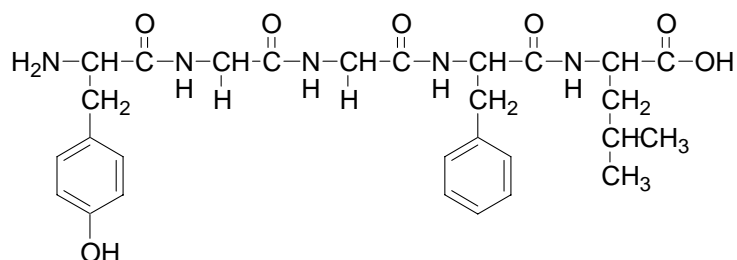


Figure 3.10. Structure of Leucine-enkephaline (YGGFL, MW=555).

Shown in Figure 3.11(a), a protonated, lithiated, and two-lithium adduct ($\text{LeuEnk}+2\text{Li-H}$)⁺ are observed from the electrospray spectrum of a 50 μM LeuEnk solution containing 5mM LiCl solution in 50:50 MeOH/ H_2O . Similarly protonated, sodiated, and ($\text{leuEnk}+2\text{Na-H}$)⁺ are observed from the electrospray spectrum of a 50 μM LeuEnk solution containing 5mM NaCl (data not shown). The MS/MS experiment on protonated LeuEnk with hydrazine as collision gas produces a ($\text{LeuEnk}+\text{H}+\text{NH}_2\text{NH}_2$)⁺ adduct ion at low collision energies along with some fragments originating from the protonated LeuEnk, as shown in Figure 3.11(c). At higher collision energies, the adduct ion disappears and fragments assigned as a_4 , b_4 , y_2 , y_3 , etc. are observed, as shown in Figure Figure 3.11(d). These fragments are also obtained from Ar CID control experiments (data not shown). As shown in Figure 3.12(a), the Ar CID on lithiated LeuEnk ion produces a modified b_n ion ($b_n\text{-OLi}$) with the Li^+ forming an ion pair with C-terminal carboxylate (See Discussion 3.4.1 for its structure). The MS/MS experiment on the lithiated LeuEnk ion with hydrazine as collision gas yields an adduct of protonated LeuEnk and hydrazine ($\text{LeuEnk}+\text{Li}+\text{NH}_2\text{NH}_2$)⁺ along with $b_3\text{-OLi}$ and $b_4\text{-OLi}$ (Figure 3.12(b)).

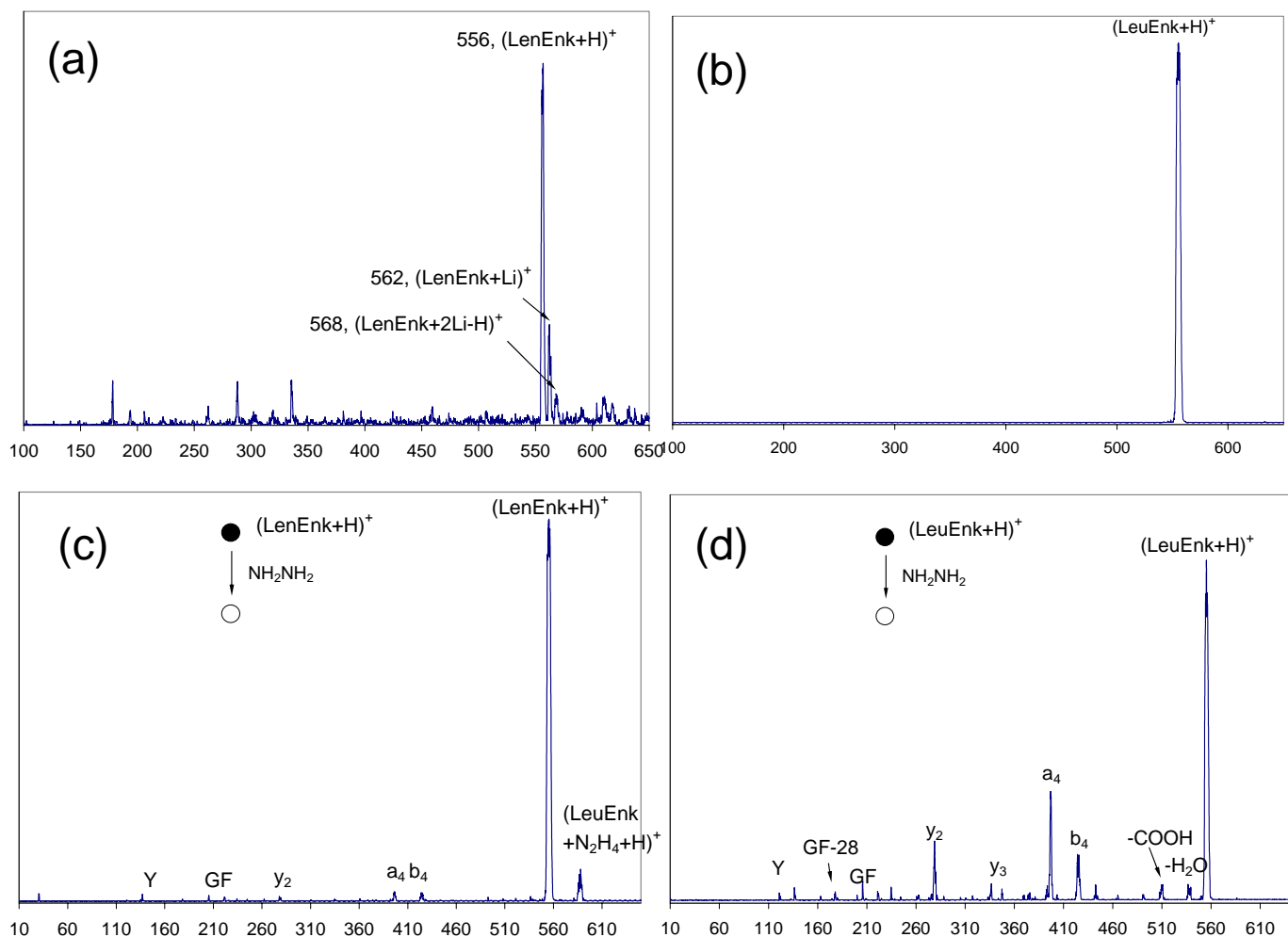


Figure 3.11. LeuEnk CID experiment using hydrazine as collision gas. (a) Electrospray spectrum of a 50 μM LeuEnk solution with 5mM LiCl in 50:50 MeOH/ H_2O . (b) SIM spectrum of protonated LeuEnk. (c) Product ion spectrum of protonated LeuEnk at $\langle KE_{cm} \rangle = 0.3\text{ eV}$. (d) Product ion spectrum of protonated LeuEnk at $\langle KE_{cm} \rangle = 0.8\text{ eV}$.

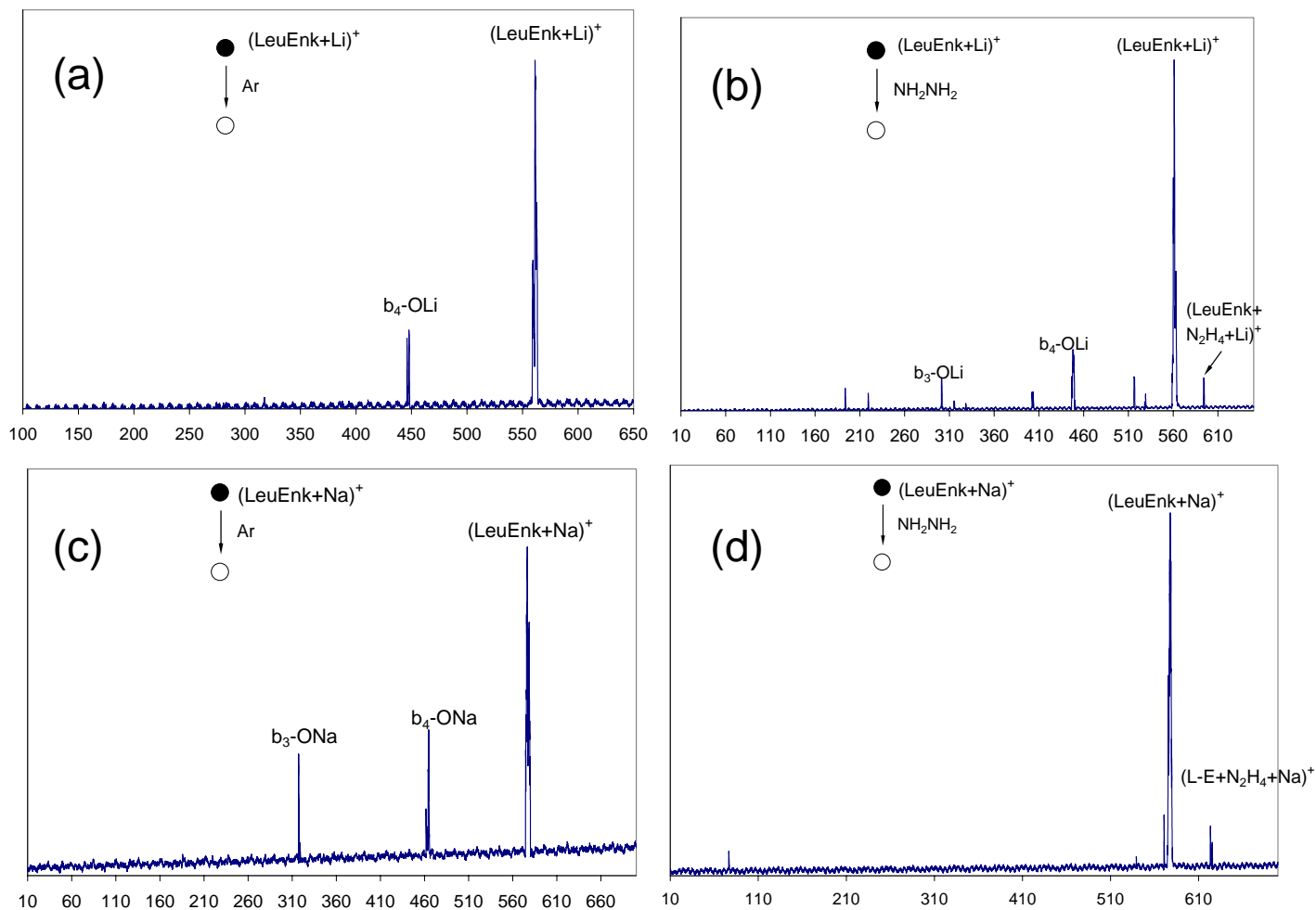


Figure 3.12. (a) Product ion spectrum of lithiated LeuEnk using Ar as collision gas at $\langle KE_{cm} \rangle = 1.3$ eV. (b) Product ion spectrum of lithiated LeuEnk using hydrazine as collision gas at $\langle KE_{cm} \rangle = 0.8$ eV. (c) Product ion spectrum of sodiated LeuEnk using Ar as collision gas at $\langle KE_{cm} \rangle = 1.3$ eV. (d) Product ion spectrum of sodiated LeuEnk using hydrazine as collision gas at $\langle KE_{cm} \rangle = 0.8$ eV.

No expected cleavage product $(b_n\text{-NHNH}_2+\text{Li})^+$ is observed (Figure 3.13). Two ion, $b_3\text{-ONa}$ and $b_4\text{-ONa}$ ions are observed in Ar CID on sodiated LeuEnk (Figure 3.12(c)). An adduct of sodiated LeuEnk and hydrazine $(\text{LeuEnk}+\text{Na}+\text{NH}_2\text{NH}_2)^+$ is observed in the MS/MS experiment using NH_2NH_2 as collision gas (Figure 3.12(d)); no specific cleavage product ion is observed. The product ions observed from MS/MS experiments on LeuEnk, along with products observed from other peptides examined in following sections, are summarized on Table 3.3.

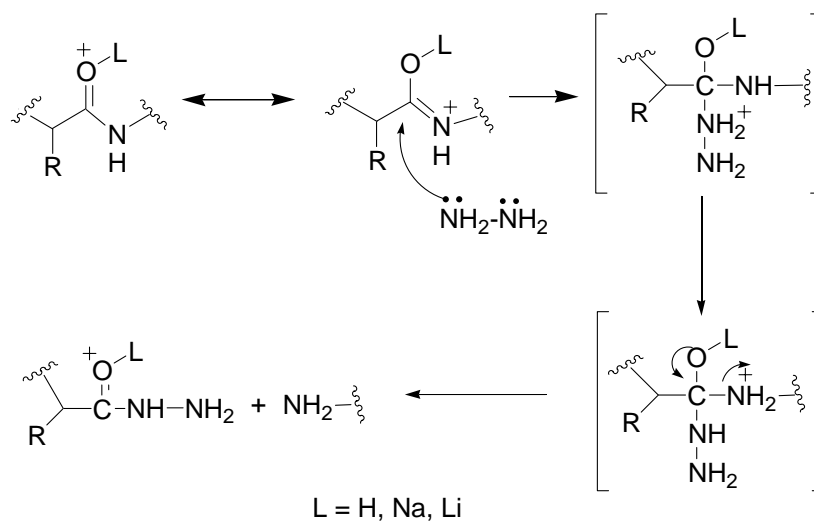


Figure 3.13. Hypothetical mechanism for hydrazine cleaving an amide bond in a cationized peptide ion in the gas-phase.

3.3.3. GGFL-NH₂ MS/MS experiments with hydrazine and ethylenediamine

[des-Tyr1]-Leucine-enkephalinamide (GGFL-NH₂, Figure 3.14), a C-terminal amide peptide is used as a model for C-terminal modified peptides in MS/MS experiments.

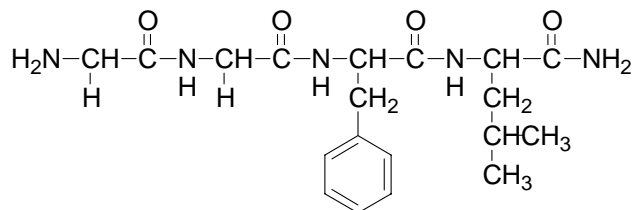


Figure 3.14. Structure of [des-Tyr1]-Leucine enkephalinamide (GGFL-NH₂, MW=391)

The ESI spectrum of GGFL-NH₂, the selected ion monitoring (SIM) spectrum of protonated GGFL-NH₂ and the product ion spectrum of Ar CID on protonated GGFL-NH₂ are shown in Figure 3.15(a-c). In the electrospray spectrum of GGFL-NH₂, protonated monomer, and both proton-bound homodimer and homotrimer are observed. The Ar CID of protonated monomer yields neutral loss ions (M+H-NH₃)⁺ and (M+H-CO-NH₃)⁺, as well as b₂ and y₂ ions. The ESI spectrum of a GGFL-NH₂/NaCl solution, the SIM spectrum of sodiated GGFL-NH₂ and the product ion spectrum of its Ar CID are shown in Figure 3.16(a-c). In the ESI spectrum, in addition to the observation of protonated monomer, proton-bound homodimer and homotrimer ions, we also observe sodiated monomer, and both sodium-bound homodimer and homotrimer ions. Ions observed from Ar CID on sodiated GGFL-NH₂ are assigned as (a₃+Na)⁺, (y₂+Na)⁺, and neutral loss from the sodiated monomer.

MS/MS experiments on protonated GGFL-NH₂ using hydrazine as collision gas yield abundant adduct ions, as shown in Figure 3.17(a). In addition to the product ions as observed from the Ar CID experiment, the adducts of the protonated parent ion with one and two hydrazine molecules, (M+H+NH₂NH₂)⁺ and (M+H+2NH₂NH₂)⁺ are observed. The adducts between normal CID fragments with one or two hydrazine molecules are also observed, e.g. (b₃+NH₂NH₂)⁺ and (b₃+2NH₂NH₂)⁺. For hydrazine MS/MS experiment on sodiated GGFL-NH₂, the same ions as produced in the Ar CID experiment are observed (Figure 3.17(b)). Similar to the hydrazine experiment, the MS/MS experiment on protonated GGFL-NH₂ using ethylenediamine (EDA) as collision gas produces adduct ions between the parent ion with EDA and fragment ions with EDA, shown in Figure 3.17(c). The EDA MS/MS experiment on sodiated GGFL-NH₂ produces adducts between the parent ion and EDA, along with normal CID fragment ions shown in Figure 3.17(d)

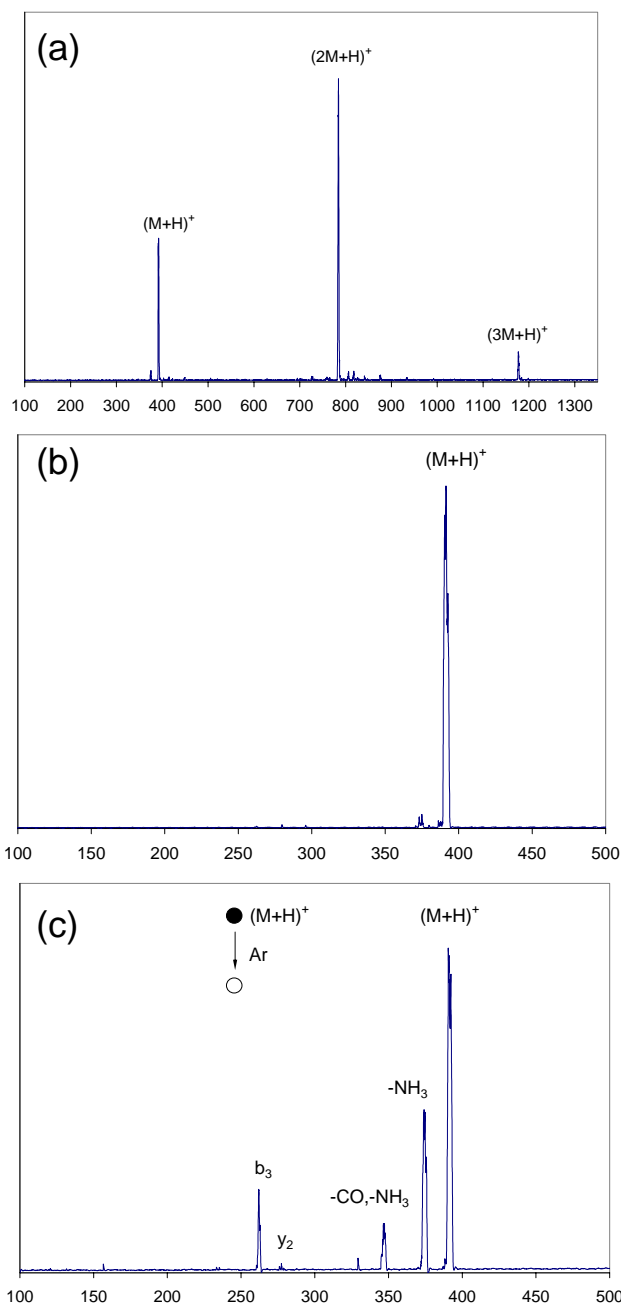


Figure 3.15. (a) Electrospray spectrum of a 50 μM GGFL-NH₂ solution in 49.5:49.5:1 MeOH/H₂O/Acetic acid solution (M stands for the neutral molecule, GGFL-NH₂). (b) SIM spectrum of protonated GGFL-NH₂, a small amount of (M+H-NH₃)⁺ is observed possible due to the CID resulting from the residue gas in the collision chamber. (c) Product ion spectrum of Ar CID on protonated GGFL-NH₂.

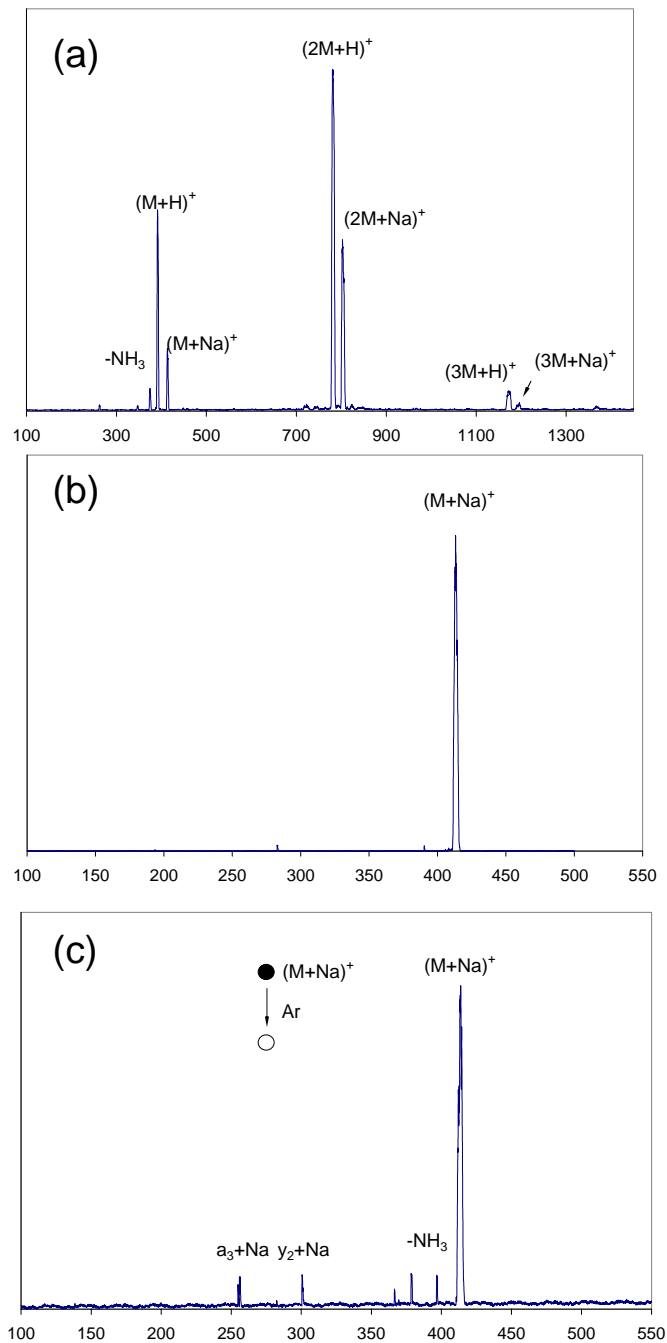


Figure 3.16. (a) Electrospray spectrum of a 50 μM GGFL- NH_2 solution with 5mM NaCl added. (M stands for the neutral molecule of GGFL- NH_2). (b) SIM spectrum of sodiated GGFL- NH_2 . (c) Product ion spectrum of Ar CID on sodiated GGFL- NH_2 .

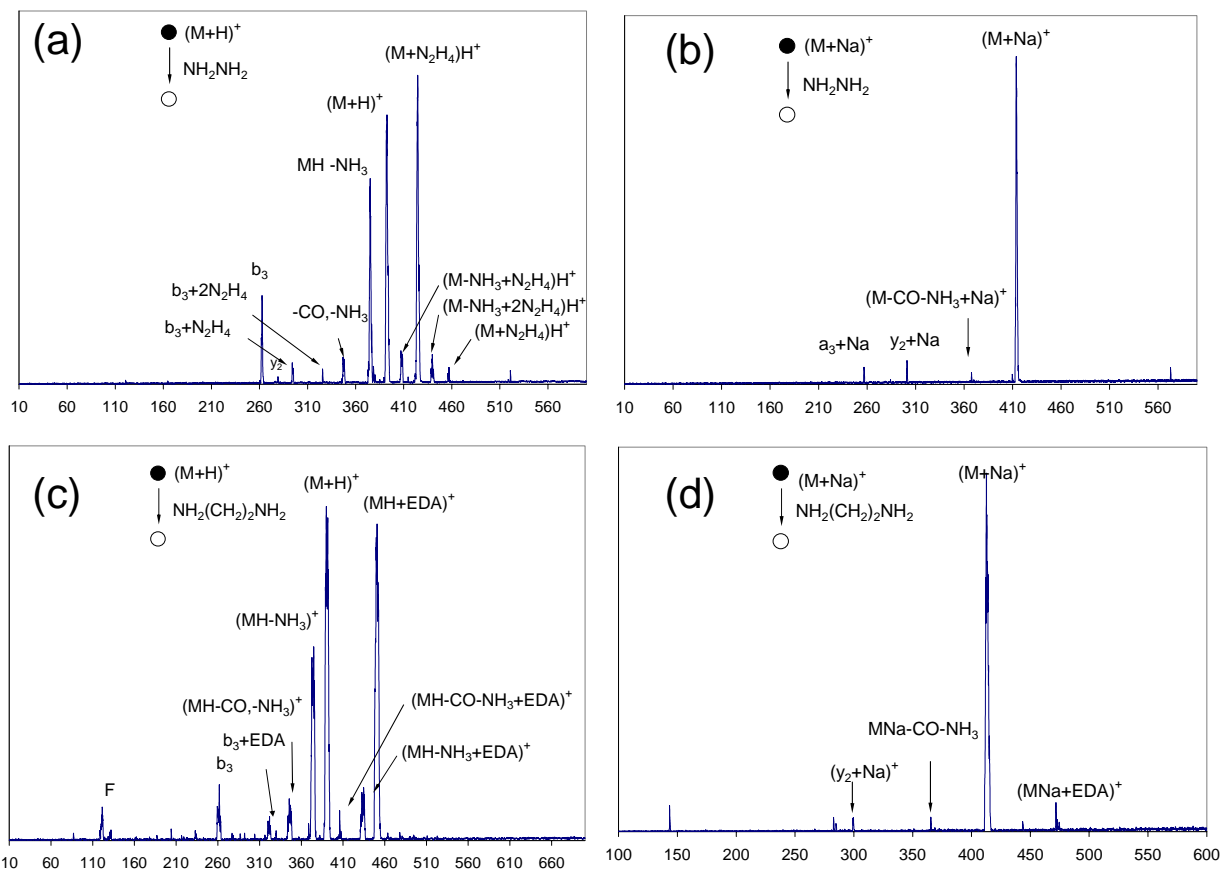


Figure 3.17. (a) Product ion spectrum of protonated GGFL-NH₂ with hydrazine as collision gas at $\langle KE_{cm} \rangle = 0.4\text{ eV}$. (b) Product ion spectrum of protonated GGFL-NH₂ with hydrazine as collision gas at $\langle KE_{cm} \rangle = 1.2\text{ eV}$ (c) Product ion spectrum of protonated GGFL-NH₂ with ethylenediamine as collision gas at $\langle KE_{cm} \rangle = 0.7\text{ eV}$. (b) Product ion spectrum of sodiated GGFL-NH₂ with ethylenediamine as collision gas at $\langle KE_{cm} \rangle = 1.8\text{ eV}$.

3.3.4. GGFL-NH₂ MS/MS experiments with formic acid and acetic anhydride

To examine the effects of eliminating the competition from the peptide C-terminal carboxylate while introducing a carboxylate group in the collision targets, formic acid (HCOOH) and acetic anhydride (Ac₂O) were used as collision gases with sodiated GGFL-NH₂ ion. (See Figure 3.22 for the proposed scheme for a carboxylate containing molecule cleaving a C-terminal amide peptide.) Shown in Figure 3.18(a-b), the adducts between sodiated GGFL-NH₂ and HCOOH are observed; at higher collision energies, the same fragments as observed in the Ar CID on sodiated GGFL-NH₂ are observed. Similarly, in the MS/MS experiment with Ac₂O as target, adducts between sodiated GGFL-NH₂ and Ac₂O are observed; normal CID fragment ions are also observed at higher collision energies, along with adducts of fragments (Figure 3.18(c-d)).

3.3.5. Ar CID on noncovalent complexes generated from solutions

Instead of forming adducts between positively charged peptide ions and targets in the gas-phase during their encounter in the collision chamber, a noncovalent complex can be pre-formed in solution and then transferred to gas phase via electrospray ionization. As shown in Figure 3.19(a), an adduct ion between GGFL-NH₂ and hydrazine is observed from the ESI spectrum of a mixture solution containing GGFL-NH₂ and hydrazine. The Ar CID on this proton-bound complex at low collision energies yields protonated GGFL-NH₂ by eliminating hydrazine from the complex (Figure 3.19(b)), which is consistent with their proton affinity order (PA(NH₂NH₂) = 203.9 kcal/mol [41]; PA of GGFL-NH₂ is expected to be much larger than glycine (211.9 kcal/mol [41])). At higher collision energies, normal CID fragments from protonated GGFL-NH₂ are observed due to possible multiple collisions, shown in Figure 3.19(c).

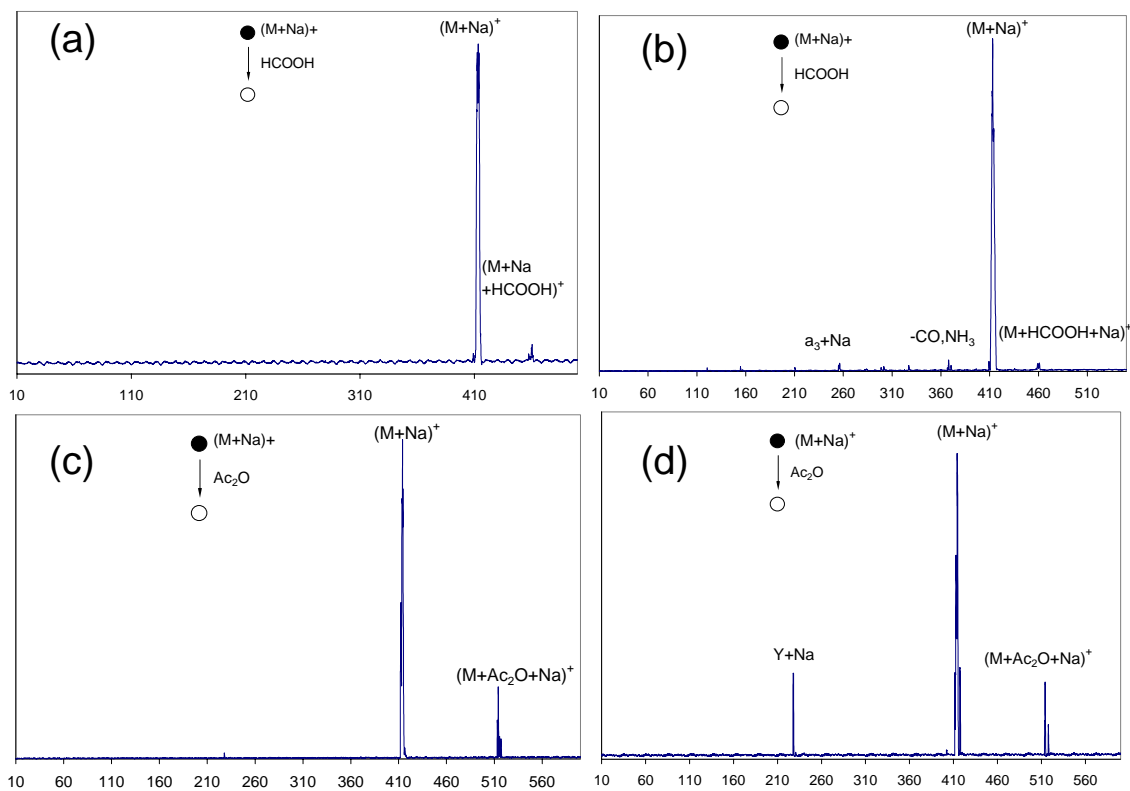


Figure 3.18. (a) Product ion spectrum of sodiated GGFL-NH₂ with formic acid as collision gas at $\langle KE_{cm} \rangle = 0.5$ eV. (b) Product ion spectrum of sodiated GGFL-NH₂ with formic acid collision gas at $\langle KE_{cm} \rangle = 1.1$ eV. (c) Product ion spectrum of sodiated GGFL-NH₂ with acetic anhydride as collision gas at $\langle KE_{cm} \rangle = 0$ eV. (d) Product ion spectrum of sodiated GGFL-NH₂ with acetic anhydride as collision gas at $\langle KE_{cm} \rangle = 1.0$ eV.

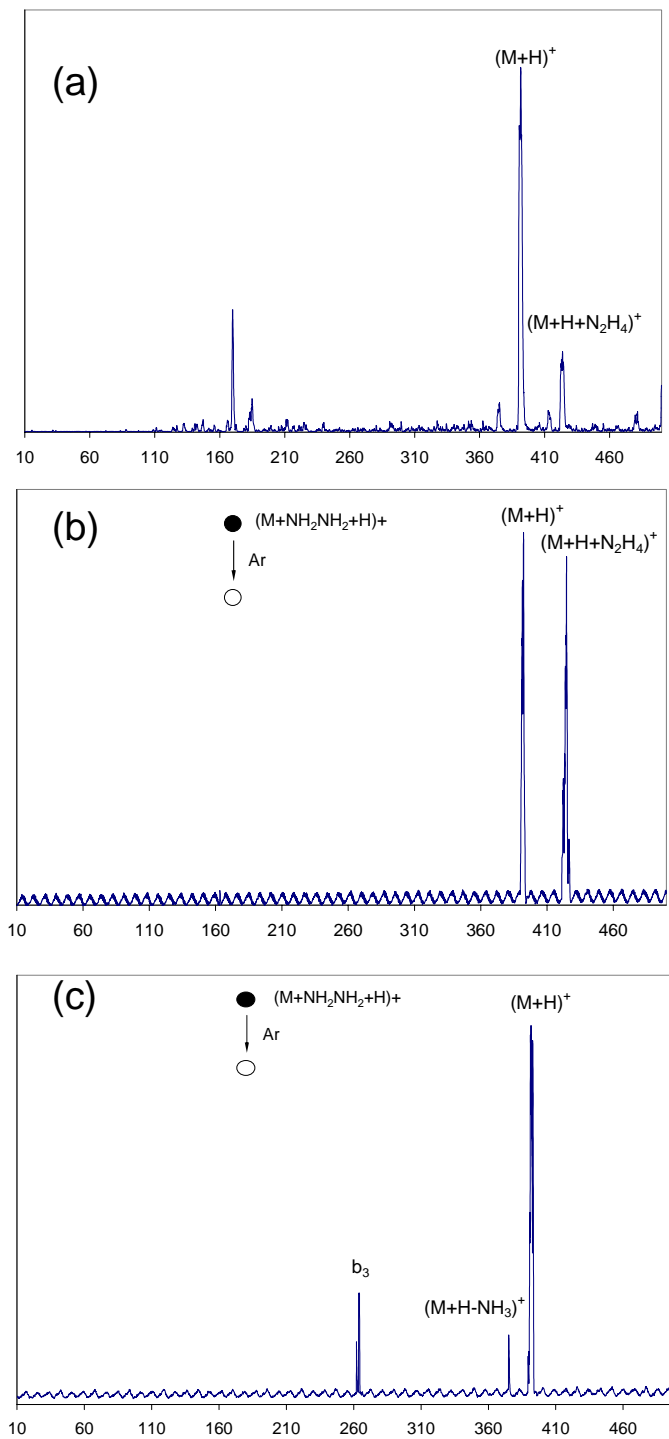
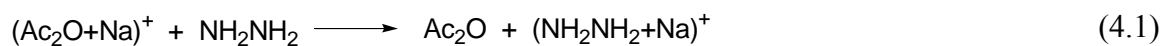


Figure 3.19. (a) Electrospray spectrum of a mixture methanol solution of GGFL-NH₂ with 25% hydrazine. Unlabeled ions are unidentified. (b) Product ion spectrum of Ar CID on the proton-bound heterodimer of GGFL-NH₂ and hydrazine at $\langle KE_{cm} \rangle = 0.4\text{ eV}$. (c) Product ion spectrum of Ar CID on the proton-bound heterodimer of GGFL-NH₂ and hydrazine at $\langle KE_{cm} \rangle = 1.3\text{ eV}$.

3.3.6. MS/MS experiment on Ac₂O with hydrazine

To examine the hydrazine nucleophilic attack on a carbonyl group, MS/MS experiments on sodiated Ac₂O using hydrazine as collision target were performed. A solution of Ac₂O in H₂O/MeOH did not produce any positively charged ions from Ac₂O; only protonated solvent and acetic acid ions are observed (data not shown). However, sodiated Ac₂O is successfully generated from 99% Ac₂O, shown in Figure 3.20(a). The MS/MS experiment at low collision energies yield adducts of sodiated Ac₂O with one and two hydrazine molecules, respectively (Figure 3.20 (b)). At higher collision energies, the abundance of adducts decrease and a sodiated hydrazine is observed (Figure 3.20 (c)), resulting from a sodium cation transfer (eq. 4.1)



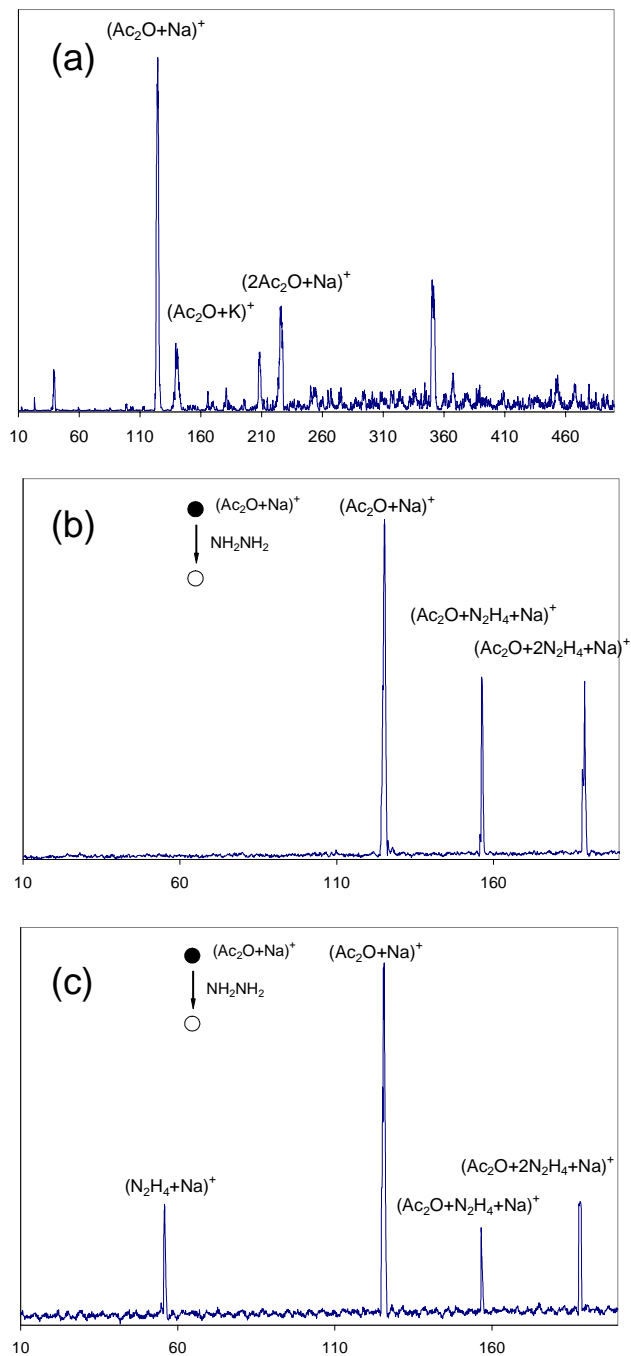


Figure 3.20. (a) Electrospray spectrum of pure Ac_2O liquid. (b) Product ion spectrum of MS/MS experiment on sodiated Ac_2O with NH_2NH_2 as collision gas at $\langle KE_{cm} \rangle = 2.1\text{ eV}$. (c) Product ion spectrum of sodiated Ac_2O with NH_2NH_2 as collision gas at $\langle KE_{cm} \rangle = 3.1\text{ eV}$.

Table 3.3. Summary of product ions observed from MS/MS experiments examined in this study.

Precursor ion	Collision targets	Product ions observed
(Leu-Enk+H) ⁺	Ar	y ₂ , y ₃ , a ₄ , and b ₄
	NH ₃	y ₂ , y ₃ , a ₄ , b ₄
	H ₂ O ₂	y ₂ , y ₃ , a ₄ , b ₄
	NH ₂ NH ₂	y ₂ , y ₃ , a ₄ , b ₄ , adduct (LeuEnk+H+NH ₂ NH ₂) ⁺
(Leu-Enk+Li) ⁺	Ar	b ₄ OLi
	NH ₂ NH ₂	b ₃ OLi, b ₄ OLi, adduct (LeuEnk+Li+NH ₂ NH ₂) ⁺
(Leu-Enk+Na) ⁺	Ar	b ₃ ONa, b ₄ ONa
	NH ₂ NH ₂	b ₃ ONa, b ₄ ONa, adduct (LeuEnk+Na+NH ₂ NH ₂) ⁺
(GGFL-NH ₂ +H) ⁺	Ar	b ₃ , y ₂ , (M+H) ⁺ -CO-NH ₃ , (M+H) ⁺ -NH ₃
	NH ₂ NH ₂	b ₃ , y ₂ , b ₃ +NH ₂ NH ₂ , b ₃ +2NH ₂ NH ₂ , (M+H) ⁺ -CO-NH ₃ , (M+H) ⁺ -NH ₃ , (M+H) ⁺ , ((M+H) ⁺ -CO-NH ₃)+ NH ₂ NH ₂ , ((M+H) ⁺ -NH ₃) ⁺ , (M+H+NH ₂ NH ₂) ⁺
	EDA	b ₃ , b ₃ +EDA, (M+H) ⁺ -CO-NH ₃ , (M+H) ⁺ -NH ₃ , (M+H) ⁺ , ((M+H) ⁺ -CO-NH ₃)+ EDA, ((M+H) ⁺ -NH ₃ + NH ₂ NH ₂), (M+H+EDA) ⁺
(GGFL-NH ₂ +Na) ⁺	Ar	a ₃ +Na, y ₂ +Na
	NH ₂ NH ₂	a ₃ +Na, y ₂ +Na
	EDA	y ₂ +Na, (M+Na-CO-NH ₃) ⁺ , (M+Na+EDA) ⁺
	HCOOH	a ₃ +Na, (M+Na-CO-NH ₃) ⁺ , (M+Na+HCOOH) ⁺
	Ac ₂ O	Y+Na, (M+Na+HCOOH) ⁺
(GGFL-NH ₂ +H+NH ₂ NH ₂) ⁺	Ar	b ₃ , (GGFL-NH ₂ -NH ₃) ⁺ , (GGFL-NH ₂ +H) ⁺ ,
(Ac ₂ O+Na) ⁺	NH ₂ NH ₂	NH ₂ NH ₂ +Na, (Ac ₂ O+Na+ NH ₂ NH ₂) ⁺ , (Ac ₂ O+Na+ 2NH ₂ NH ₂) ⁺

3.4. Discussion

3.4.1. Cleavage mechanism

The proposed mechanism for hydrazine nucleophilic attacking a carbonyl group in a peptide backbone is illustrated in Figure 3.13. The first step is the formation of an adduct between a cationized peptide and a hydrazine molecule. The cleavage starts with the nucleophilic addition by the nitrogen atom in hydrazine to form a tetrahedral intermediate and a hydrogen migration from the hydrazine nitrogen to the amide nitrogen, followed by amide C-N bond breaking to produce a b_n type ion, $(b_n + \text{NHNH}_2)^+$. The attachment of a proton or metal cation on the amide oxygen atom will significantly increase the electrophilic character of the carbonyl carbon. However, the proton in a protonated peptide is known to be mobile [43]. Upon collision activation in the gas-phase, the proton in a protonated peptide can move from more basic sites, including the N-terminal nitrogen and basic side chains, to any heteroatom in the peptide backbone. Compared to a proton, metal cations such as lithium and sodium in a cationized peptide, are less mobile due to multidentate coordination [9, 44, 45]. Thus, the chemical cleavage scheme proposed here may be more likely to proceed with a sodiated or lithiated peptide. Another advantage of avoiding use of a protonated peptide ion is that a good nucleophile is often a strong base, which can deprotonate a protonated peptide via proton transfer. Indeed in the present study, the sodium or lithium transfer is only observed in the MS/MS experiment on Ac_2O with hydrazine as collision gas (Figure 3.20(d)) and are not observed in other sodiated or lithiated peptides.

For a sodiated or lithiated peptide ions, the generation of a special type of fragment resulting from the C-terminal carboxylate cleavage during a CID process has been proposed [44, 46]. As illustrated with a sodiated tripeptide in Figure 3.21, the Na^+ can form an ion pair with the

C-terminal carboxylate; the replaced proton becomes mobile and can reside at any basic site along the backbone or side chains. The Na^+ in the C-terminal carboxylate can polarize the carbonyl group on the adjacent residue. This is followed by a nucleophilic attack by the carboxylate to this neighboring carbonyl, neutral elimination and $b_n\text{-ONa}$ ion generation.

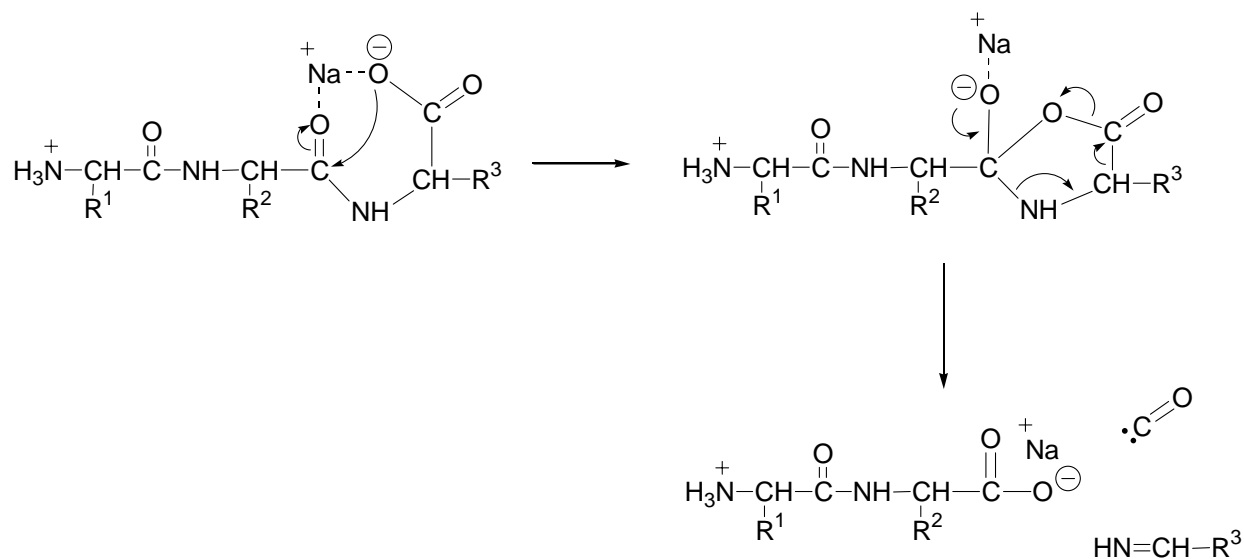


Figure 3.21. Reaction scheme for the fragmentation of a sodiated peptide during the CID process. Figure adapted from [46].

3.4.2. Potential complications

A common observation from the hydrazine CID with protonated LeuEnk and GGFL- NH_2 is the formation of adducts between protonated parent ions and hydrazine at low collision energies. Formation of such adducts between parent peptides and targets forming in a collision cell have been reported by Fesenlau and co-workers in their endothermic ion-molecule reaction studies [28-31]. No specific cleavage product ions, such as those proposed in Figure 3.13 are found at higher collision energies. The mobile proton might prevent the proposed mechanism to proceed. Interestingly enough, ions with m/z values corresponding to $(b_n+\text{NH}_2\text{NH}_2)^+$, which are

the expected product according to the schedule outlined in Figure 3.13, are observed in the GGFL-NH₂ MS/MS experiment using hydrazine as target. However, it could also be the noncovalent complex of b_n ions with a hydrazine resulting from the secondary collision between fragments and hydrazine. O'Hair and co-workers [32] reported the presence of (b_n+BuNH₂)⁺ in their n-butylamine MS/MS study on protonated peptides in an ion trap instrument. By performing MS³ on the (b_n+BuNH₂)⁺ ion they demonstrated that these ions had covalent linkages between b_n and BuNH₂.

The carboxylate cleavage ions, (b_n-ONa)⁺ and (b_n-OLi)⁺ are commonly observed in the Ar and chemical MS/MS experiments on sodiated and lithiated LeuEnk. Clearly, this C-terminal carboxylate nucleophilic attack pathway (Figure 3.21) is competing with the desired specific cleavage pathway. Modification of the C-terminus from a carboxylate to a less nucleophilic functional group such as C-terminal amide might increase the possibility of chemical cleavage. The MS/MS experiments on a sodiated or lithiated GGFL-NH₂ with HCOOH as collision gas is based on the strategy of blocking the C-terminal carboxylate cleavage while introducing a carboxylate group in the collision complex. Similarly, the acetic anhydride was chosen to examine its reactivity toward GGFL-NH₂. The proposed mechanism for HCOOH cleaving a sodiated peptide is shown in Figure 3.22. However, only adducts and normal CID fragments are observed; no specific peptide backbone cleavage products from HCOOH or Ac₂O's carboxylate nucleophilic attack on the backbone carbonyl are observed. A possible reason for the failure of observing any specific cleavage products as expected from Figure 3.22 might not that the reaction may not have enough time to proceed to completion when forming the collision complex in the gas-phase.

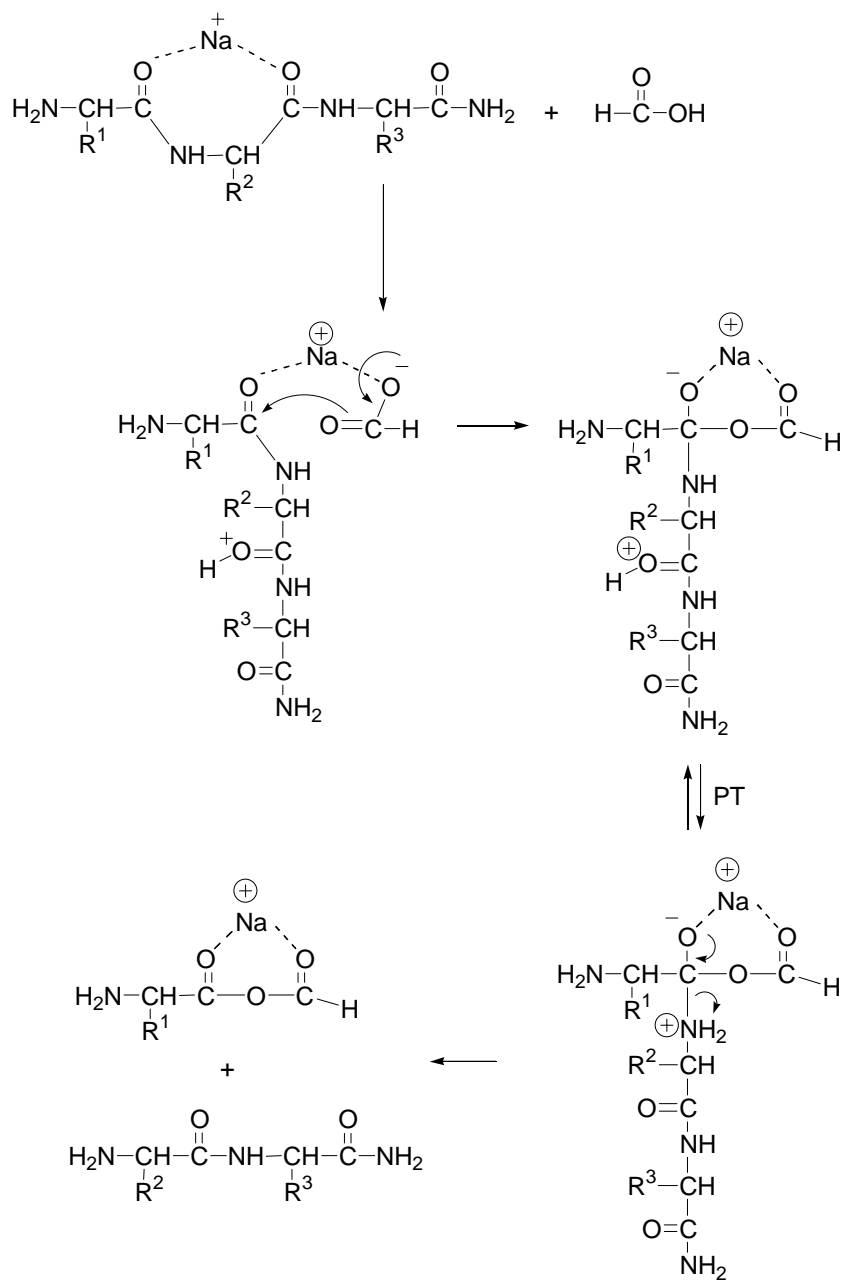


Figure 3.22. Hypothetical mechanism for HCOOH cleaving an amide bond in a sodiated peptide ion.

Another scheme based on essentially the same strategy is to form a noncovalent complex of a peptide and a prospective cleavage reagent in solution, then activate the complex through Ar energetic collision, as shown in Figure 3.19. However, the complex simply dissociates (in accord with the Cooks kinetic method for measuring cation affinity) upon the collision activation. One variable that might limit the success of the schemes and strategies proposed here is that the triple quadrupole, with no trapping capability, might not be the optimal instrument. A typical resident time for an ion in the collision cell is several milliseconds, while a trapping device (e.g., an ion trap), capable of trapping ions from several hundred milliseconds to several seconds, may allow enough time for the reaction to proceed. William et al. [47] has demonstrated that Cheng's method of cleaving deprotonated peptide analog N-methyl acetamide by CF_3COOEt can be successfully carried out in an ion trap equipped with a negative ion chemical ionization source.

3.4.3. Alternative solutions

Conventional CID processes on N- or C-terminal derivatized peptide ions have been demonstrated to produce specific fragmentation patterns. Summerfield et al. [48], for instance, found that the N-terminal phenylthiocarbamoyl (PTC) derivatized peptides enhanced the abundances of b_1 and y_{n-1} ions, as shown in Figure 3.23. Beardsley and Reilly [49] discovered that by acetamidinating (Figure 3.24(a)) the N-terminus of a peptide using S-methyl thioacetimidate the abundance of b_n and y_n ions were enhanced in the product ion spectrum of Ar CID on the protonated peptide ion. The proposed intermediate for y_{n-1} fragment formation is shown in Figure 3.24(b). Wysocki and co-workers [43] demonstrated that residue-specific cleavage was observed in fixed-charge containing N-terminal derivatized peptides.

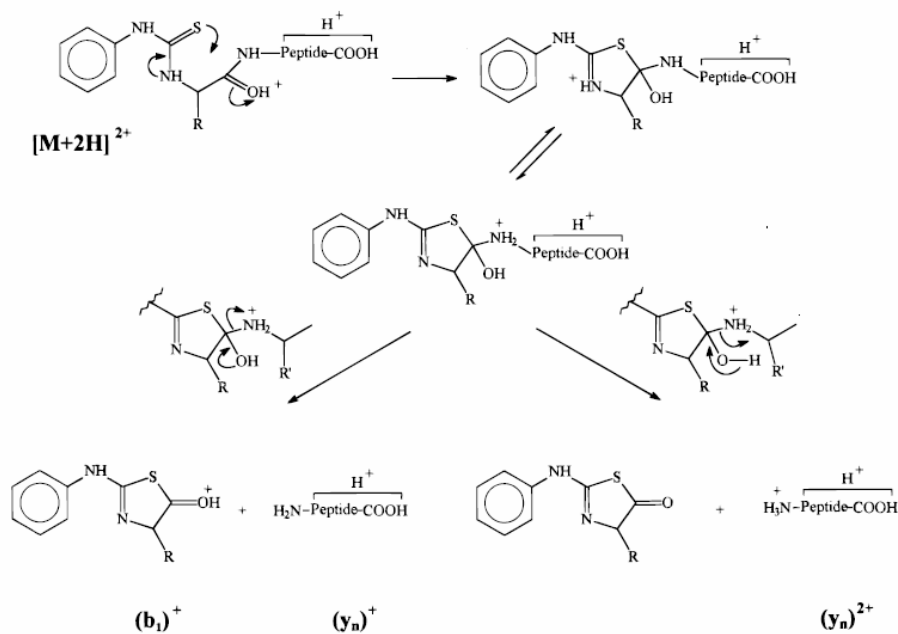


Figure 3.23. Proposed mechanism of production of b_1 and y_n fragments from $[M+2H]^{2+}$ ions of peptide PTC derivatives. Figure taken from [48].

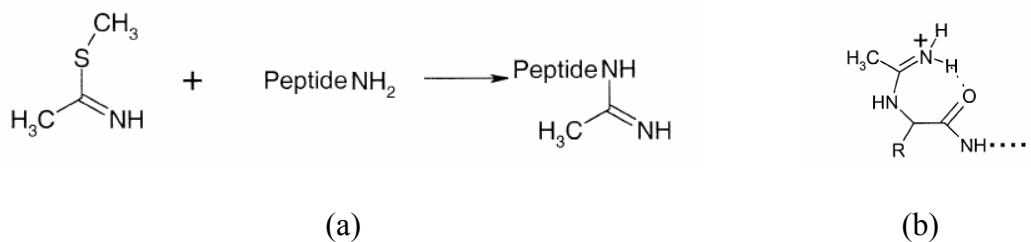


Figure 3.24. (a) Acetamidination reaction of a peptide. (b) Proposed cyclic intermediate leading to y_{n-1} in formation. Figure adapted from [49]

Interestingly enough, O'Hair and Reid [50] illustrated the possibility of performing gas-phase derivatization of some simple protonated peptides with acetone in an ion trap. After a period of trapping time up to 10 s, a noncovalent adduct ion between protonated parent ion and acetone is found; a Schiff's base ion is also observed via dehydration of the parent adduct ion

(Figure 3.25). The Ar CID of the Schiff's base ion shows an enhanced fragmentation pattern of a_n and b_n type ions. Although using gas-phase derivatizations to enhance the CID fragmentation selectivity is not directly relevant to the nucleophile-electrophile type chemical strategy for peptide cleavage, a fast gas-phase derivatization reaction will also greatly simplify the CID product ion spectrum interpretation if the fragment pattern is consistent, regardless the primary structure of peptides.

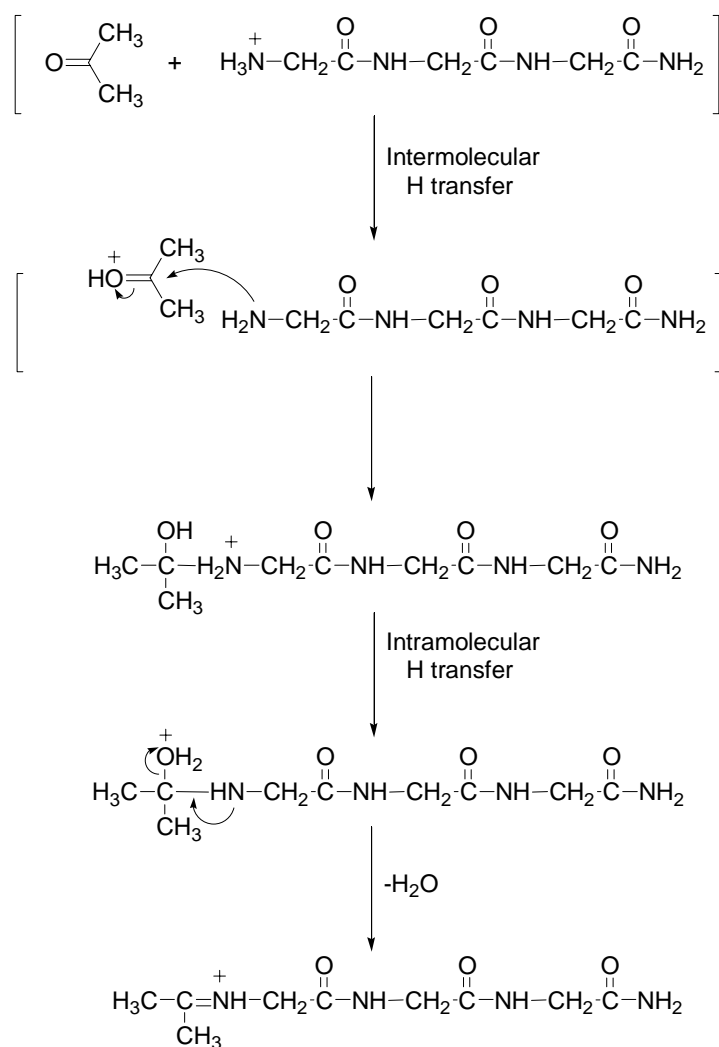
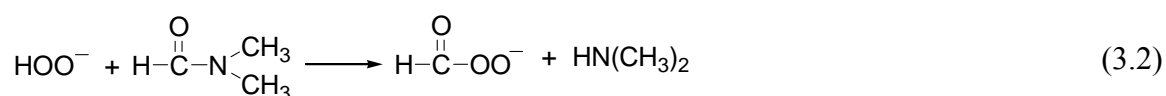


Figure 3.25. Proposed scheme for derivation of protonated peptide via gas-phase ion-molecule reaction of a protonated peptide and acetone.

3.4.4. Negative ion cleavage

Although most of peptide fragmentation data in current MS/MS databases are for positive ions, a reagent that can work with negatively charged ions from electrospray can also provide valuable sequence information as a supplement to conventional positive ion CID. Negatively charged peptide ions generated from electrospray generally have negative charges on carboxylate groups, either on C-termini or acidic residues. HOO^- has been demonstrated to cleave an amide bond in the gas-phase [51], shown in eq. 3.2. Using hydrogen peroxide as the collision gas to generate a HOO^- ion inside the collision complex, formed between HOOH and a negative charge peptide in the gas phase, may yield the N-terminal sequence information, as proposed in Figure 3.26. MS/MS experiments using HOOH as collision gases were attempted on several dipeptides in the same fashion as the positive ion experiment outlined in this study. The same fragment ions were observed from experiments using either HCOOH and Ar as the collision target. Unlike the positive ion mode experiment, no adducts between parent peptide ions and HCOOH were observed. A complication of working in negative ion mode is that negatively charged peptides are difficult to generate from electrospray.



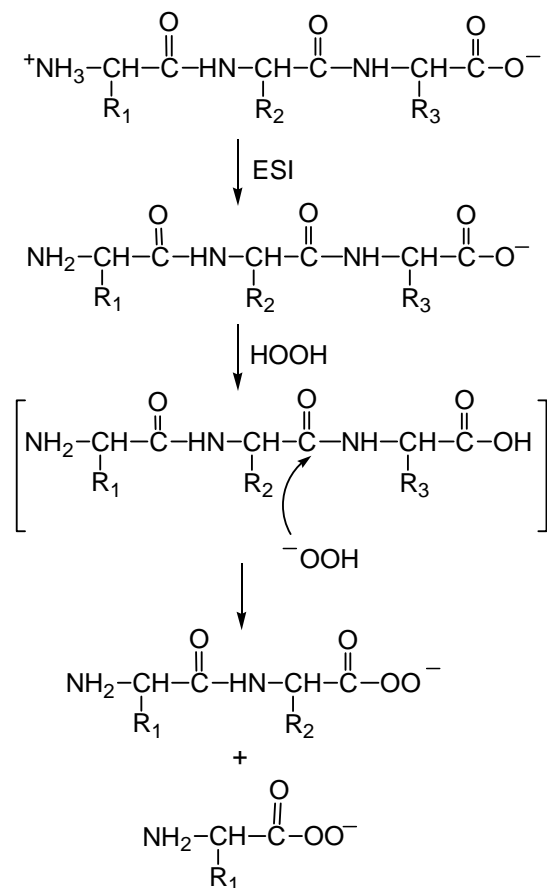


Figure 3.26. Proposed scheme for cleavage of a negatively charged peptide ion by using HOOH as the cleavage reagent.

3.5. Conclusion

The gas-phase ion-molecule reactions between protonated, lithiated, or sodiated peptides and selected reagents have been investigated in the collision chamber of an electrospray ionization triple quadrupole instrument, at various collision energies. The adduct ions between the parent peptide ions and neutral reagents are commonly observed at low collision energies. At higher collision energies, non-selective fragment ions are produced along with adducts of these fragment ions and one or two neutral reagents. An collisional activation on non-covalent complexes generated from ESI of peptide and chemical reagent mixtures were also attempted.

However, no specific cleavage product from the chemical reaction was observed. A trapping device that is capable of retaining ions to prolong the ion-molecule reaction time might be more appropriate for such studies. The peptide bond cleavage via ion-molecule reaction from negatively charged ions may achieve better selectivity.

3.6. References

- [1] D.F. Hunt, J.R. Yates, J. Shabanowitz, S. Winston, and C.R. Hauer, *Proc. Natl. Acad. Sci.* 83 (1986) 6233-6237.
- [2] K. Biemann, *Anal. Chem.* 58 (1986) 1288A-1300A.
- [3] K. Biemann and H.A. Scoble, *Science* 237 (1987) 992-998.
- [4] P. Roepstorff and J. Fohlman, *J. Biol. Mass Spectrom.* 11 (1994) 601.
- [5] M. Kinter and N.E. Sherman, *Protein Identification by Database Searching*, in: (Eds.), *Protein Sequencing and Identification Using Tandem Mass Spectrometry*, John Wiley & Sons, Inc New York, 2000.
- [6] R.J. Simpson, L.M. Connolly, J.S. Eddes, J.J. Pereira, R.L. Moritz, and G.E. Reid, *Electrophoresis* 21 (2000) 1707-1732.
- [7] M. Kinter and N.E. Sherman, *Collisional Induced Dissociation of Protonated Peptide Ions and the Interpretation of Product Ion Spectra*, in: (Eds.), *Protein Sequencing and Identification Using Tandem Mass Spectrometry*, John Wiley & Sons, Inc New York, 2000.
- [8] G. Tsaprailis, A. Somogyi, E.N. Nikolaev, and V.H. Wysocki, *Int. J. Mass Spectrom.* 195/196 (2000) 467-479.
- [9] M.M. Kish and C. Wesdemiotis, *Int. J. Mass Spectrom.* 227 (2003) 191-203.
- [10] R.B. Cody and B.S. Freiser, *Anal. Chem.* 59 (1987) 1054-1056.
- [11] B. Wang and F.W. McLafferty, *Org. Mass Spectrom.* 25 (1990) 554-556.
- [12] N.A. Kruger, R.A. Zubarev, B.K. Carpenter, N.L. Kelleher, D.M. Horn, and F.W. McLafferty, *Int. J. Mass Spectrom.* 182/183 (1999) 1-5.
- [13] R.A. Zubarev, N.L. Kelleher, and F.W. McLafferty, *J. Am. Chem. Soc.* 120 (1998) 3265-3266.

- [14] N.L. Kelleher, *Anal. Chem.* (2004) 197A-203A.
- [15] J.E.P. Syka, J.J. Coon, M.J. Schroeder, J. Shabanowitz, and D.F. Hunt, *Proc. Natl. Acad. Sci.* 101 (2004) 9528-9533.
- [16] J.J. Coon, J.E.P. Syka, J.C. Schwartz, J. Shabanowitz, and D.F. Hunt, *Int. J. Mass Spectrom.* 236 (2004) 33-42.
- [17] E.R. William, J.J.P. Furlong, and F.W. McLafferty, *J. Am. Soc. Mass Spectrom.* 1 (1990) 288-294.
- [18] C.B. Lebrilla, D.T.S. Wang, T.J. Mizoguchi, and R.T.J. McIver, *J. Am. Chem. Soc.* 111 (1989) 8593-8598.
- [19] D.P. Little, J.P. Speir, M.W. Senko, P.B. O'Connor, and F.W. McLafferty, *Anal. Chem.* 66 (1994).
- [20] R.A. Jockusch, K. Paech, and E.R. William, *J. Phys. Chem. A* 104 (2000) 3188-3196.
- [21] M.D.A. Mabud, M.J. Dekery, and C.R. G., *Int. J. Mass Spectrom. Ion Processes* 67 (1985) 285-294.
- [22] S.J. Pachuta, H.J. Kenttamaa, T.M. Sack, R.L. Cerny, K.B. Tomer, M.L. Gross, R.R. Pachuta, and R.J. Cooks, *J. Am. Chem. Soc.* 110 (1988) 657-665.
- [23] C.F. James and C.L. Wilkins, *Anal. Chem.* 62 (1990) 1295-1299.
- [24] E.R. William, K.D. Henry, F.W. McLafferty, J. Shabanowitz, and D.F. Hunt, *J. Am. Soc. Mass Spectrom.* 1 (1990).
- [25] R.A. O'Hair, *J. Mass Spectrom.* 35 (2000) 1377-1381.
- [26] M.A. Freitas, R.A. O'Hair, S. Dua, and J.H. Bowie, *Chem. Commun.* 15 (1997) 1409-1410.
- [27] M.A. Freitas and R.A. O'Hair, *Int. J. Mass Spectrom. Ion Processes* 175 (1998) 107-122.
- [28] R. Orlando, C. Fenselau, and R.J. Cotter, *Org. Mass Spectrom.* 4 (1990) 259-262.
- [29] R. Orlando, C. Fenselau, and R.J. Cotter, *Anal. Chem.* 62 (1990) 2388-2390.
- [30] R. Orlando, C. Fenselau, and R.J. Cotter, *J. Am. Soc. Mass Spectrom.* 2 (1991) 189-197.
- [31] X. Cheng and C. Fenselau, *J. Am. Chem. Soc.* 115 (1993) 10327-10333.
- [32] R.A. O'Hair, N.K. Androustopoulos, and G.E. Reid, *Rapid Commun. Mass Spectrom.* 14 (2000) 1707-1716.

- [33] X. Cheng and J.J. Grabowski. *Designing A Reagent to Cleave Carbonyl-Nitrogen Bonds in Peptides in an Anion-Molecule reaction*. in *Proceeding of the 39th ASMS Conference on Mass Spectrometry and Allied Topics*. 1991. Nashville, TN.
- [34] S.J. Leach, *Pure Appl. Chem.* 3 (1953) 25-60.
- [35] J.R. Benson, P.C. Louie, and R.A. Bradshaw, in: E. Gloss and J. Meienhofer (Eds.), *The Peptide; Analysis, Synthesis, Biology*, Academic New York, 1981, pp. 243-245.
- [36] R.L. Hill, in: C.B. Anfinsen, et al. (Eds.), *Advances in Protein Chem.*, Academic New York, 1965, pp. 37-108.
- [37] X. Cheng and J.J. Grabowski, Unpublished results.
- [38] N.J. Fina and J.O. Edwards, *Int. J. Chem. Kinetics* V (1973) 1-26.
- [39] A.P. Grekov and V.Y. Veselow, *Russian Chem. Rev.* 47 (1978) 631-648.
- [40] A. Ozdemir, *Structure Studies of Peptides by UV Resonance Raman and Mass Spectrometry*, in *Department of Chemistry*. 2002, University of Pittsburgh: Pittsburgh.
- [41] NIST Standard Reference Database Number 69 - March 2003 Release.
- [42] J.C. Schwartz, A.P. Wade, C.G. Enke, and R.J. Cooks, *Anal. Chem.* 62 (1990) 1809-1818.
- [43] V.H. Wysocki, G. Tsaprailis, L.L. Simth, and L.A. Breci, *J. Mass Spectrom.* 35 (2000) 1399-1406.
- [44] X. Tang, W. Ens, K.G. Standing, and J.B. Westmore, *Anal. Chem.* 60 (1988) 1791-1799.
- [45] J.M. Barr and M.J.V. Stipdonk, *Rapid Commun. Mass Spectrom.* 16 (2002) 566-578.
- [46] S.W. Lee, H.S. Kim, and J.L. Beauchamp, *J. Am. Chem. Soc.* 120 (1998) 3188-3195.
- [47] T.L. William, J.L. Stephenson, and R.A. Yost. *Chemical reactions vs. CID to cleave amide bonds*. in *The 43rd ASMS Conference on Mass Spectrometry and Allied Topics*. 1995. Atlanta, GA.
- [48] S.G. Summerfield, M.S. Bolar, and S.J. Gaskell, *J. Mass Spectrom.* 32 (1997) 225-231.
- [49] R. Beardsley and J.P. Reilly, *J. Am. Soc. Mass Spectrom.* 15 (2004) 158-167.
- [50] R.A. O'Hair and G.E. Reid, *J. Am. Soc. Mass Spectrom.* 11 (2000) 244-256.
- [51] C.H. DePuy, J.J. Grabowski, V.M. Bierbaum, S. Ingemann, and N.M.M. Nibbering, *J. Am. Chem. Soc.* 107 (1985) 1093-1098.

Chapter 4 Leucine-Enkephalin and Methionine-Enkephalin Proton Affinity Measurement via the Extended Kinetic Method

4.1. Introduction

Leucine-enkephalin (LeuEnk, YGGFL) and methionine-enkephalin (MetEnk, YGGFM) are two important neuropeptides that often present simultaneously in brains [1]. Electrospray mass spectrometry in conjunction with HPLC has been used for the quantitation of these two neuropeptides in vivo [2-4]. Proton affinity (PA), one of the fundamental thermochemical properties of a molecule, plays an important role in determining the ionization efficiency of a molecule during an electrospray processes; the electrospray response of a molecule with a lower proton affinity can be suppressed by a molecule with a higher proton affinity [5]. Despite the significance of proton affinities on the understanding of gas-phase ionization behaviors of molecules, no systematic study of the proton affinities of LeuEnk and MetEnk has been reported. The proton affinity of a neutral molecule can be obtained by equilibrium [6, 7], bracketing [8] or kinetic method [9, 10]. The equilibrium method derives the gas-phase basicity difference between two molecules through measurement of the equilibrium constant of the proton transfer reaction between a protonated ion and a neutral in the gas-phase. The bracketing method allows a protonated molecule to react with a series of references to establish the value of the proton affinity of the molecule being examined based on the assumption that endothermic proton transfer can not occur.

The kinetic method, developed by Cooks and co-workers [9, 10], can derive the thermochemical properties of a molecule, such as proton, metal ion and electron affinities, from the relative dissociation rate coefficients of a weakly bound complex ion. Compared to these two methods, the kinetic method is relatively simple and sensitive and can be used to study non-

volatile biological molecules. Shown in eq. 4.1, a proton-bound dimer between two neutral molecules B_1 and B_2 has two competitive dissociation channels leading to two protonated product ions B_1H^+ and B_2H^+ . The abundances of the product ions resulting from these two dissociation channels are proportional to the rate coefficients of each channel (k_1 and k_2), which can be expressed using unimolecular reaction theory (eq. 4.2) [11].



$$k = \frac{RT}{h} \frac{Q^*}{Q} \exp\left(-\frac{\varepsilon_0}{RT}\right) \quad (4.2)$$

$$\ln \frac{[B_1H^+]}{[B_2H^+]} = \ln \frac{k_1}{k_2} = \ln \frac{Q_1^*}{Q_2^*} + \frac{\varepsilon_{02} - \varepsilon_{01}}{RT_{eff}} \quad (4.3)$$

The natural logarithm of the product ion intensity ratio can be expressed by eq. 4.3, where Q_1^* and Q_2^* are the partition functions of the activated complexes that forms $B_1H^+ + B_2$ and $B_2H^+ + B_1$ respectively, ε_{01} and ε_{02} are the activation energies of the individual dissociation channels, and T_{eff} is the effective temperature of the activated complex ion. Assuming that no reverse barrier exists [12], the activation energy difference between the two reaction channels can be replaced by the proton affinity difference between the two molecules (eq. 4.4).

$$\ln \frac{[B_1H^+]}{[B_2H^+]} = \ln \frac{Q_1^*}{Q_2^*} + \frac{PA(B_2) - PA(B_1)}{RT_{eff}} \quad (4.4)$$

For two structurally and chemically similar molecules, a second assumption, that $Q_1^* = Q_2^*$, can be applied. Thus $\ln Q_1^*/Q_2^* = 0$ and the proton affinity difference of these two molecules can be expressed as the natural logarithm of the product ions abundance ratio (eq. 4.5).

$$\ln \frac{[B_1H^+]}{[B_2H^+]} = \frac{PA(B_2) - PA(B_1)}{RT_{eff}} \quad (4.5)$$

However, for a structurally complicated biomolecule, it is difficult to find a reference base with similar structure and having a known proton affinity, which has a proton affinity close to the one to be measured. To circumvent this problem, Cheng et al. [13] developed a method to measure the proton affinity of peptides using a series of compounds that are structurally similar among themselves but dissimilar to the peptides studied as references. Based on the assumption that $\ln(Q_1^*/Q_2^*)$ is likely to be constant for each such peptide-reference pair, the plot of $\ln([B_1H^+]/[B_2H^+])$ versus the proton affinity of reference $PA(B_2)$ yields a linear correlation with a slope of $-1/RT_{eff}$ and a y-intercept $[\ln(Q_1^*/Q_2^*) + PA(B_1)/RT_{eff}]$ of as shown in eq. 4.6.

$$\ln \frac{[B_1H^+]}{[B_2H^+]} = \left\{ \ln \frac{Q_1^*}{Q_2^*} + \frac{PA(B_1)}{RT_{eff}} \right\} - \frac{PA(B_2)}{RT_{eff}} \quad (4.6)$$

Let $y' = [\ln(Q_1^*/Q_2^*) + PA(B_1)/RT_{eff}]$. Perform the experiments at several T_{eff} (by changing collision energy), thus different y' can be obtained. Next a second plot of y' versus $1/RT_{eff}$, another linear correlation with a slope of $PA(B_1)$, which is the proton affinity of the unknown molecule, can be obtained. Using the procedure described above, proton affinities of several small peptides have been determined. For instance, Wu and Fenselau measured proton affinities of a series of polyglycines (from monoglycine to decaglycine) using FAB-MS derived-data [14]. They also used this strategy to measure the proton affinities of lysine, histidine and several tripeptides containing a lysine or histidine residue [15]. Proton affinity of lysine and histidine containing di- and tripeptides were also examined by Carr and Cassady [16]. The same strategy has employed by the Wedemiotis and the Gronert groups to measure the proton affinity [17], sodium affinity and lithium affinity [18-20] of selected peptides.

One surprising feature in these peptide affinity measurements is that a unity correlation ($R^2=1$) is obtained from the $[\ln(Q_1^*/Q_2^*) + PA(B_1)/RT_{eff}]$ vs. $1/RT_{eff}$ plot. Armentrout [21] points out that, in Fenselau's method, the $[\ln(Q_1^*/Q_2^*) + PA(B_1)/RT_{eff}]$ and $1/RT_{eff}$ are not independent due to the covariance between the slope and y-intercept originated from the isokinetic effect [22-24]. Armentrout argues that examining the entropy effect by the method initially described by Fenselau and Wedemiotis is not necessarily valid. Instead, Armentrout recommends a procedure to remove the covariance in order to examine the entropy effect more rigorously by plotting $\ln[BH^+]/[B_{ref}H^+]$ as a function of $PA(B_{ref})-PA(avg)$, where $PA(avg)$ is the average proton affinity of all reference compounds employed, as shown in eq. 4.7.

$$\ln \frac{[BH^+]}{[B_{ref}H^+]} = \{PA(apparent) - PA(avg)\} / RT_{eff} - \frac{PA(B_{ref}) - PA(avg)}{RT_{eff}} \quad (4.7)$$

The slope of such a plot is $-1/RT_{eff}$, but the y-intercept will be $[PA(apparent)-PA(avg)]/RT_{eff}$, which can be further expanded to $[PA(B)-PA(avg)]/RT_{eff}-\Delta(\Delta S)/R$, where $\Delta(\Delta S)$ is the entropy difference between the two dissociation channels. Let $y'' = [PA(B)-PA(avg)]/RT_{eff}-\Delta(\Delta S)/R$. Perform the experiments at several T_{eff} (by changing collision energy), thus different y'' can be obtained. Next a second plot of y'' versus $1/RT_{eff}$, another linear correlation with a slope of $PA(B)-PA(avg)$, which is the proton affinity difference of the unknown molecule and the $PA(avg)$, and a y-intercept of $-\Delta(\Delta S)/R$ can be obtained. This method, known as the extended kinetic method, has been adopted for the measurement of proton affinities of amino acids [25] and nucleic acids [26] and will be employed in the present study to measure the proton affinity of LeuEnk and MetEnk. The proton affinities of the examined molecule derived from the Fenselau's method and from the kinetic method are identical. However, the extended kinetic method provides a means to evaluate the validity of the constant entropy assumption more accurately.

4.2. Experimental

The relative proton affinities of LeuEnk and MetEnk were measured by performing collision induced dissociation (CID) on the proton-bound heterodimer of LeuEnk and MetEnk. The absolute proton affinities were measured by performing CID on the proton-bound dimers of LeuEnk or MetEnk with triethylamine (TEA), tripropylamine (TPA) or tributylamine (TBA). For each CID experiment, two instruments, an ESI-triple quadrupole mass spectrometer (TQMS) and an ESI quadrupole-time-of-flight mass spectrometer (Q-TOF) were used. For all quantitative proton affinity measurements performed either on the TQMS or the Q-TOF, experiments were repeated at least twice on different experimental days. LeuEnk, MetEnk and other peptides were obtained from Bachem Americas (King of Prussia, PA). TEA, TPA, TBA and other chemicals were purchased from common commercial chemical suppliers. All reagents were used without further purification. A solution containing 250 μ M LeuEnk and MetEnk each, in 49.5:49.5:1 (V%) methanol/H₂O/acetic acid was used for the LeuEnk MetEnk relative proton affinity measurement. A solution of 250 μ M LeuEnk or MetEnk and 1 μ l/ml TEA or TPA or TBA in 49.5:49.5:1 (V%) methanol/H₂O/acetic acid solution was used for the absolute proton affinity measurement.

The ESI-TQMS used in this study is a custom-built instrument and has been described in detail in Chapter 3. The typical operation conditions to generate the proton-bound dimers needed in this study is are: 2.5 kV spray voltage, 150 °C desolvation temperature, 70 V on the heated capillary, 50 V on the skimmer-1 and 35 V on the skimmer-2. The typical TQMS experimental procedure for the kinetic method measurement in this study is as follows. A proton-bound heterodimer is generated by the electrospray ionization of a solution containing both analytes. Then, the desired ion is mass selected by Q₁ and focused into the octopole collision chamber

where it is allowed to undergo collision induced dissociation while the product ion spectrum is recorded by scanning Q₃. The collision energy is changed by varying the Q₂ pole bias offset. Ar and He are used as collision gases. Data acquisition and processing are performed by Merlin software (Version 1.0.15). The pressure in the collision chamber is monitored by an ion gauge located in the inlet of the turbo pump with a typical reading of $(1.0-3.0) \times 10^{-5}$ Torr at a CID experiment. Product ion abundances are obtained by averaging spectra collected over a 3-minute acquisition.

The ESI-Q-TOF experiments are performed on an orthogonal quadrupole/time-of-flight mass spectrometer (Q-TOF-API-US, Micromass, Manchester, UK), equipped with a Z-spray electrospray source. The typical instrument operation parameters for the source region for this study are a capillary voltage of 3.5 kV, cone voltage of 25 V, source temperature of 80°C, desolvation temperature of 150°C, cone gas flow of 60 l/hr and desolvation gas flow of 600 l/hr. The cone voltage is kept as low as possible to minimize collision induced dissociation in the source region and to maximize the abundance of the proton-bound dimer ion. The solution to be analyzed is infused into the instrument via the embedded syringe pump at a flow rate of 10 μ l/min. The instrument is operated with a full width half maximum (FWHM) resolution of around 10000 and the spectra were accumulated at an acquisition rate of 1s/scan. Data acquisition and processing are performed by MassLynx V4.0 software package. The typical Q-TOF experimental procedure for the measurements in this study is as follows: a proton-bound heterodimer is generated by electrospray ionization and is then mass selected by the quadrupole and subjected to Ar-induced dissociation in the octopole collision chamber with a pressure of 3×10^{-5} Torr. The product ions are analyzed by the TOF MS and the abundance of product ions are obtained from a summation of 200 scans.

4.3. Results

4.3.1. Relative proton affinity measurement

An electrospray spectrum from the mixture of LeuEnk and MetEnk solution obtained from a TQMS experiment is shown in Figure 4.1. In addition to the observation of a protonated LeuEnk (m/z 556) and a protonated MetEnk (m/z 574), a proton-bound homodimer of two LeuEnk (m/z 1111), a homodimer of two MetEnk (m/z 1147) and a proton-bound heterodimer of LeuEnk and MetEnk (m/z 1129) are observed. A CID experiment on the heterodimer produces both protonated LeuEnk and protonated MetEnk, with the latter having a higher intensity (Figure 4.2). The intensity of both LeuEnk and MetEnk increase as the collision energy is raised until $\langle KE_{CM} \rangle = 0.9$ eV as shown in Figure 4.3. Further increases in the collision energy will eventually lead to observation of fragment ions produced from peptide covalent bonds breaking in the peptide ions and thus decrease the intensities of both LeuEnk and MetEnk. The intensity ratio of protonated MetEnk to protonated LeuEnk does not change within the collision energy range examined, as shown in Figure 4.4. Since LeuEnk and MetEnk are both pentapeptides and their sequences are only different in the fifth residue, they can be considered as two structurally similar molecules and thus eq. 4.5 can be applied. Take the average of the natural logarithm of the intensity ratios from Figure 4.4, 0.18, and adopt the effective temperature $T_{eff} = 250$ K (see Discussion 4.4.3), thus the relative proton affinity of MetEnk is 0.1 kcal/mol higher than LeuEnk and MetEnk.

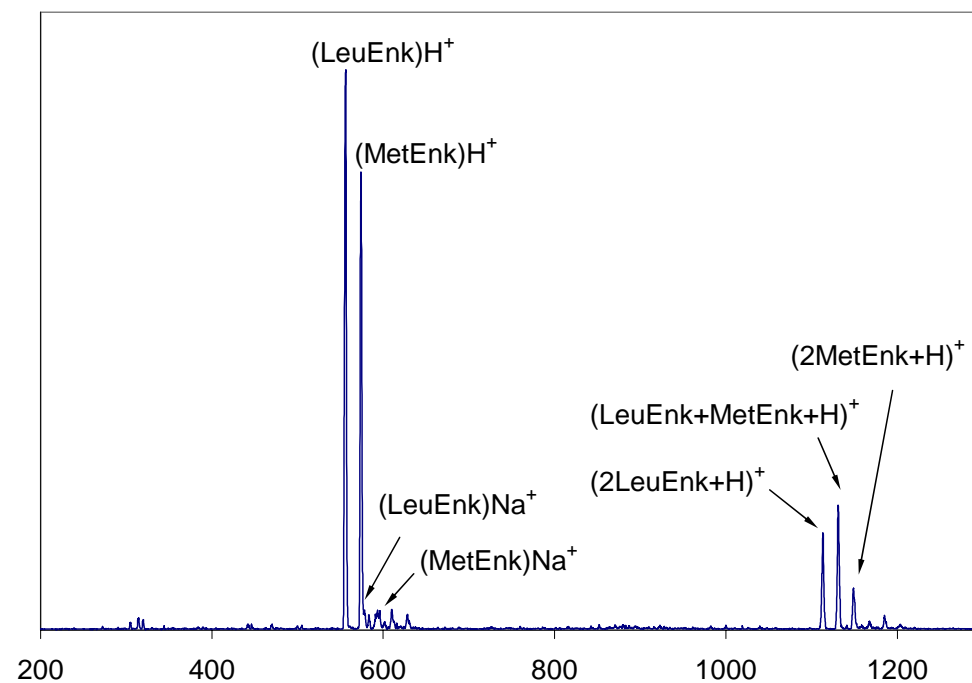


Figure 4.1. ESI of a mixture solution containing 500 μM LeuEnk and MetEnk each obtained from the TQMS; the spray conditions are 0.1 $\mu\text{l}/\text{min}$ flow rate and 2.5 kV spray voltage.

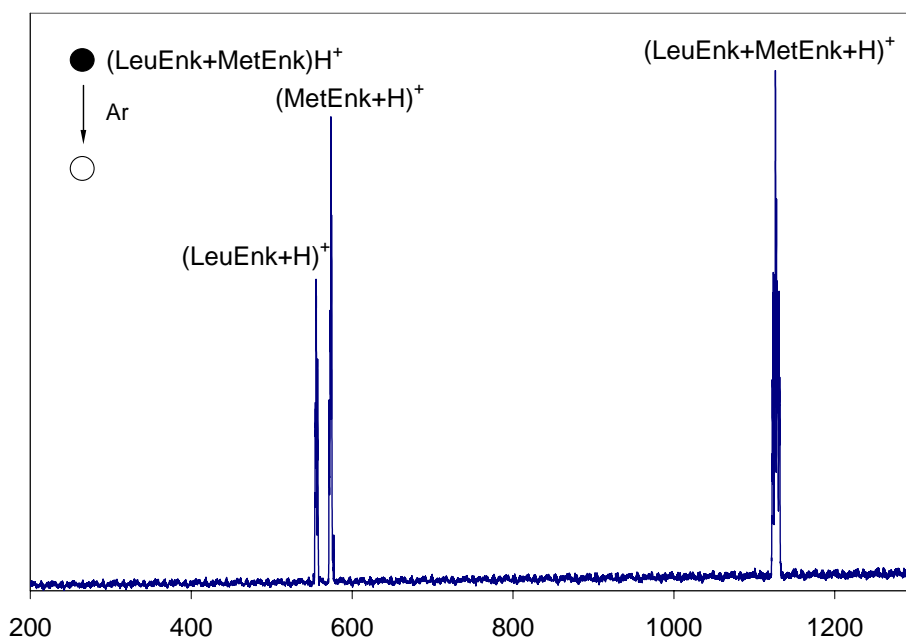


Figure 4.2. A representative product ion spectrum of CID on the proton-bound dimer of LeuEnk and MetEnk obtained from the TQMS; $\langle \text{KE}_{\text{CM}} \rangle = 0.50$ eV.

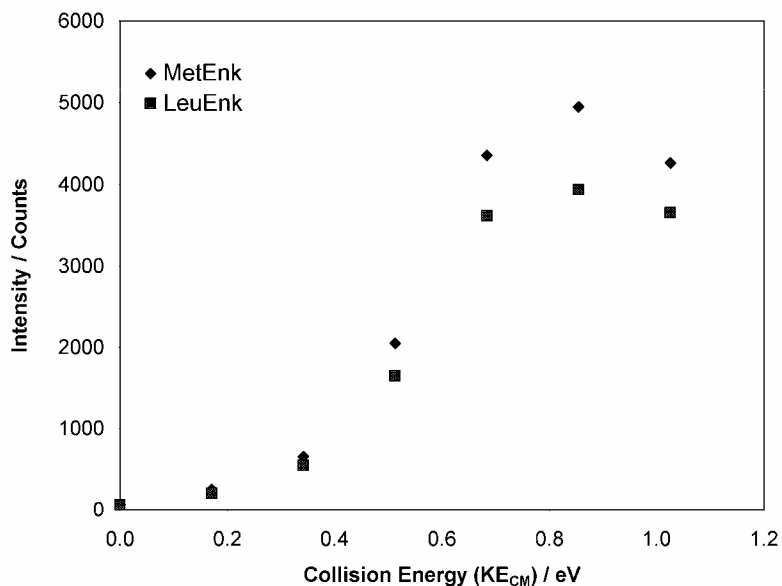


Figure 4.3. The intensities of protonated MetEnk and protonated LeuEnk resulting from CID on the proton-bound heterodimer ion as a function of collision energy; the experiment was performed on the Q-TOF.

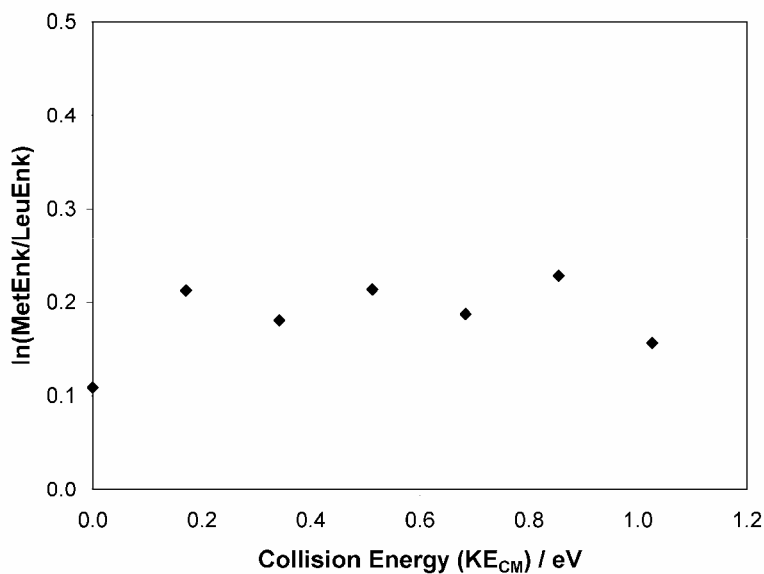


Figure 4.4. The intensity ratio of protonated MetEnk to protonated LeuEnk resulting from CID on the proton-bound heterodimer ion as a function of collision energy; the experiment was performed on the Q-TOF.

4.3.2 Absolute proton affinity measurement using ESI-TQMS

The absolute proton affinity of LeuEnk and MetEnk are measured from the measurement against pentaglycine, which is also a pentapeptide. The CID experiment on the proton-bound heterodimer of LeuEnk and pentaglycine ($\text{LeuEnk}+\text{G}_5\text{H}^+$), generated from the electrospray of a LeuEnk/pentaglycine mixture solution, produces both proton LeuEnk and protonated pentaglycine, as shown in Figure 4.5(a) and (c). Similarly, both protonated MetEnk and protonated pentaglycine are observed from the CID on the proton-bound heterodimer of LeuEnk and pentaglycine ($\text{MetEnk}+\text{G}_5\text{H}^+$), as shown in Figure 4.5(b) and (d). Based on the known proton affinity of pentaglycine ($\text{PA}(\text{G}_5) = 231.8 \pm 0.7 \text{ kcal/mol}$ [14]) and the ratio of protonated enkephalin and product glycine in the product ion spectra, the proton affinity of LeuEnk and MetEnk are located in the range of 235-240 kcal/mol.

Based on the estimation of LeuEnk and MetEnk proton affinity from the pentaglycine experiments, three trialkylamines with proton affinities in the range of 230-240 kcal/mol - triethylamine (TEA, $\text{PA} = 234.7 \text{ kcal/mol}$), tripropylamine (TPA, $\text{PA} = 236.9 \text{ kcal/mol}$) and tributylamine (TBA, $\text{PA} = 238.6 \text{ kcal/mol}$) - were chosen as references to measure the absolute proton affinities of LeuEnk and MetEnk. The commonly observed ions from the electrospray of LeuEnk or MetEnk and trialkylamines mixture solutions include the protonated LeuEnk, protonated trialkylamines and heterodimer between LeuEnk or MetEnk and a trialkylamine. These heterodimer ions are mass selected and subjected to CID at various collision energies.

A set of representative ion spectra obtained from CID on the proton-bound dimer of LeuEnk and either TEA, TPA or TBA collected at the same collision energy, are shown in Figure 4.6(a-c), respectively. The product ions observed from these experiments are protonated LeuEnk and protonated trialkylamines; no additional fragments from protonated LeuEnk or from

protonated trialkylamines are observed under these conditions. As the proton affinity of the trialkylamine reference increases, the intensity ratio of protonated LeuEnk to protonated trialkylamine decreases, as shown in Figure 4.6 from (a) to (c). For each LeuEnk-trialkylamine pair, the CID experiments are carried out at three different collision energies, for which, it is observed that the ion intensity ratios vary as the collision energy changes. For each collision energy, the natural logarithm of the product ion intensity ratio of protonated LeuEnk to trialkylamine $\ln(\text{LeuEnk}/\text{Amine})$ is plotted against $(\text{PA}(\text{amine})-\text{PA}(\text{avg}))$, where $\text{PA}(\text{avg})=236.7$ kcal/mol is the average proton affinity of TEA, TPA and TBA. A linear regression is performed on the three data points obtained from the three trialkylamine references which defines a slope $-1/RT_{\text{eff}}$, shown in Figure 4.7(a). The intensity ratios obtained at three collision energies yield three linear regression lines; the three pairs of slopes and y-intercepts are summarized in Table 4.1. The apparent gas-phase basicities (GB^{app}) are derived by dividing the y-intercepts by the corresponding slopes, shown in Table 4.1. Apply eq. 4.6, take the y-intercepts in Table 4.1, plot them against corresponding $1/RT_{\text{eff}}$ (negative of the slope in Table 4.1), and perform another linear regression, shown in Figure 4.7(b). The slope (2.88) obtained from the linear regression in Figure 4.7 (b) is the proton affinity difference between LeuEnk and three references' average proton affinity, $\text{PA}(\text{LeuEnk})-\text{PA}(\text{avg})$, with units of kcal/mol. The y-intercept (-2.50) is $\Delta(\Delta S)/R$, where $\Delta(\Delta S)$ is the average entropy difference of two dissociation channels (leading to protonated LeuEnk and protonated trialkylamine) and R is molar gas constant. Thus, the proton affinity of LeuEnk measured from this set of experiments is 239.4 kcal/mol and the average entropy difference $\Delta(\Delta S)$ is -4.98 cal/mol K.

Similarly, the absolute proton affinity of MetEnk is measured by performing CID on the proton-bound dimer of MetEnk and TEA, TPA or TPA at various collision energies. The natural

logarithm of the intensity ratio of protonated MetEnk to proton trialkylamine, at three collision energies, from one set of experiments are plotted in Figure 4.8(a). The slopes and y-intercepts from the best fit lines to the data in Figure 4.8 (a) are summarized in Table 4.2 and from which effective temperatures and apparent gas-phase basicities are derived. The slopes derived from the data in Figure 4.8 (a) are plotted against $1/RT_{\text{eff}}$ is shown in Figure 4.8(b). The slope (1.71) obtained from the linear regression in Figure 4.8(b) is the proton affinity difference between MetEnk and three references' average proton affinity, $PA(\text{LeuEnk})-PA(\text{avg})$, with units of kcal/mol. The y-intercept (-2.13) is $\Delta(\Delta S)/R$, where $\Delta(\Delta S)$ is the average entropy difference of two dissociation channels (leading to protonated MetEnk and protonated trialkylamine) and R is molar gas constant. Thus, the proton affinity of LeuEnk measured from this set of experiments is 238.5 kcal/mol and the average entropy difference $\Delta(\Delta S)$ is -4.24 cal/mol K.

The results of the absolute proton affinity measurements of LeuEnk and MetEnk performed in the triple quadrupole instrument using Ar as collision gas are summarized in Table 4.3. The slopes and y-intercepts from the plots of $[PA(\text{app})-PA(\text{avg})]/RT_{\text{eff}}$ vs. $1/RT$, proton affinity and $\Delta(\Delta S)$ derived from each set of experiment and are listed in Table 4.3.

The results for the absolute proton affinity of LeuEnk and MetEnk obtained using TEA, TPA and TBA as reference bases and performed in either the TQMS using Ar or He as collision gases and in the Q-TOF instrument using Ar as collision gas, are summarized in Table 4.4. The results from different instruments under different experimental conditions are consistent: (1) All proton affinities obtained are in the range of 234-240 kcal/mol range. (2) $PA(\text{LeuEnk})$ is 1 kcal/mol higher than $PA(\text{MetEnk})$. (3) The effective temperatures obtained from the TQMS experimental data are in the range of 600-1200K. (4) The effective temperatures obtained from the Q-TOF experimental data are in the range of 200-300K.

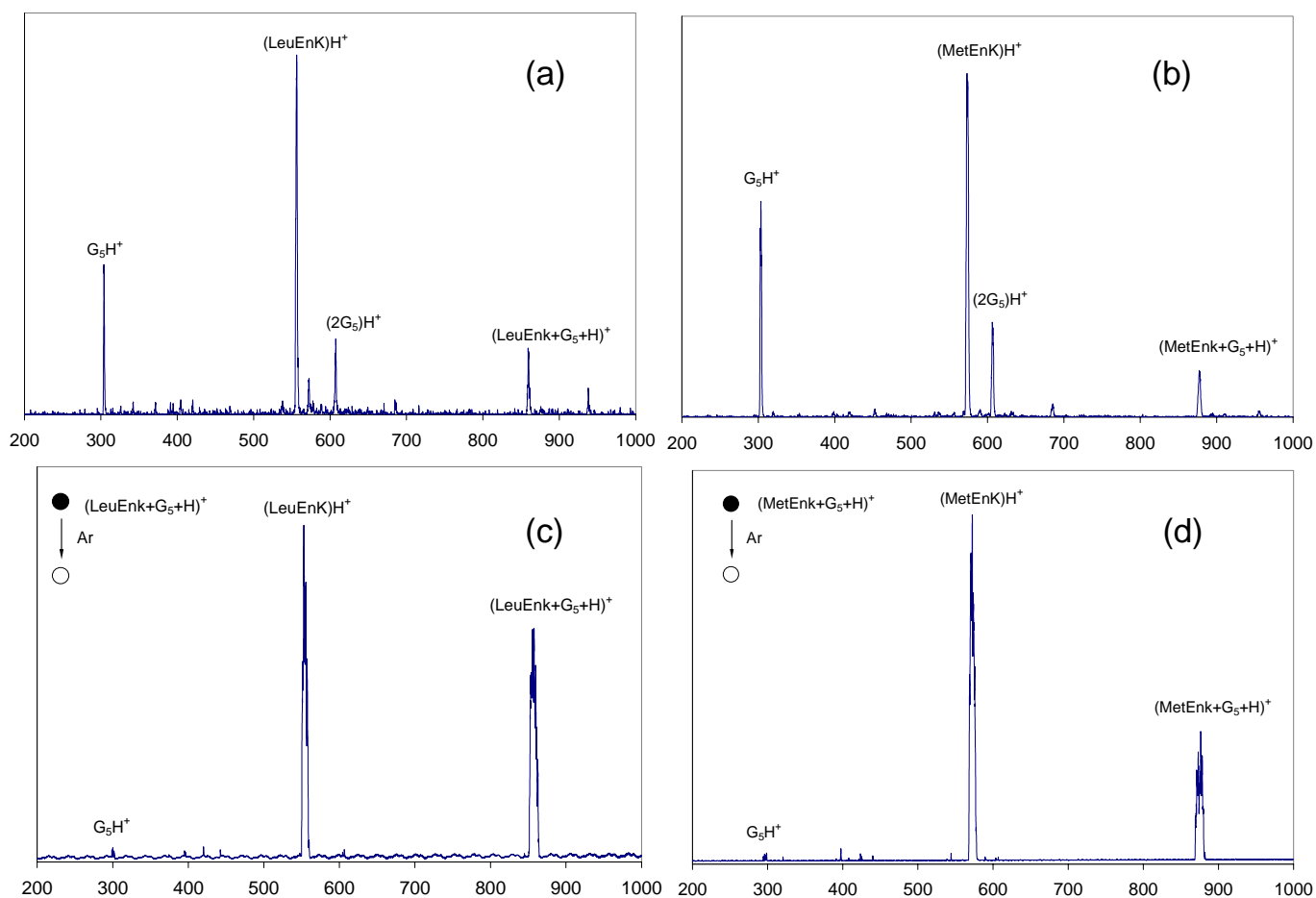


Figure 4.5. TQMS experiments of enkephalin proton affinity measurement versus pentaglycine: (a) Electrospray spectrum of a LeuEnk/pentaglycine mixture solution. (b) Electrospray spectrum of a MetEnk/pentaglycine mixture solution. (c) CID on the proton-bound heterodimer of LeuEnk and pentaglycine using Ar as collision gas. (d) CID on the proton-bound heterodimer of MetEnk and pentaglycine using Ar as collision gas.

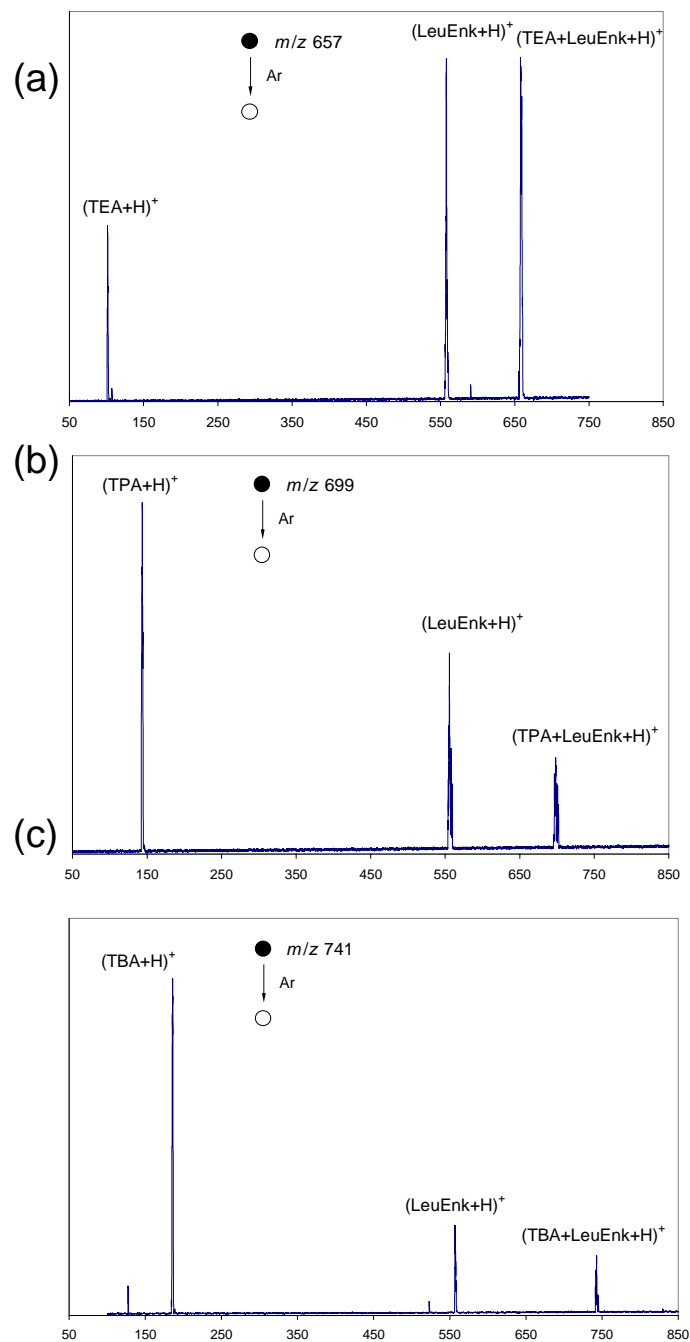


Figure 4.6. A set of representative CID product ion spectra: (a) CID on the proton-bound heterodimer of TEA and LeuEnk. Product ions observed are protonated LeuEnk and protonated TEA. (b) CID on the proton-bound heterodimer of TPA and LeuEnk. Product ions observed are protonated LeuEnk and protonated TPA. (c) CID on the proton-bound heterodimer of TBA and LeuEnk. Product ions observed are protonated LeuEnk and protonated TBA.

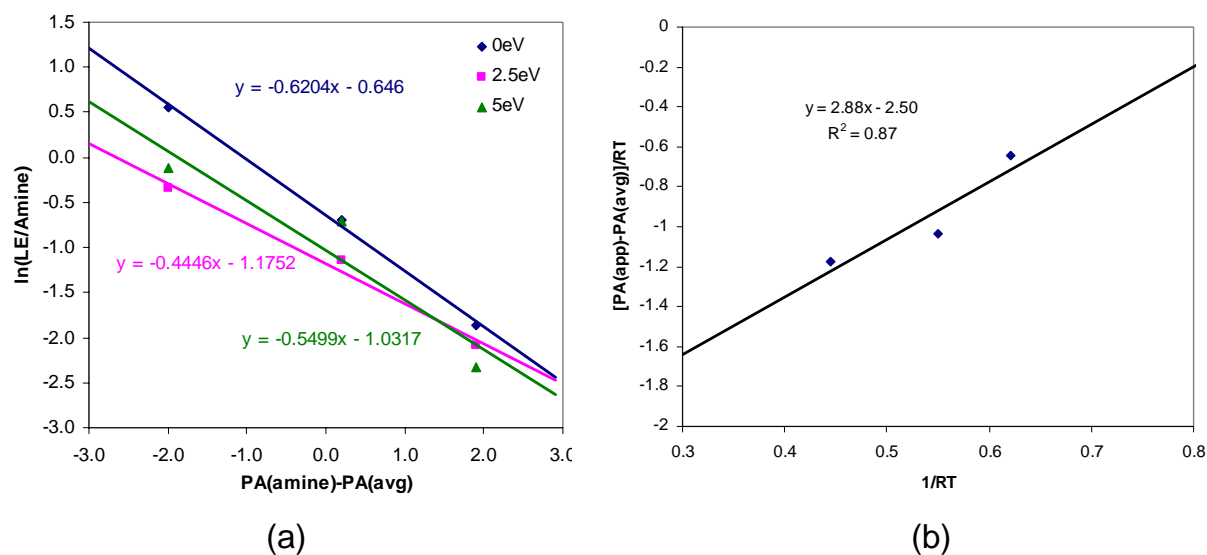


Figure 4.7. (a) The natural logarithm of the intensity ratio of protonated LeuEnk to protonated trialkylamine $\ln(\text{LeuEnk}/\text{Amine})$ as a function of $PA(\text{amine})-PA(\text{avg})$ obtained at various collision energies. (b) The plot of $[PA(\text{apparent})-PA(\text{avg})]/RT_{\text{eff}}$ versus $1/RT_{\text{eff}}$.

Table 4.1. Slopes and y-intercepts obtained from Figure 4.6(a). Effective temperatures are derived from the slopes ($-1/RT_{\text{eff}}$) and the apparent proton affinities are obtained from dividing y-intercepts by the corresponding slopes. Experiments are performed on the TQMS.

Collision energy (eV, Lab)	y-Intercept	Slope	$T_{\text{eff}} / \text{K}$	$GB^{\text{app}} \text{ kcal/mol}$
0	146.21	-0.6204	810	235.3
2.5	104.07	-0.4446	411	235.5
5.0	129.13	-0.5499	914	235.1

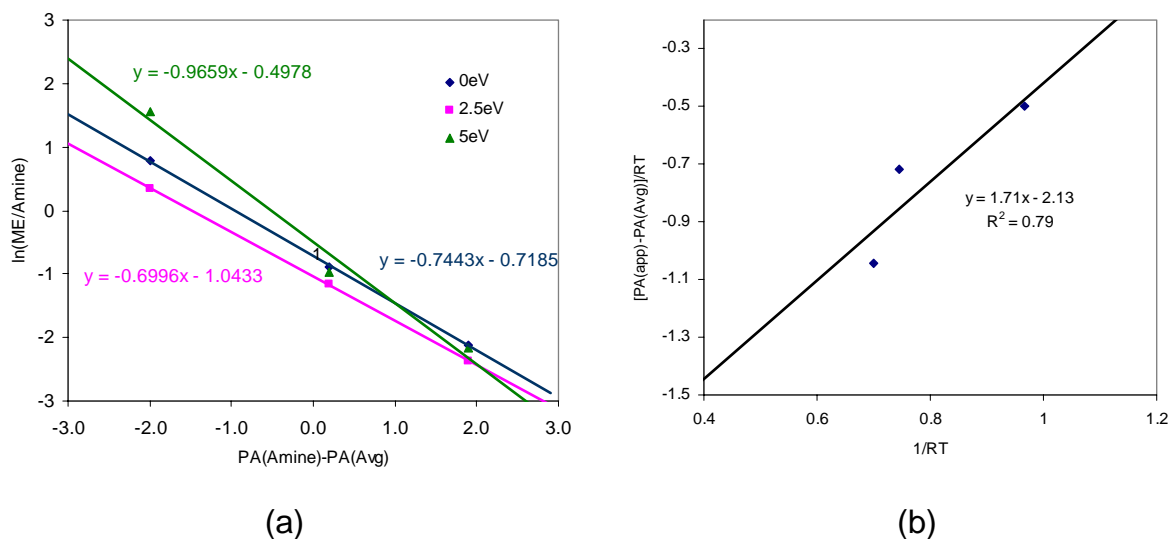


Figure 4.8. (a) The natural logarithm of the intensity ratio of protonated MetEnk to protonated trialkylamine $\ln(\text{MetEnk}/\text{Amine})$ as a function of $\text{PA}(\text{amine}) - \text{PA}(\text{avg})$ obtained at various collision energies. (b) The plot of $[\text{PA}(\text{apparent}) - \text{PA}(\text{avg})]/RT_{\text{eff}}$ versus $1/RT_{\text{eff}}$.

Table 4.2. Slopes and y-intercepts obtained from Figure 4.7(a). Effective temperatures are derived from the slopes ($-1/RT_{\text{eff}}$) and the apparent proton affinities are obtained from dividing y-intercepts by the corresponding slopes. Experiments are performed on the TQMS.

Collision energy (eV, Lab)	y-Intercept	Slope	$T_{\text{eff}} / \text{K}$	$\text{GB}^{\text{app}} \text{ kcal/mol}$
0	175.47	-0.7443	675	235.8
2.5	164.54	-0.6996	718	235.2
5.0	228.13	-0.9659	520	236.2

Table 4.3. Summary of the slopes and y-intercepts from the plots of $[PA(\text{app})-PA(\text{avg})]/RT_{\text{eff}}$ vs. $1/RT_{\text{eff}}$ derived from data obtained from TQMS experiments. The absolute proton affinity is the sum of the slope and $PA(\text{avg})$ which is 236.7 kcal/mol for these experiments. The $\Delta(\Delta S)$ is obtained from the product of molar gas constant R and the y-intercept.

Experiment		Slope	y-intercept	PA (kcal/mol)	$\Delta(\Delta S)$ (cal/mol K)
LeuEnk	#1	2.88	-2.50	239.6	-4.98
	#2	2.36	-2.28	239.1	-4.54
	#3	3.43	-2.72	240.1	-5.41
	Average			239.6	-4.98
MetEnk	#1	1.71	-2.13	238.4	-4.24
	#2	2.79	-2.88	239.5	-5.73
	#3	1.51	-1.95	238.2	-3.88
	Average			238.7	-4.62

Table 4.4. Summary of experimental determination of the proton affinity of LeuEnk and MetEnk using TEA, TPA and TBA as references obtained from TQMS and Q-TOF at different experimental conditions. Proton affinities shown are the average of replicate experiments, the number of which is shown in parentheses.

	PA (LeuEnk) kcal/mol	PA (MetEnk) kcal/mol
TQMS, Ar as collision gas	239.6 ± 3.0 (3)	238.7 ± 3.0 (3)
TQMS, He as collision gas	237.4 ± 3.0 (2)	235.5 ± 3.0 (2)
Q-TOF, Ar as collision gas	234.5 ± 3.0 (2)	233.7 ± 3.0 (2)

4.4. Discussion

4.4.1 The absolute proton affinity

The proton affinity for LeuEnk and MetEnk obtained from the TQMS experiments (average from experiments using Ar and He as collision gas) are 238.5 ± 5.0 kcal/mol and 237.1 ± 5.0 kcal/mol, which is about 4 kcal/mol above the corresponding results obtained from the Q-TOF experiments. In the triple-quadrupole experiments, the analyzer quadrupole (Q_3) is tuned until the peaks in the mass range examined possess equal resolutions as defined by the peak width in order to minimize any mass discrimination problem. However, a similar optimization will not overcome the known low m/z ion discrimination problem in an orthogonal injection time-of-flight mass spectrometer such as that used in this study [27]. Therefore, the values obtained from the Q-TOF instrument in the present study are considered only as qualitative and are used to consider the impact of instrumentation on the results.

The absolute proton affinity from LeuEnk and MetEnk from TQMS are indistinguishable. However, the LeuEnk and MetEnk relative proton affinity measurement unambiguously reveals that the proton affinity of LeuEnk is 0.1 kcal/mol smaller than the proton affinity of MetEnk. Combined these results, the absolute proton affinity of LeuEnk and MetEnk is reported to be 238.5 ± 5.0 kcal/mol 238.6 ± 5.0 kcal/mol, respectively, from the current study.

The proton affinity difference between LeuEnk and MetEnk is small (~ 1 kcal/mol) compared to proton affinity difference (~ 5 kcal/mol) between amino acid leucine (PA = 218.6 kcal/mol) and amino acid methionine (PA = 223.6 kcal/mol). The primary structures of LeuEnk (YGGFL) and MetEnk (YGGFM) are different by only the C-terminal residue. Examining the proton affinities of the amino acid residues [28] that consists of these two peptides, one see that methionine is the most basic residue in YGGFM. However, the experiment shows that this

proton affinity trend is not maintained by LeuEnk and MetEnk. It is not unreasonable to assume that the proton affinity of each pentapeptide is defined by the molecule as a whole, rather than by a simple perturbation induced by one amino acid change. Additional support for this idea can be obtained from gas-phase basicities or proton affinity measurements of other simple peptides. Carr and Cassdy [16] found that the gas-phase basicity of GGK is larger than GGH, in agreement with the relative proton affinity of K and H. But the location of the basic residue (histidine and lysine) affects the gas-phase basicities of the tripeptides, e.g., GB(GGH) = 229.4±3.0 kcal/mol, GB(GHG) = 226.2±3.0 kcal/mol, and GB(HGG) = 227.8±3.0 kcal/mol. These results suggest that the location histidine or lysine affects the conformation of the peptides examined and it is these conformations that determine the proton affinities of these peptides. Wu and Fenselau have shown that the proton affinity of polyglycine increases when the length of the polypeptide chain increases [14]. The proton affinity jumps about 8 kcal/mol from monoglycine to diglycine, and increases on average by about 4 kcal/mol per added residue from diglycine to pentaglycine and increases about 3 kcal/mol per added residue from pentaglycine to decaglycine. This trend of smaller increases in proton affinity per added residue, as the peptide's chain increase, also indirectly suggests that the conformation may play an important role in the determination of proton affinity of peptides. The similar proton affinity between LeuEnk and MetEnk obtained from the present study suggests that the gas-phase conformation of protonated LeuEnk and MetEnk are very similar.

4.4.2 Entropy consideration.

The entropy change $\Delta(\Delta S)$, derived from $R\ln(Q_1^*/Q_2^*)$, which is the y-intercept in $[PA(\text{apparent})-PA(\text{avg})]$ vs. $1/RT_{\text{eff}}$ plot, in the extended kinetic method measurement, is the

reaction entropy difference between two fragmentation channels leading to protonated LeuEnk or MetEnk or protonated TEA, TPA or TBA. The similar $\Delta(\Delta S)$ from LeuEnk and MetEnk in the Ar CID experiment in the triple experiments (Table 4.3) suggests that entropy difference of these two fragment are similar. One assumption that the extended kinetic method based is the constant entropy difference between the unknown molecule and references. The relative constant R^2 values (around 0.7-0.8) in such plots in the TQMS experiments suggest that the assumption is generally valid in the present study. However, using the $\Delta(\Delta S)$ to represent the entropy in the extended kinetic study has been under debate in the past few years [21, 29, 30]. The entropy effect in a system involving complicate molecules, such as peptides, can not be ignored. An approach combining computation and experiment to evaluate the entropy might be appropriate, which is, unfortunately, difficult.

4.4.3. Effective temperature.

The effective temperature in the kinetic method study is not a thermodynamic value due to the fact that the weakly bound complex ions decomposing in kinetic method study conditions do not possess a Maxwell-Boltzmann distribution [10, 31]. The effective temperature reflects the fraction of activated ions that happen to dissociate during the instrument time window. In another word, effective temperature can be considered as the overlap of the lifetime of an activated complex and the instrument time window. Variations of instrument operation conditions, including collision energy, collision target and collision gas density, will affect the effective temperature derived. In the present study, the effective temperature obtained from the triple-quadrupole experiment is in the range of 600-1000K; and from the Q-TOF experiment is 200-300K. Thus, an average value of 800K and 250 K are adopted for the triple-quadrupole and

Q-TOF respectively to estimate the relative proton affinity between LeuEnk and MetEnk. The effective temperature in a CID experiment reflects the amount of energy deposited to the complex ion, which depends on the mass of the collision target, number of collisions and details of collision dynamics [21]. So, it is not surprised that the effective temperature from two different instruments are dramatically different. In our triple quadrupole experiment, with a 20-cm-long octopole collision cell, the single collision limit is around 1×10^{-5} Torr for a complex ion involving a pentapeptide. Considering the fact that the actual pressure inside the relative isolate collision chamber (which is connected to Q_1 and Q_3 by two inter-lens) is much higher than the pressure read from the ion gauge near the inlet of the turbo pump, some complex ions in the triple-quadrupole CID experiment might undergo multiple collisions, which result in elevated effective temperature. The lower effective temperature obtained from the Q-TOF instrument using the same collision gas reflects the different collision dynamics originated from different instrument configurations. A more systematic and straightforward means to examine this complicated problem is to examine the collision induced dissociation under a strict single-collision condition as studied by Armentrout and co-workers [32, 33]. A common and simple practice of deriving thermochemical value of a class of structurally similar molecules via kinetic method is first to establish the ladder among these molecules using simple kinetic method. Then, the thermochemical value of a specific molecule is measured against several references via extended kinetic method; the effective temperature is derived and used to obtain the absolute thermochemical values of all the molecules in the ladder [18-20]. Because of the assumption that a common effective temperature among different complex is very unlikely to be valid, a larger error bar (as large as 50%) in the effective temperature is appropriated. However, such a large

uncertainty in effective temperature can only introduced a few kilo calories per mole uncertainty in proton affinity or other cation affinities.

4.5. Conclusion

The proton affinity of LeuEnk and MetEnk were measured against three trialkylamine using extended kinetic method to be 238.5 ± 5.0 kcal/mol and 237.1 ± 5.0 kcal/mol respectively. The entropy effect, probably originating from intramolecule hydrogen binding plays a role in determining the proton affinity peptide's proton affinity. The proton affinities obtained from the experiments performed on different instruments and at different operation conditions are consistent. The effective temperature, however, varies with the experimental conditions. Although the applying of the assumptions of kinetic method is difficult to validate on a system involving complex biological molecules, the extended kinetic method can provide a relative simple way to establish a narrow range of the thermochemical properties. Although kinetic is a sensitive method and can differentiate a small amount of difference in thermochemical properties, applying kinetic method to a system that entropy effect can not be ignored should be careful. Because that the kinetic method is not an intrinsically accurate or precise method of obtaining thermodynamic information [34], the thermochemical value derived from kinetic method should be cautiously presented and a large error is more appropriate.

4.6. References

- [1] D.T. Krieger, Science 222 (1983).
- [2] M.R. Emmett, P.E. Andren, and R.M. Caprioli, J. Neurosci. Methods 62 (1995) 141-147.
- [3] P.E. Andren and R.M. Caprioli, Brain Res. 845 (1999) 123-129.

- [4] W.E. Haskins, Z. Wang, C.J. Watson, R.R. Rostand, S.R. Witowski, D.H. Powell, and R.T. Kennedy, *Anal. Chem.* 73 (2001) 5005-5014.
- [5] M.H. Amad, N.B. Cech, G.S. Jackson, and C.G. Enke, *J. Mass Spectrom.* 35 (2000) 784-789.
- [6] R. Yamdagni and P. Kebarle, *J. Am. Chem. Soc.* 98 (1976) 1320-1324.
- [7] P. Kebarle, *Ann. Rev. Phys. Chem.* 28 (1977) 445-476.
- [8] J.L. Beauchamp, *Ann. Rev. Phys. Chem.* 22 (1971) 527-561.
- [9] R.G. Cooks, J.S. Patrick, T. Kotiaho, and S.A. McLuckey, *Mass. Spectrom. Rev.* 13 (1994) 287-339.
- [10] R.G. Cooks and P.S. Wong, *Acc. Chem. Res.* 31 (1998) 379-386.
- [11] P.J. Bobinson and K.A. Holbrook, *Unimolecular Reaction. 1972: Wiley.*
- [12] S.A. McLuckey and R.G. Cooks, *J. Am. Chem. Soc.* 103 (1981) 1313-1317.
- [13] X. Cheng, Z. Wu, and C. Fenselau, *J. Am. Chem. Soc.* 115 (1993) 4844-4848.
- [14] Z. Wu and C. Fenselau, *J. Am. Soc. Mass. Spectrom.* 3 (1992) 863-866.
- [15] Z. Wu and C. Fenselau, *Rapid. Commun. Mass Spectrom.* 8 (1994) 777-780.
- [16] S.R. Carr and C.J. Cassady, *J. Am. Soc. Mass. Spectrom.* 7 (1996) 1203-1210.
- [17] M.J. Nold, B.A. Cerda, and C. Wesdemitois, *J. Am. Soc. Mass. Spectrom.* 10 (1998) 1-8.
- [18] W.Y. Feng, S. Gronert, and C. Lebrilla, *J. Phys. Chem. A* 107 (2003) 405-410.
- [19] M.M. Kish, G. Ohanessian, and C. Wesdemitois, *Int. J. Mass Spectrom.* 227 (2003) 509-524.
- [20] W.Y. Feng, S. Gronert, and C. Lebrilla, *J. Am. Chem. Soc.* 121 (1999) 1365-1371.
- [21] P.B. Armentrout, *J. Am. Soc. Mass. Spectrom.* 11 (2000) 371-379.
- [22] R.R. Krug, w.G. Hunter, and R.A. Grieger, *J. Phys. Chem.* 80 (1976).
- [23] R.R. Krug, w.G. Hunter, and R.A. Grieger, *J. Phys. Chem.* 80 (1976) 2341-2351.
- [24] C. Ouvrard, M. Berthelot, T. Lamer, and O. Exner, *J. Chem. Inf. Comput. Sci.* 41 (2001) 1141-1144.
- [25] S.P. Mirza, S. Prabhakar, and M. Vairamani, *Rapid. Commun. Mass Spectrom.* 15 (2001) 957-962.
- [26] L.D. Donna, A. Napoli, G. Sindona, and C. Athanassopoulos, *J. Am. Soc. Mass. Spectrom.* 15 (2004) 1080-1086.

- [27] I.V. Chernushevich, A.V. Loboda, and B.A. Thomson, *J. Mass Spectrom.* 36 (2001) 849-865.
- [28] NIST Standard Reference Database Number 69 - March 2003 Release.
- [29] X. Zheng and R.G. Cooks, *J. Phys. Chem. A* 106 (2002) 9939-9946.
- [30] K.M. Ervin, *J. Am. Soc. Mass. Spectrom.* 13 (2002) 435-452.
- [31] L. Drahos and K. Vekey, *J. Mass Spectrom.* 34 (1999).
- [32] M.T. Rodgers, K.M. Ervin, and P.B. Armentrout, *J. Chem. Phys.* 106 (1997) 4499-4506.
- [33] M.T. Rodgers and P.B. Armentrout, *J. Chem. Phys.* 109 (1998) 1787-1800.
- [34] P.B. Armentrout, *J. Mass Spectrom.* 34 (1999) 74-78.

Appendix A Gas-Phase Thermochemical Properties

The proton affinity (PA) of a molecule is defined as the negative of the enthalpy change of the hypothetical protonation reaction (eq. A.1) at 298 K:



$$PA = -\Delta H_{\text{rxn}}$$

The Gibbs free energy change associated with this protonation reaction (eq.A.1) is called the gas-phase basicity (GB) of molecule M.

$$GB(M) = -\Delta G_{\text{rxn}}(\text{eq. A.1})$$

The gas-phase acidity of a hydrogen containing molecule AH is the enthalpy change of the deprotonation reaction (eq. A.2) at 298 K.



$$\Delta H^{\circ}_{\text{acid}}(AH) = -\Delta H_{\text{rxn}}(\text{eq. A.2})$$

The electron affinity (EA) of a molecule or atom is defined as the negative of the enthalpy change for the electron attachment reaction (eq.A.3) at 0 K.



$$EA = \Delta H_{\text{rxn}}(\text{eq. A.3})$$